

# Terahertz detectors and focal plane arrays

A. ROGALSKI<sup>1</sup> and F. SIZOV<sup>2</sup>

<sup>1</sup>Institute of Applied Physics, Military University of Technology, 2 Kaliskiego Str., 00-908 Warsaw, Poland

<sup>2</sup>Institute of Semiconductor Physics of the Ukrainian National Academy of Sciences,  
Kiev-03028, 41 Nauki Ave, Ukraine

*Terahertz (THz) technology is one of emerging technologies that will change our life. A lot of attractive applications in security, medicine, biology, astronomy, and non-destructive materials testing have been demonstrated already. However, the realization of THz emitters and receivers is a challenge because the frequencies are too high for conventional electronics and the photon energies are too small for classical optics. As a result, THz radiation is resistant to the techniques commonly employed in these well established neighbouring bands.*

*In the paper, issues associated with the development and exploitation of THz radiation detectors and focal plane arrays are discussed. Historical impressive progress in THz detector sensitivity in a period of more than half century is analyzed. More attention is put on the basic physical phenomena and the recent progress in both direct and heterodyne detectors. After short description of general classification of THz detectors, more details concern Schottky barrier diodes, pair braking detectors, hot electron mixers and field-effect transistor detectors, where links between THz devices and modern technologies such as micromachining are underlined. Also, the operational conditions of THz detectors and their upper performance limits are reviewed. Finally, recent advances in novel nanoelectronic materials and technologies are described. It is expected that applications of nanoscale materials and devices will open the door for further performance improvement in THz detectors.*

**Keywords:** direct and heterodyne THz detectors, focal plane arrays, Schottky barrier diodes, SIS detectors, SIN detectors, hot electron bolometers, transition edge sensors, field-effect transistor detectors, extrinsic photodetectors, performance limits, novel THz detectors.

1. Introduction
2. Outlook on THz radiation specificity
3. Trends in developments of THz detectors
4. Direct and heterodyne THz detection
  - 4.1. Direct detection
  - 4.2. Heterodyne detection
  - 4.3. Heterodyne vs. direct detection
5. Photoconductive THz generation and detection
6. General classification of THz detectors
  - 6.1. Photon detectors
  - 6.2. Thermal detectors
7. Schottky barrier diodes
8. Extrinsic detectors
  - 8.1. Extrinsic germanium detectors
  - 8.2. Another extrinsic detectors
9. Pair braking photon detectors
10. Pyroelectric detectors
11. Semiconductor bolometers
12. Semiconductor hot electron bolometers
13. Superconducting hot-electron bolometers
14. Transition edge sensor bolometers

15. Field effect transistor detectors
16. Novel THz detectors
17. Conclusions

## 1. Introduction

The terahertz (THz) region of electromagnetic spectrum is often described as the final unexplored area of spectrum. First humans relied on the radiation from the Sun. Cave men used torches (approximately 500,000 years ago). Candles appeared around 1000 BC, followed by gas lighting (1772), and incandescent bulbs (Edison, 1897). Radio (1886–1895), X-rays (1895), UV radiation (1901), and radar (1936) were invented in the end of the 19-th and the beginning of the 20-th centuries. However, terahertz range of electromagnetic spectrum still presents a challenge for both electronic and photonic technologies.

THz radiation (see Fig. 1) is frequently treated as the spectral region within frequency range  $\nu \approx 1\text{--}10$  THz ( $\lambda \approx 300\text{--}30$   $\mu\text{m}$ ) [1–3] and it is partly overlapping with loosely treated submillimeter (sub-mm) wavelength band  $\nu \approx 0.1\text{--}3$  THz ( $\lambda \approx 3$  mm – 100  $\mu\text{m}$ ) [4]. Even wider region  $\nu \approx 0.1\text{--}10$  THz [5,6] is treated as THz band overlapping thus with

\* e-mail: rogan@wat.edu.pl

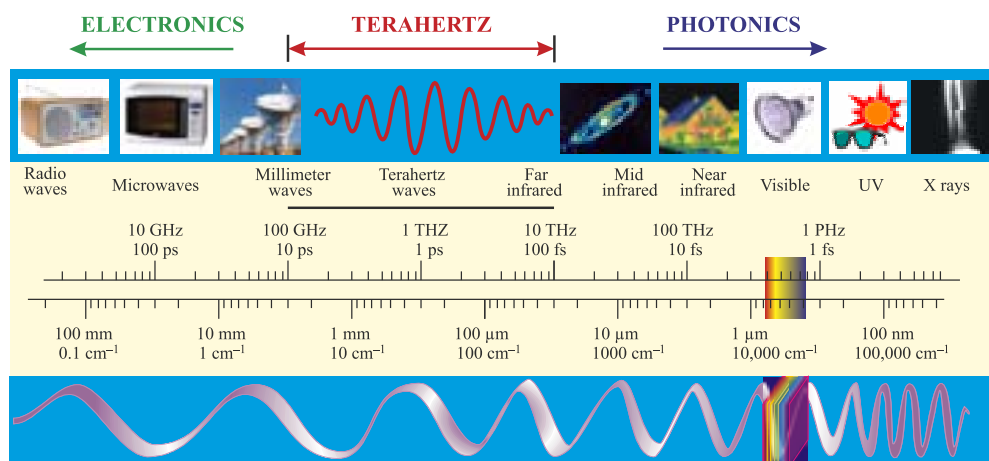


Fig. 1. The electromagnetic spectrum.

sub-mm wavelength band. As a result, frequently both these notions are used as equal ones (see, e.g. Ref. 7). Here, THz range is accepted as the range within  $\nu \approx 0.1\text{--}10$  THz. THz electronics spans the transition range from radio-electronics to photonics.

The THz region of the electromagnetic spectrum has proven to be one of the most elusive. Being situated between infrared light and microwave radiation, THz radiation is resistant to the techniques commonly employed in these well established neighbouring bands. Historically, the major use of THz spectroscopy has been by chemists and astronomers in the spectral characterization of the rotational and vibrational resonances and thermal-emission lines of simple molecules. Terahertz receivers are also used to study the trace gases in the upper atmosphere, such as ozone and many gases involved in ozone depletion cycles, such as chloride monoxide. Air efficiently absorbs in wide spectral THz region (except for narrow windows around  $\nu \approx 35$  GHz, 96 GHz, 140 GHz, and 220 GHz, and others, see Fig. 2 [8]). THz and millimeter waves are efficient at detecting the presence of water and thus, are efficient to discriminate different objects on human bodies (water content of human body is about 60%) as the clothes are transparent. In the longer

wavelength region (cm wavelength region) even persons hiding behind a wall (not very thick) can be visualized. It should be mentioned that about half of the luminosity of the Universe and 98% of all the photons emitted since the Big Bang belong to THz radiation [9]. This relict radiation carries information about the cosmic space, galaxies, stars and planets formation [10].

The past 20 years have seen a revolution in THz systems, as advanced materials research provided new and higher-power sources, and the potential of THz for advanced physics research and commercial applications was demonstrated. Numerous recent breakthroughs in the field have pushed THz research into the centre stage. As examples of milestone achievements we can mention the development of THz time-domain spectroscopy (TDS), THz imaging, and high-power THz generation by means of nonlinear effects [1–3]. Researches evolved with THz technologies are now received increasing attention, and devices exploiting this wavelength band are set to become increasingly important in diverse range of human activity applications (e.g., security, biological, drugs and explosion detection, gases fingerprints, imaging, etc.). The interest in the THz range is attracted by the fact that this range is the place where different physical phenomena are revealed which frequently calls for multidisciplinary special knowledge in this research area. Nowadays, the THz technology is also of much use in fundamentals science, such as nanomaterials science and biochemistry. This is based on the fact that THz frequencies correspond to single and collective excitations in nanoelectronic devices and collective dynamics in biomolecules. In 2004, *Technology Review*'s editors selected THz technology as one of “10 emerging technologies that will change your world” [11]. Overviews on various applications of THz technologies can be found, e.g., in Refs. 1–3, 6, 12–20.

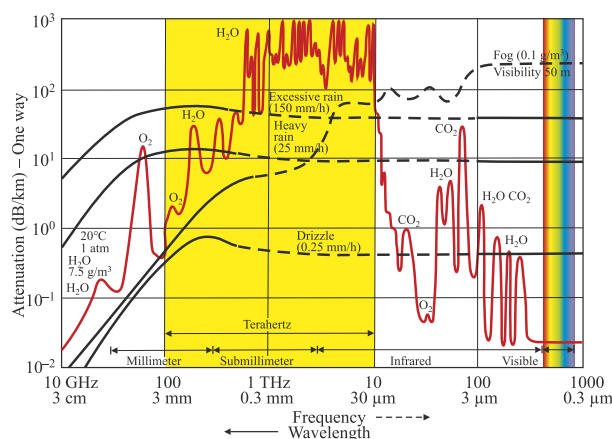


Fig. 2. Attenuation of the Earth atmosphere from visible to radiofrequency band region (after Ref. 8).

## 2. Outlook on THz radiation specificity

THz radiation due to its unique properties provides a variety of applications and opportunities in different field. Historically, astronomers were first which focused on THz detec-

tion technology since interstellar dust covers spectrum that ranges from 1 mm to 100  $\mu\text{m}$  (14–140 K below the ambient background on the Earth). Figure 3 shows the radiation spectrum of interstellar (dust, light and heavy molecules), a 30-K blackbody, and the 2.7-K cosmic background [21]. THz spectroscopy allows us true probe into the early universe, star forming regions, and many other abundant molecules.

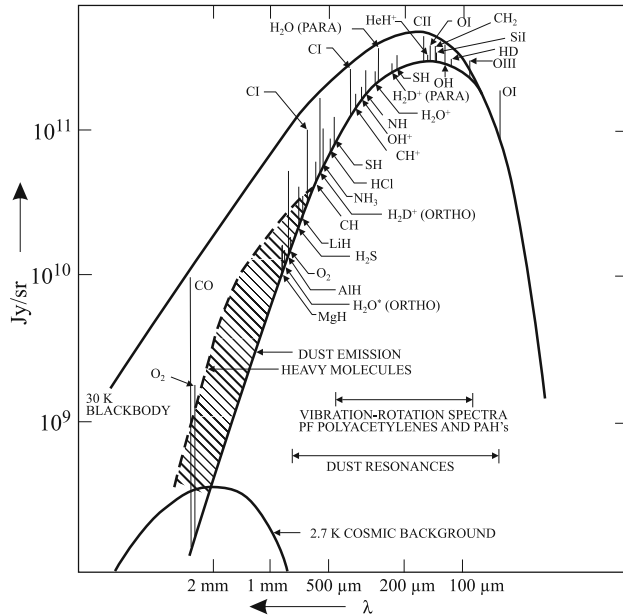


Fig. 3. Radiation spectrum of 30-K blackbody, typical interstellar dust and key molecular line emissions in the submillimeter (after Ref. 21).

THz remote sensing in the Earth's atmosphere has been a big challenge because of strong, ambient moisture absorption in the THz frequency range (see Fig. 4). Conventional THz generation and detection techniques cannot be applied to remote THz spectroscopy without suffering substantial attenuation during the THz wave propagation in the air. With currently available and practical THz detectors and sources, the measurements over distances larger than 20 m are very difficult. Because of considerable attenuation, THz waves are not very useful for long-range communications [22]. However, due to strong absorption, the transmission spectra of

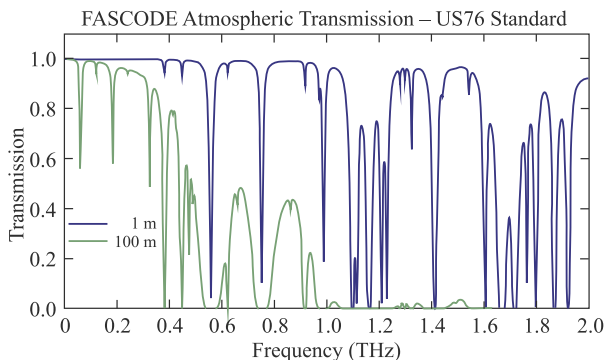


Fig. 4. Transmission of THz radiation in air.

a lot of materials can provide information about the physical properties of the materials investigated. In addition, an important feature of THz radiation is the ability to penetrate into and distinguish between non-metallic materials.

Unlike visible and IR detectors, the far IR and sub-mm wavelength detectors have not reached fundamental quantum limit characteristics yet. They are not limited by photon flux fluctuations (photon noise), except operation at some selected frequencies and sub-Kelvin temperature operation [23,24]. The registration of single THz photons was demonstrated using quantum dot devices [25,26].

The noise equivalent power ( $NEP$ ) is one of the figures of merit for detectors and characterizes their sensitivity. It is defined as the value of rms incident power on the detector generating a signal output equal to the rms noise output (signal-to-noise ratio;  $SNR = 1$ ). Intrinsic temperature fluctuation noise of thermal detector defines its upper  $NEP$  limit as

$$NEP = (4k_B T^2 G_{th})^{1/2}, \quad (1)$$

where  $k_B$  is the Boltzmann's constant,  $T$  is the temperature of the thermistor, and  $G_{th}$  is the thermal conductance between the detector and the heat sink. For the lower  $G_{th}$ , the lower values of  $NEP$  can be achieved. For  $T \approx 50$  mK and low phonon conductance  $G_{th} \approx 10$  fW/K, the values of electrical  $NEP \approx 4 \times 10^{-20}$  W/Hz $^{1/2}$  can be achieved at low background fluctuations conditions. Figure 5 presents the data of the background-limited detector sensitivity for THz spec-

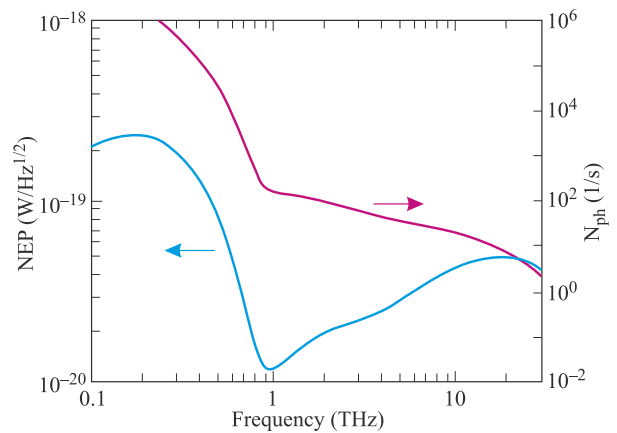


Fig. 5. Background-limited detector sensitivity for THz spectroscopy in space. The flux of photons  $N_{ph}(\nu)$  due to the background radiation from the Universe was calculated from the experimental luminosity of continuum radiation within a diffraction-limited beam. This estimate assumes that the detector is sensitive to a single-photon polarization, its optical coupling efficiency is 25%, and its spectral resolution  $\nu/d\nu \approx 1000$  corresponds to the width of a typical extragalactic emission line ( $\nu = 2\nu/c$  results from Doppler line broadening in distant galaxies with rotational velocities  $u \approx 10^2$  km/s). The background photon flux is very weak:  $N_{ph} < 100$  photons/s at  $\nu > 1$  THz. Fluctuations of this flux (the photon shot noise) determine the background-limited detector sensitivity  $NEP_{ph}(\nu)$ . At  $\nu < 1$  THz, the detector performance is limited by the cosmic microwave background; at higher frequencies it is limited by the radiation from the galactic core and dust clouds (after Ref. 7).

troscopy in space and also the photons flux at cosmic background shot noise conditions. The presented dependences are valid both for direct detection and heterodyne detector systems, and also for coherent (mixer) focal plane arrays, which at present are realized only in single pixel or small number detector arrays [27].

Realization of appropriate low values of  $NEP \sim 4 \times 10^{-20}$  W/Hz<sup>1/2</sup> considerably depends on background temperature, spectral band, and resolution needed. The calculated  $NEP$  values for  $\Delta\lambda/\lambda = 10^{-3}$  and for diffraction limited beams taking into account only the fluctuations of power from the background radiation are shown in Fig. 6. Calculations were done for Poisson statistics (solid curves) that dominates in IR systems and with account of the Gaussian statistics (dashed curves), which is important for THz/sub-THz region. It is seen that the possible upper limit of  $NEP \sim 10^{-20}$  W/Hz<sup>1/2</sup> for low background conditions ( $T = 3$  K) is possible only in the spectral range  $\nu > 1.2$  THz ( $\lambda < 250$   $\mu$ m), the wavelengths region where the Cryogenic Aperture Large Infrared Space Telescope Observatory (CALISTO) will be operated (spectral range from 30  $\mu$ m to 300  $\mu$ m). It is predicted that the technology for CALISTO will be developed during the next decade [28].

The critical differences between detection at sub-mm wavelengths and IR detection lie in small photon energies (at  $\lambda \approx 300$   $\mu$ m,  $h\nu \approx 4$  meV, compared to the thermal energy of 26 meV at room temperature). Also the Airy disk diameter (diffraction limit) defined by

$$A_{dif} \approx 2.44 \frac{\lambda f}{D} = 2.44 \lambda (f/\#), \quad (2)$$

is large, what determines low spatial resolution of THz systems. Here  $f$  is the focus length of optical system,  $D$  is its input diameter, and  $f/\#$  is the  $f$ -number of the optical system.

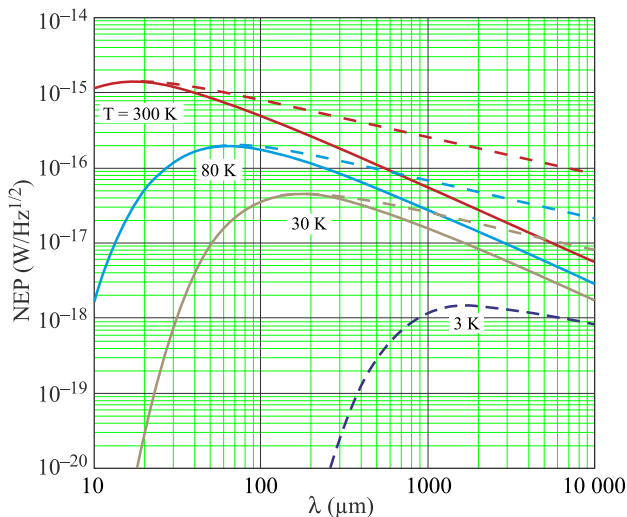


Fig. 6. Photon noise limited  $NEP$  calculated only for Poisson statistics (solid curves) that dominates in IR systems and with account of the Gaussian statistics (dashed curves), which is important for THz/sub-THz region.  $\Delta\lambda/\lambda = 0.001$ . Calculations are done for emissivity, transmittivity, and coupling efficiency equal to 1 ( $\varepsilon, \tau, \eta = 1$ ).

To achieve higher spatial imaging resolution, two approaches could be applied: solid immersion lenses (usually Si lenses) or near-field imaging. Compared to the visible region, the near-field imaging in the THz region has not yet been well established, because, e.g., of the lack of THz fibres or other bulk media transparent in THz region to generate near-field waves.

One of the problem, which limits an advent of heterodyne arrays in THz spectral region needed for high-resolution spectroscopy applications ( $\nu/\Delta\nu \approx 10^6$ ), photometry ( $\nu/\Delta\nu \approx 3-10$ ) and imaging, lies in technology limitations of solid-state local oscillator (LO) power (see Fig. 7). Around  $\nu \approx 1$  THz one can see that there exist the so cold “THz gap”.

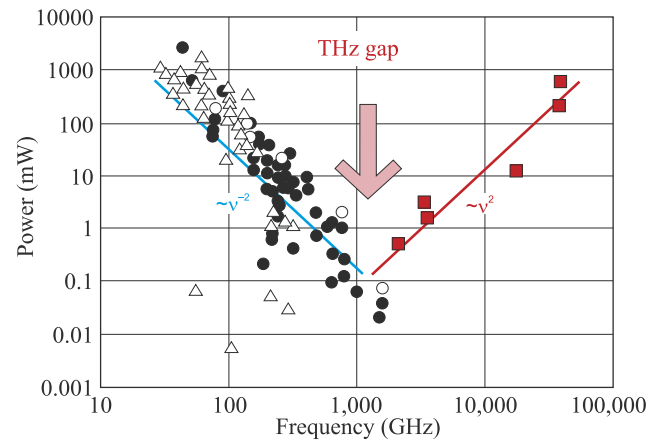


Fig. 7. THz gap with respect to source technology: (■) quantum cascade lasers (QCL) are progressing downward from high frequencies, the lowest  $\nu = 1.2$  THz,  $T = 110$  K – CW,  $T = 163$  K – pulsed; (●) frequency multipliers dominate other electronic devices ( $\Delta$ ) above about 150 GHz; cryogenic sources are shown as hollow symbols ( $\circ$ ) (after Ref. 5).

### 3. Trends in developments of THz detectors

The detection of THz radiation is resistant to the commonly employed techniques in the neighbouring microwave and infrared (IR) frequency bands. In THz detection, the use of solid state detectors has been hampered for the reasons of transit time of charge carriers being larger than the time of one oscillation period of THz radiation. Also the energy of radiation quanta is substantially smaller than the thermal energy at room temperature and even liquid nitrogen temperature.

Detector development is at the heart of all current plants. There exists a large variety of traditional deeply cooled mm and sub-mm wavelength detectors (mainly bolometers) as well as new propositions based on optoelectronic quantum devices [20], carbon nanotube bolometers, plasma wave detection by field effect transistors, and hot electron room temperature bipolar semiconductor bolometers [23,24].

Progress in THz detector sensitivity has been impressive in a period of more than half century what is shown in Fig. 8(a) in the case of bolometers used in far-IR and sub-mm-wave astrophysics [29]. The  $NEP$  value has decreased by



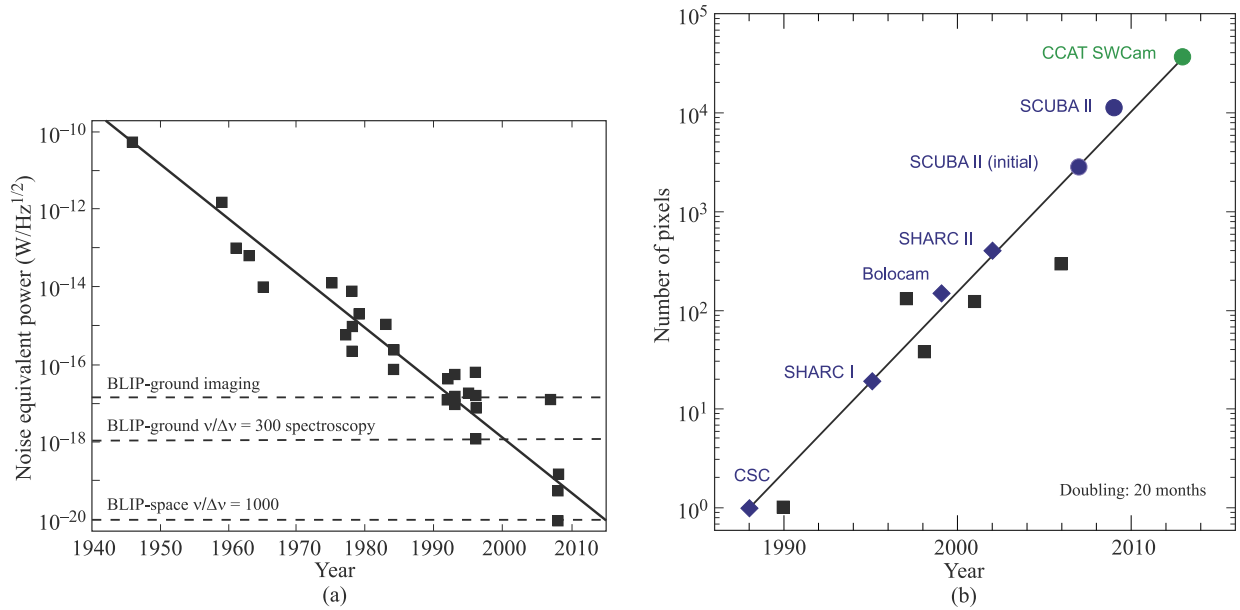


Fig. 8. Trends in development of THz detectors: (a) improvement in the bolometer NEP-value for more than half a century (sensitivity doubled every 2 years over the past 70 years) and (b) detector arrays have doubled in format every 20 months over the past 10 years; green symbol indicates current expectation (adapted after Ref. 29).

a factor of  $10^{11}$  in 70 years, corresponding improvements by a factor of two every two years. Individual detectors achieved photon noise limited performance for ground-based imaging in the 1990s. The photon noise from astrophysical sources, achievable in space with a cold telescope,  $\sim 10^{-18} \text{ W/Hz}$ , is now within demonstrated sensitivities. In present decade, the studies of inflation via cosmic microwave background (CMB) polarization will be driven not by detector sensitivity but by array formats. Far-infrared spectroscopy from a cold telescope, however, requires sensitivity  $\sim 10^{-20} \text{ W/Hz}$  to reach the astrophysical photon noise limit. Achieving this sensitivity in working detector arrays remains a challenge for the coming decade, as the number of the detectors in the array is a key parameter that determines the information capabilities of the system [24] and the speed improvement in obtaining a complete imaging or spectrum when observing galactic objects, as the accumulation time  $\tau_{acc}$  at each sensitive element is proportional to the number  $M_e$  of sensitive elements in the array and inversely proportional to the frame rate  $f_r$ , and the number of picture dots  $M$ ,  $\tau_{acc} = 1/f_r(M_e/M)$ .

The development of pixel arrays has been comparably revolutionary [29]. Figure 8(b) shows increase in a number of pixels in the period over last two decades. Detector arrays have doubled in format every 20 months over the past 10 years producing arrays with pixels now numbering in the thousands. Steady increase in overall observing efficiency is expected in near future, which by now has reached factors in the range of  $10^{12}$  in comparison to capabilities in the early 1960s.

For space-board systems, the system NEP should not be limited by the thermal emission from the telescope optics or the detector noise itself. Assuming that the telescope is

cooled to  $\sim 4 \text{ K}$ , its emission should be negligible throughout the sub-mm/FIR range, and the requirement on detector performance (and ultimate system sensitivity) is set by the astronomical background and spectral resolution needed (see, e.g. Fig. 6). At longer wavelengths, this is dominated by dust emission from the Milky Way, together with the cosmic microwave background. At shorter wavelengths ( $\lambda <$

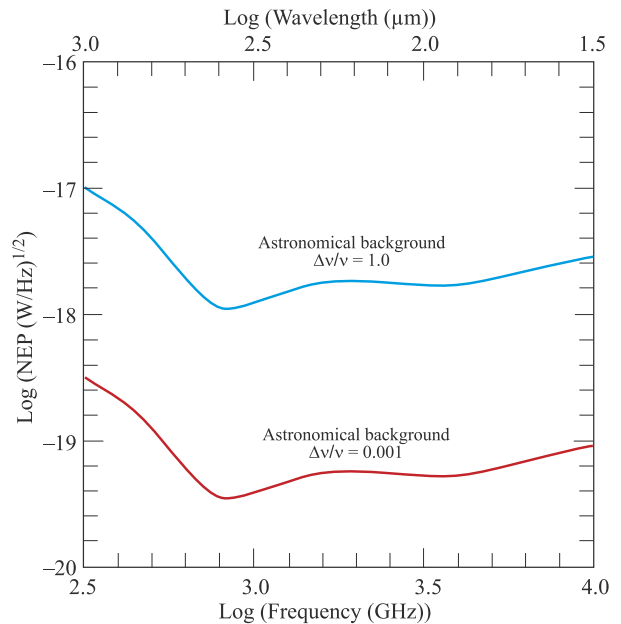


Fig. 9. Dark sky astronomical background as a function of wavelength for two different fractional resolutions,  $v/\Delta v = 1$  for photometry and,  $v/\Delta v = 1000$  for moderate resolution extragalactic spectroscopy. The detector NEP should be well below these values in order that the overall noise be dominated by the astronomical background (after Ref. 28).

100  $\mu\text{m}$ ), the zodiacal emission becomes significant. These two contributions have different angular distributions, but if one considers only the “darkest sky”, the resulting detector *NEP* requirements should be below  $3 \times 10^{-18} \text{ W/Hz}^{1/2}$  ( $\nu/\Delta\nu = 1$ , photometry requirements), and for  $\nu/\Delta\nu = 1000$  spectroscopy below  $8 \times 10^{-20} \text{ W/Hz}^{1/2}$  ( $\lambda \sim 30\text{--}1000 \mu\text{m}$ , Fig. 9).

NASA has historically been the leading US agency for promoting the development of long wavelength detector technologies. Figure 10 shows the sensitivities of currently-planned or active far-IR/sub-mm spectroscopic facilities in near future, instead Table 1 describes shortly several airborne and space-borne platform missions.

Table 1. Far-IR spectroscopy platforms.

|  |   |   |
|--|---|---|
| Spitzer<br>Space<br>Telescope<br><br>2003    |    | The <b>Spitzer Space Telescope</b> was launched in August 2003. It is the last of NASA's “great observatories” in space. Spitzer is much more sensitive than prior infrared missions and studies the universe at a wide range of infrared wavelengths. Spitzer concentrates on the study of brown dwarfs, super planets, protoplanetary and planetary debris disks, ultraluminous galaxies, active galaxies, and deep surveys of the early universe.  |
| SOFIA<br><br>2005                            |    | SOFIA ( <b>Stratospheric Observatory for Infrared Astronomy</b> ) was finally completed in 2005. SOFIA, a joint project between NASA and the German Space Agency, incorporates a 2.5 meter optical/infrared/sub-millimeter telescope mounted in a Boeing 747. Designed as a replacement for the successful Kuiper Airborne Observatory, SOFIA is the largest airborne telescope in the world.   |
| Herschel<br>Space<br>Observatory<br><br>2009 |   | The <b>Herschel Space Observatory</b> carried into orbit in May 2009 is a European Space Agency infrared-submillimeter mission. Herschel is built to perform spectroscopy and photometry over a wide range of infrared wavelengths and it is used to study galaxy formation, interstellar matter, star formation, and the atmospheres of comets and planets. The Herschel Observatory is capable of seeing the coldest and dustiest objects in space. It is the largest space telescope ever launched carrying a single mirror of 3.5 meter in diameter.  |
| ALMA<br><br>2011                             |  | The <b>Atacama Large Millimeter/submillimeter Array (ALMA)</b> is an international partnership between Europe, North America, East Asia and the Republic of Chile to build the largest astronomical project in existence. It is an astronomical interferometer, comprising an array of 66 12-meter and 7-meter diameter radiotelescopes observing at millimeter and submillimeter wavelengths. It is being built on the Chajnantor plateau at 5000 meters altitude in the Atacama desert of northern Chile. ALMA is expected to provide insight on star birth during the early universe and detailed imaging of local star and planet formation. Costing more than a billion dollars, it is the most ambitious ground-based telescope currently under construction. ALMA will begin scientific observations in the second half of 2011 and is scheduled to be fully operational by the end of 2012. |
| James Webb<br>Space<br>Telescope<br><br>2014 |  | The <b>James Webb Space Telescope (JWST)</b> is a large, infrared-optimized space telescope, scheduled for launch in 2014. It is a visible/infrared space mission which will have extremely good sensitivity and resolution, giving us the best views yet of the sky in the near-mid infrared. JWST will be used to study the early universe and the formation of galaxies, stars and planets. Webb will have a large mirror, 6.5 meters in diameter and a sunshade the size of a tennis court. Both the mirror and sunshade will not fit onto the rocket fully open, so both will fold up and open once Webb is in outer space. Webb will reside in an orbit about 1.5 million km from the Earth.  |
| SPICA/BLISS<br><br>2017                      |  | The <b>Background Limited Infrared Submillimeter Spectrograph (BLISS)</b> is a far-IR spectrograph concept for the <b>Space Infrared Telescope for Cosmology and Astrophysics (SPICA)</b> . The SPICA mission is a future Japanese infrared astronomical satellite, with launch envisioned in 2017, to explore the universe with a cooled, large telescope. The philosophy of BLISS is to provide a rapid survey spectroscopy capability over the full far-IR range. The baseline approach is a suite of broadband grating spectrometer modules with transition-edge superconducting (TES) bolometers. SPICA will use a cooled telescope (3.5 m diameter primary, $\sim 5 \text{ K}$ ) to achieve sensitivities currently inaccessible to existing facilities operating over this wavelength range (SOFIA, Herschel).   |

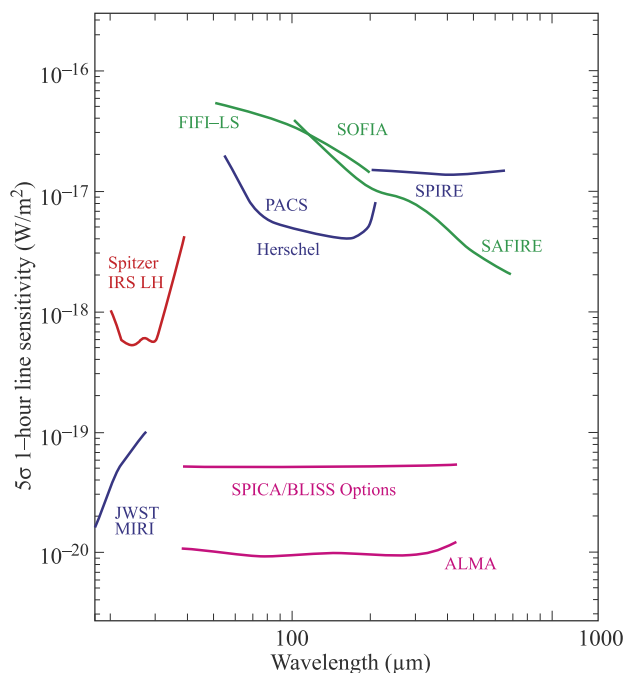


Fig. 10. Sensitivity of far-IR spectroscopy platforms (after Ref. 29).

As last figure shows, the James Webb space telescope (JWST) operates at wavelengths below about 27  $\mu\text{m}$ . The Atacama Large Millimeter/submillimeter Array (ALMA) operating through a number of submillimeter atmospheric windows as well as  $\sim 650 \mu\text{m}$ , will have sensitivities at least 100 times higher than Herschel spanning the intervening 60–650  $\mu\text{m}$  wavelength range. ALMA and JWST are currently scheduled to start operations within the next few years. The Space Infrared Telescope for Cosmology and astrophysics (SPICA), with launch envisioned in 2017, will provide two-to-three orders of magnitude increase in sensitivity in comparison with Herschel that will bring far-IR/sub-mm sensitivity into line with those of JWST and ALMA. The ambitious requirements of future space missions are summarized in Table 2.

#### 4. Direct and heterodyne THz detection

All radiation detection systems in THz spectral ranges can be divided into two groups:

- incoherent detection systems (with direct detection sensors), which allow only signal amplitude detection and which, as a rule, are broadband detection systems, and

- coherent detection systems, which allow detecting not only the amplitude of the signal, but also its phase.

Coherent signal detection systems use heterodyne circuit design, since so far, for high radiation frequency range, proper amplifiers do not exist. The detected signals are transferred to much lower frequencies ( $f \approx 1\text{--}30 \text{ GHz}$ ) where they are amplified by low-noise amplifiers. Basically, these systems are selective (narrow-band) detection systems.

##### 4.1. Direct detection

Detectors with direct signal detection basically are used in spectroscopic and technical vision systems of ultraviolet, visible, IR, sub-mm, and mm regions. In sub-mm and mm wavelength bands they are suitable for applications that do not require ultrahigh spectral resolution ( $\nu/\Delta\nu \approx 10^6$ ) that is provided by heterodyne detector spectroscopic systems. But unlike heterodyne detection systems, there do not exist the problem of multielement arrays formation conditioned by LO power and fast detector response ( $\tau \approx 10^{-10}\text{--}10^{-11} \text{ s}$ ).

In direct THz detection systems, even room temperature detectors can be used with relatively long response time ( $\tau \approx 10^{-2}\text{--}10^{-3} \text{ s}$ ) and modest sensitivity. Among them there are Golay cells [31,32], pyroelectric detectors [33], different kind of thermal direct detection detectors (bolometers and microbolometers) [34,35], which use antennas to couple power to a small thermally absorbing regions. The NEP value for uncooled detectors typically is from  $10^{-10}$  to  $10^{-9} \text{ W/Hz}^{1/2}$  (see Table 3, Ref. 36).

Different kind of cooled semiconductor detectors (hot electron InSb, Si, Ge bolometers, extrinsic Si and Ge) [1,24, 37–43] with the response time of  $\tau \approx 10^{-6}\text{--}10^{-8} \text{ s}$  and  $NEP \approx 10^{-13}\text{--}5 \times 10^{-17} \text{ W/Hz}^{1/2}$  and operated at  $T \approx 4 \text{ K}$  are also used. Direct extrinsic photoconductors (stressed Ge:Ga) can be sensitive up to the wavelength  $\lambda \approx 400 \mu\text{m}$  [41] and can be assembled into arrays [44]. However, the most sensitive direct detectors in sub-mm and mm wavebands are different bolometer designs cooled to  $T \approx 100\text{--}300 \text{ mK}$  reaching NEP limited by cosmic background radiation fluctuations [7, 45–48]. Intrinsic and extrinsic photon detectors, based on interband, intersubband or impurity optical transitions, are used only in the short range of sub-mm spectral band. The reason of that is high thermal generation rate in comparison with photoionization rate under radiation. A comprehensive review of different direct detection detectors up to 1994 is

Table 2. Requirements for future space applications (after Ref. 30).

| Science             | Future opportunities       | Requirements                     |             |        |
|---------------------|----------------------------|----------------------------------|-------------|--------|
|                     |                            | NEP (W/Hz)                       | $\tau$ (ms) | Format |
| CMB polarization    | Inflation probe            | $(1\text{--}5) \times 10^{-18}$  | 1–30        | $10^4$ |
| Galaxy evolution    | SPICA/BLISS                | $(3\text{--}30) \times 10^{-20}$ | 100         | 5000   |
| Star formation      | SAFIR/CALISTO imaging      | $3 \times 10^{-19}$              | 10          | $10^5$ |
| Circumstellar disks | SAFIR/CALISTO spectroscopy | $3 \times 10^{-20}$              | 100         | $10^5$ |
|                     | SPIRIT                     | $1 \times 10^{-19}$              | 0.2         | 256    |

Table 3. Parameters of some uncooled THz wave detectors (after Ref. 36).

| Detector type                   | Modulation frequency (Hz)   | Operation frequency (THz) | Noise equivalent power (W/Hz <sup>1/2</sup> )  |
|---------------------------------|---|---------------------------|--|
| Golay cell                      | 20  | 30                        | 10 <sup>-9</sup> –10 <sup>-10</sup>  |
| Piezoelectric                   | 10 <sup>2</sup> (decreases with $f$ increasing and depends on dimensions) | 30                        | $\approx (1-3) \times 10^{-9}$ (decreases with $\nu$ increase)                             |
| VO <sub>x</sub> microbolometers | 10 <sup>2</sup>   | 4.3                       | $> 3 \times 10^{-10}$ (increases with $\nu$ increase)                                      |
| Bi microbolometer               | 10 <sup>6</sup>   | 3                         | $1.6 \times 10^{-10}$ (increases with $\nu$ increase)                                      |
| Nb microbolometer               | –   | 30                        | $5 \times 10^{-11}$  |
| Ti microbolometer               | 530   | 0.3                       | $4 \times 10^{-11}$  |
| Ni microbolometer               | 30  | 0.094                     | $1.9 \times 10^{-11}$  |
| Schottky diodes                 | 10 <sup>10</sup>  | 10                        | 10 <sup>-10</sup> (increases several orders with $\nu$ increase within $\sim 0.1$ –10 THz) |
| Schottky diode (zero biased)    | –   | –                         | $1.5 \times 10^{-12}$ (no incident power)  |
| Mott diodes                     | –   | 0.1                       | $1 \times 10^{-12}$  |
| Si MOSFET                       | $3 \times 10^4$   | 0.645                     | $\approx 3 \times 10^{-10}$ (depends on gate length and gate voltage)                      |
| Si FET                          | –   | 0.7                       | $> 10^{-10}$ (depends on gate length and gate voltage)                                     |
| Si CMOS                         | –   | –                         | $5 \times 10^{-11}$  |
| SiN membrane                    | 200   | $\approx 1.6$ –4.3        | 10 <sup>-9</sup>   |
| Micro-Golay cell                | 30  | 0.105                     | $3 \times 10^{-7}$   |
| HgCdTe HEB                      | $< 10^8$  | $\approx 0.03$ –1.5       | $\sim 4 \times 10^{-10}$ ( $\nu \approx 37$ GHz, increases with $\nu$ increase)            |

carried out in Ref. 41. Some kind of new cooled detectors are considered in Refs. 49 and 50.

A schematic diagram of a direct detection is shown in Fig. 11. Detector detects both signal radiation with the signal power  $W_s$  and background radiation with the power  $W_B$ . Focusing optics (lenses, mirrors, horns, etc.) is used to collect radiation over a large area to focus it to detector. Frequently, an optical filter is located before detector to remove background radiation at wavelengths other than the detected signal. A relatively small electrical signal from detector is amplified by amplifier and the generated signal  $I_s$  is further processed.

It can be shown that for direct detection with non-photoconductive detector, when fluctuation noise (background flux fluctuations) predominates, the minimum detectable

signal in background limited performance (BLIP) conditions is equal to [51,52]

$$W_{s,dir}^{min} = \frac{2h\nu}{\eta} W_B \Delta f^{1/2}, (W), \quad (3)$$

where  $\eta$  is the detector quantum efficiency (coupling efficiency) and  $\Delta f$  is the bandwidth.

It is seen that  $W_{s,dir}^{min} \sim (\Delta f)^{1/2}$  and detectable signal can be appreciably weaker than  $W_B$ . From this expression, one can also see that when comparing detectors, it is useful to normalize them to  $(\Delta f)^{1/2}$  which is done comparing NEP of different detectors.

At the condition that fluctuation noise is in the signal flow itself ( $W_{s,dir}^{min} = W_B$ ) for non-photoconductive direct detector for minimum detectable signal it follows

$$W_{s,dir}^{min} = \frac{2h\nu}{\eta} \Delta f, (W). \quad (4)$$

It means that to detect a minimum current, there should be accepted at least two photons by detector ( $\eta = 1$ ). Then, for the radiation frequency  $\nu = 1$  THz  $W_{s,dir}^{min} \approx 6.6 \times 10^{-22}$  W ( $\Delta f = 1$  Hz). But, the ability to detect such signals by direct detection detectors is limited by irreducible background photon noise not vanishingly small even for cosmic background. Performance of these detectors is background noise limited compared to heterodyne detectors, which performance is quantum noise limited. As a rule, the threshold power detected by direct detectors is higher, that is caused by other noises present both in detector itself and in circuit elements, and amplifiers.

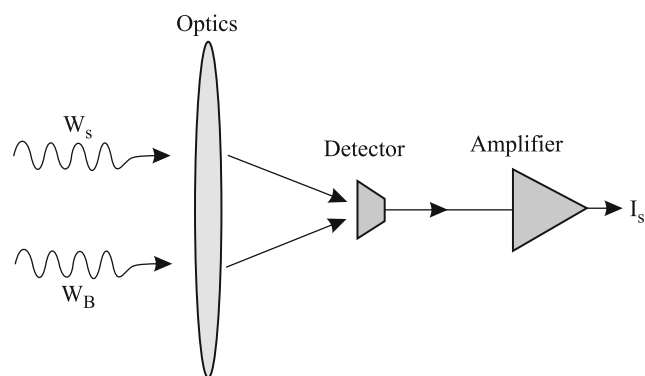


Fig. 11. Schematic representation of a direct detection.  $W_s$  is the signal power and  $W_B$  is the background radiation power.



For BLIP detection, when normalizing detector  $NEP$  to  $(\Delta f)^{1/2}$ , from Eq. (3) it follows

$$NEP_{dir} = \frac{2h\nu}{\eta} W_B^{1/2}, \quad (W/Hz^{1/2}). \quad (5)$$

The lower  $NEP$  means the more sensitive detector.

An advantage of systems with direct detection is relative simplicity and possibility of designing large format arrays [53–57]. Most imaging systems used passive direct detection. In active systems, for operation of which the scene is illuminated, heterodyne detection can also be used in order to increase sensitivity to low radiant levels or to image through the scattering media.

## 4.2. Heterodyne detection

In heterodyne detectors, the signals with THz frequencies are down-converted to intermediate frequency (IF), preserving the amplitude and phase information of the incoming radiation. In the last several decades, the detectors are of choice for high resolution spectroscopic studies, cosmic remote sensing, and relatively recently, for mm and sub-mm imaging [1–3].

A schematic of heterodyne detection is shown in Fig. 12. In addition to the signal  $W_s$  and the background  $W_B$  radiant powers, the radiant power  $W_{LO}$  from a local oscillator is added. LO is required to drive the mixing process. Basic element of mm or sub-mm heterodyne detector is a mixer, which is needed to align  $W_s$  and  $W_{LO}$  for generating a copy of a signal at the intermediate frequency  $\nu_{IF} = |\nu_s - \nu_{LO}|$  and its key component is the nonlinear mixing element (detector) at which the signal and LO radiant powers are coupled using some kind of diplexer or a beam splitter for IR region. The latter one spatially combines the signal beam and LO-beam.

Mixer is the most important component of heterodyne receiver input stage that is responsible for its responsivity. Its conversion loss enhancement decreases contribution into the noise heterodyne receiver temperature and consequent intermediate frequency amplifier. Signal power losses occur at diplexer and detector, but it is a mixer and its distributing circuits, which contribute the most noise to heterodyne receiver [58]. To be used in mm or sub-mm array, the mixer choice is dictated by the available LO power in these spectral range, mixer operating temperature and sensitivity needed.

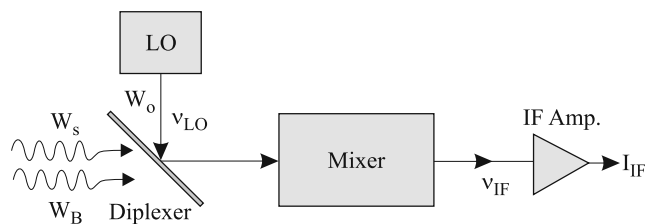


Fig. 12. Simplified schematic representation of heterodyne receiver.  $W_s$  is the signal power with the frequency  $\nu_s$ ,  $W_B$  is the background radiation power,  $W_o$  is the local oscillator radiation power with the frequency  $\nu_{LO}$ ,  $\nu_{IF}$  is the intermediate frequency.

Dependent on the availability of suitable LOs, two heterodyne techniques are possible. One can use a tuneable LO and a fixed IF amplifier with filters. Another one uses a fixed frequency LO in combination with IF amplifiers and filters to cover the needed frequency range. The first one is more flexible but tuneable continuous wave sources (such as, e.g., backward wave oscillators or frequency multiplied millimetre wave sources) produce low power at wavelengths less than 500  $\mu\text{m}$ , which can be not enough, e.g., for detection with Schottky barrier diode (SBD) receivers. The available narrow linewidth sources with sufficient power, as an LO for SBDs, are optically pumped sub-mm gas lasers or quantum cascade lasers (QCLs) for shorter part of sub-mm range. Although many CW lines are available from the gas lasers, these are all at specific wavelengths and heterodyne detection is restricted to a relatively narrow range on either side of each available wavelength [e.g., gas lasers at  $\lambda = 433 \mu\text{m}$  (HCOOH), at  $\lambda = 184, 214$ , and  $288 \mu\text{m}$  ( $\text{CH}_2\text{F}_2$ ),  $\lambda = 337 \mu\text{m}$  (HCN),  $\lambda = 118 \mu\text{m}$  ( $\text{H}_2\text{O}$ ), and others].

The serious problem, which limits an advent of heterodyne sensor arrays in sub-mm (THz) spectral region [e.g., for high-resolution spectroscopy applications ( $\nu/\Delta\nu \approx 10^6$ ) or photometry ( $\nu/\Delta\nu \approx 3\text{--}10$ ) and imaging], lies in technology limitations of solid-state local oscillator (LO) power. With an exception of free electron lasers that use relativistic electrons and are capable of reaching kilowatt level terahertz power [59], other THz source generate milliwatt or microwatt power levels (see Fig. 7). Traditional electronic devices, such as transistors, do not work well much above about 150 GHz. Therefore there are no amplifiers available throughout most of the THz band. Similarly, semiconductor lasers that have long been available in optical and IR bands, are not available in most of the THz band. Although much progress is being made in the area of high frequency transistors [60] and semiconductor lasers [61], it seems clear that, the so-called, “THz gap” will remain an important challenge to scientists and engineers for foreseeable future.

The primary benefit of heterodyne detection systems is that the frequency and phase information at the signal frequency  $\nu_s$  is converted to the frequency  $\nu_{IF}$ , which is in much lower frequency band ( $\nu_{IF} \ll \nu_s$ ) appropriate to electronics time response. This transformation ( $\nu_s \rightarrow \nu_{IF}$ ) is called heterodyne conversion. If the signal and LO frequencies are equal, then  $\nu_{IF} = 0$  and the beat tone degenerates to DC, and such detection process is called homodyne conversion.

Any nonlinear electronic device can be used as a mixer. However, to achieve efficient conversion and low noise in mm and sub-mm wavelength bands, only several types of detectors can be used. Frequently used mixers are devices having a strong electric field quadratic nonlinearity. Examples are forward biased Schottky barrier diodes (SBDs), superconductor-insulator-superconductor (SIS) tunnel junctions, semiconductor and superconducting hot electron bolometers (HEBs), and superlattices (SLs). Schematic current-voltage characteristics of these devices are shown in Fig. 13. Simultaneously with reasonable conversion effi-

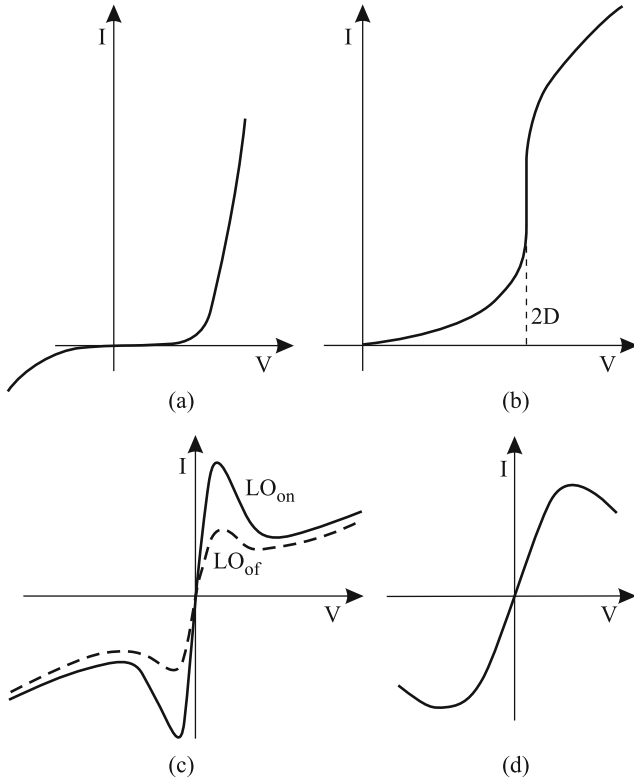


Fig. 13. Schematic of I-V characteristics of nonlinear elements on which THz heterodyne receivers are based: (a) Schottky diode, (b) SIS, (c) HEB, and (d) SL.

ciency and low noise, these nonlinear devices should possess high conversion operation speed for assurance of wide bandpass for consequent signals amplification at much lower frequencies 1–30 GHz.

At large LO power  $W_o$  one can detect the relatively small signal powers  $W_s$ . When this condition is abide by  $W_o \gg W_s$ , the quantum noise in the signal flux can be the dominant noise, and for internal signal gain  $G = 1$  for non-photoconductive detector at signal-to-noise ratio  $S/N = 1$ , it follows [51,52]

$$W_{s,het}^{min} = \frac{h\nu}{\eta} \Delta f, (W), \quad (6)$$

and for minimal detectable energy one has  $E_{s,het}^{min} = h\nu/\eta$ . For the coupling efficiency  $\eta = 1$  it means the quantum limit of signal detection. Thus, the energy of one photon accepted by non-photoconductive detector is transformed into the kinetic energy of one electron, which then crosses the barrier.

For heterodyne detection in BLIP regime, it can be shown [52], that

$$NEP_{het} = \frac{W_{s,het}^{min}}{\Delta f} = \frac{h\nu}{\eta}, (W/Hz). \quad (7)$$

In heterodyne detection, the possible minimum detectable signal is twice lower in comparison with direct detection [see Eqs. (4) and (6)]. Note also, that for heterodyne detection, units of  $NEP$  are W/Hz instead of  $W/Hz^{1/2}$  [see

Eq. (5)] as for direct detection. But frequently  $NEP$  still is cited in units of  $W/Hz^{1/2}$ .

A key advantage of mm and sub-mm sensors over infrared and visible ones is ultimate noise limits. Both direct and heterodyne detectors operate against fundamental noise limits that depend on the background radiation and the photon frequency. In the coherent case, the limit is simply the photon shot noise that has  $NEP$  equal to  $h\nu\eta$ . This limit is plotted in Fig. 14 for  $\eta = 1$  in terms of the photon energy  $h\nu$  and the equivalent temperature  $T = h\nu/k_B$ . The same advantage is shared by RF receivers operating at lower frequencies, which is one of the reasons for RF communications, be it wired or wireless, is generally superior to photonic communications in terms of sensitivity [15].

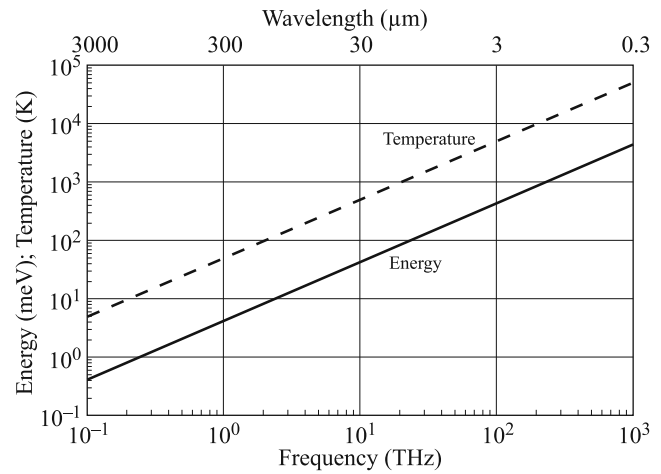


Fig. 14. Quantum-limit defined by the minimum energy – one photon – per spatial mode from the mm-wave region through the visible region (after Ref. 15).

The sensitivity of heterodyne detectors is frequently given in terms of the mixer noise temperature  $T_{mix}$ , which correlates with the mixer noise equivalent power

$$NEP_{mix} = k_B T_{mix}. \quad (8)$$

For the wavelength band  $\lambda \approx 3$  mm ( $\nu \approx 100$  GHz), where it is atmospheric transparency window, the value  $T_s^{min} = E_{s,het}^{min}/k_B = h\nu/k_B \approx 4.8$  K is the fundamental limit to the noise temperature imposed by the uncertainty principle on any simultaneous measurement of the amplitude and phase of the electromagnetic wave (see Fig. 14). In the case of heterodyne detection with SIS tunnel junctions as the mixing elements, “the true quantum-noise limited mixer temperature is  $T_{mix}^{min} = h\nu/2k_B$ ” [62].

The limit values of noise temperature of heterodyne THz detectors are frequently compared using  $T_s^{min}$ -values. Since heterodyne detectors measure both amplitude and phase simultaneously, they are governed by the uncertainty principle, and hence they are quantum-noise limited to an absolute noise-floor of 48 K/THz.

THz mixer receivers can operate in different modes, depending on the configuration of the receiver and the

nature of the measurement. The signal and image frequencies may be separated in the correlator, or the image may be removed by appropriate phase switching of pairs of local oscillators. The function of separating or dumping the image in the receiver is to remove some of the uncorrelated noise to improve the system sensitivity.

In single-sideband (SSB) operation, the receiver is configured so that, at the image sideband, the mixer is connected to a termination within the receiver. There is no external connection to the image frequency, and the complete receiver is functionally equivalent to an amplifier followed by a frequency converter.

In double-sideband (DSB) operation, on the other hand, the mixer is connected to the same input port at both upper and lower sidebands. The DSB receivers can be operated in two modes:

- in SSB operation to measure narrow-band signals contained entirely within one sideband – for detection of such narrow-band signals, power collected in the image band of a DSB receiver degrades the measurement sensitivity
- in DSB operation to measure broadband (or continuum) sources whose spectrum covers both sidebands – for continuum radiometry, the additional signal power collected in the image band of a DSB receiver improves the measurement sensitivity.

The technology that has traditionally been available for terahertz receivers utilizes Schottky-barrier diode (SBD) mixers pumped by gas laser local oscillators. The noise temperature of such receivers has essentially reached a limit of about  $50h\nu/k$  in the frequency range below 3 THz (see Fig. 15). Above 3 THz, there occurs a steep increase, mainly due to increasing losses of the antenna and reduced performance of the diode itself. In the last two decades, impressive improvements in receiver sensitivities have been achieved using superconducting mixers, with both SIS and HEB mixers. In Fig. 15, selected receiver noise temperatures are plotted. Nb-based SIS mixers yield almost quantum limited performance up to gap frequency of 0.7 THz.

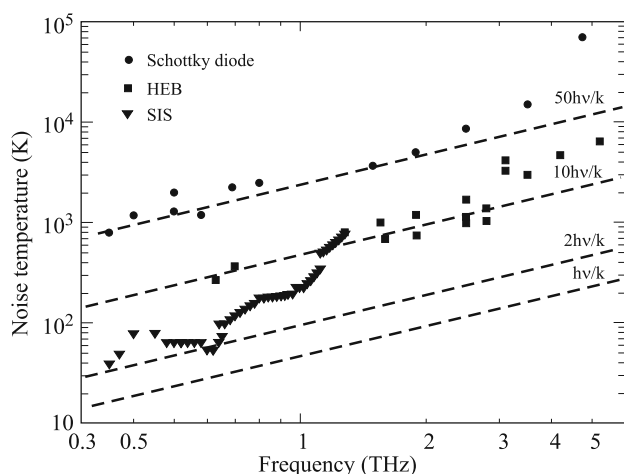


Fig. 15. Noise temperature of Schottky diode mixers, SIS mixers and HEB mixers operated in terahertz spectral band (after Ref. 48).

Unlike SBD and SIS mixers, the HEB mixer is a thermal detector. Up to 2.5 THz, the noise temperature follows closely the  $10h\nu/k$  line. In comparison with Schottky-barrier technology, HEB mixers require three to four orders of magnitude less LO power.

Heterodyne detectors are mostly used in investigations of CMB radiation measurements at mm and sub-mm wavelengths. Typical receiver includes conical antenna, HEMT amplifier, band pass filter and SIS, or superconducting HEB detector. HEMT amplifiers can be cooled to cryogenic temperatures to minimize their noise.

### 4.3. Heterodyne vs. direct detection

One of the critical questions, especially for space-borne observatories at sub-mm wavelengths, is whether to use heterodyne or direct detector instruments for spectroscopic studies. In general, heterodyne detection offers higher spectral resolution  $\nu/\Delta\nu \sim 10^5$ – $10^6$ . Very high spectral resolution is possible, since  $\nu_{IF} \ll \nu$ . But for heterodyne systems, especially for SBD receivers in THz region, a critical component is the LO source.

At the same time, direct detection detectors, as a rule operating in wider spectral range, when, e.g., photon background is low, can provide sufficient resolution. They are preferable for moderate spectral resolution  $\nu/\Delta\nu \sim 10^3$ – $10^4$  or lower and they are also preferable for imaging [63]. Direct detectors can be used in those applications where sensitivity is more important than the spectral resolution.

Having background limited detector array is important from the point of removing of, e.g., sky background noise, taking into consideration that any spatially correlated component of this noise detected in all detectors in the array can be substantially suppressed.

Among the direct detectors, low-temperature bolometers currently offer the highest sensitivity from the far-infrared to millimetre-wave region of the electromagnetic spectrum providing background limited performance with  $NEP$  up to  $\sim(0.4\text{--}3)\times 10^{-19}$  W/Hz<sup>1/2</sup> at operation temperature  $\sim 100$ – $300$  mK [7,47,64,65]. Direct detection bolometers have been used for decades in measurements of CMB spectrum and anisotropy, including space flight COBE-FIRAS instrument [66]. In CMB experiments, coherent detector systems and incoherent bolometric systems are used. For cosmic ground-based experiments, both detector types are viable [67].

Compared to direct detection, heterodyne detection exhibits both advantages and disadvantages [52]. Among the advantages of heterodyne detection are:

- it can detect frequency modulation and phase modulation,
- dominant noise follows from fluctuations in  $W_{LO}$  rather than from background radiation noise, thus providing discrimination, e.g., against background flux, microphonics etc.,
- IF conversion process provides gain, so that IF detector signal output may be made large to override, e.g., thermal and generation-recombination noise,

- conversion gain is proportional to  $W_{LO}/W_s$  and thus, much weaker radiant signal powers compared to direct detection can be detected.

Among the disadvantages of heterodyne detection are:

- both beams should be coincident and equal of diameter, and also their Pointing vectors should be coincident,
- wavefronts of both beams should have the same radius of curvature and have the same transverse spatial mode structure, moreover they should be polarized in the same direction,
- difficulty of producing large format arrays.

Coherent detection systems (with SIS or SBD mixers), as a rule, are limited in detection signals with the frequencies above 1 THz. Heterodyne superconducting HEB mixers, TES and microwave kinetic inductance detectors (MKIDs) direct detection detectors have almost no practical limitations in applications in shorter sub-mm range. In this spectral band, both antenna-coupled detectors and detectors itself (except, e.g., HEB detectors) for radiation detection can be used.

## 5. Photoconductive THz generation and detection

Before the mid-1970s, the only viable source for THz radiation was a thermal source. This changed in 1975, when Auston of Bell Labs demonstrated that a short laser pulse (on the order of 100 fs and with a wavelength above the bandgap) impinging on a biased semiconductor would create a picosecond current transient [68]. This time-dependent current radiates and contains frequency components in the THz frequency range. This pioneering source for a THz pulse called the “Auston switch” led to the development of photoconductive [69] and electro-optic methods [70] to generate and detect radiation in the THz frequency range.

In typical photoconductive switch [see Fig. 16(a)], two biased parallel metal strip lines, called the “Grischowsky antenna” [71], with a typical separation of several micrometers are embedded in a semiconductor substrate [14]. The THz pulse is generated when fs-laser pulse is focused near the anode of the antenna thereby creating free charge carriers,

which are accelerated in the electric field between the striplines. These are radiated into the substrate (and in opposite direction) and collimated by a hyperhemispherical lens with high resistivity silicon for better coupling of THz radiation to the free space (free space impedance  $Z \approx 377 \Omega$ ).

The photoconductive detection of broadband THz radiation is based on antenna structures similar to those used for generation of pulsed broadband THz radiation emission spectra and is used in time domain spectroscopy (TDS) experiments or imaging (see Fig. 17) [14,73,74]. Each pulse of a femtosecond laser producing an optical-pulse train separates into two paths. One reaches the THz emitter, such as a photoconductive antenna, semiconductor wafer or nonlinear crystal, where the optical pulses are transformed into ultrashort electromagnetic pulses. These pulses propagate in free space, and are focused onto an ultrafast detector, such as low-temperature grown (LTG) GaAs photoconductive switch or electro-optic crystal. The second part of the pulse is also delivered onto the detector after passing through a time-delay stage.

Unfortunately, LTG detector sensitivities or changes in optical polarization of electro-optical cells are small due to the weakness of the THz fields and nonlinear effect. Because of these circumstances, to obtain an image (only in the active mode) with their help, one needs to move, e.g., the object mechanically, and it takes at least several minutes.

Figures 16(b) shows a schematic illustration of the photoconductive antenna sensor (detector). It consists of an H-shaped stripline structure deposited on a semiconductor substrate. In analogy to the emitter switch, an incoming fs laser beam (from the same fs laser), which is focused between protruding parts of the electrodes, injects free carriers leading to a drop of the resistance across the switch below about a hundred ohms. The electric field of the focused incoming THz radiation from fs laser, induces a transient bias voltage across the 1–5- $\mu\text{m}$  gap between the two arms of this receiving antenna. Thus, when the laser pulse coincides spatially and temporally with the THz electric field of the incoming THz radiation, a photocurrent is induced that is proportional to the incident electric field. By delaying the laser pulse, relative to the THz pulse, the time-dependence

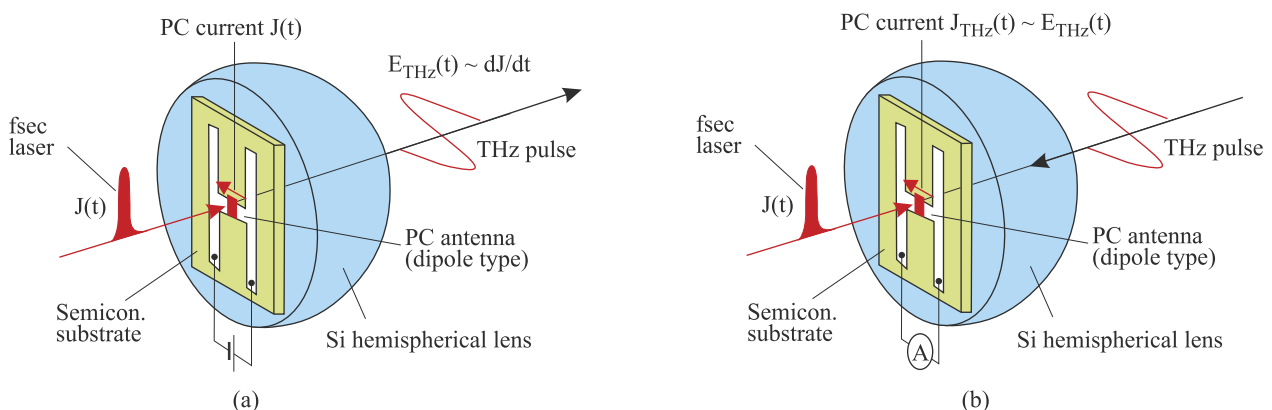


Fig. 16. Photoconductive emitter (a) and photoconductive detector antenna (b) mounted on a hemispherical lens (after Ref. 72).



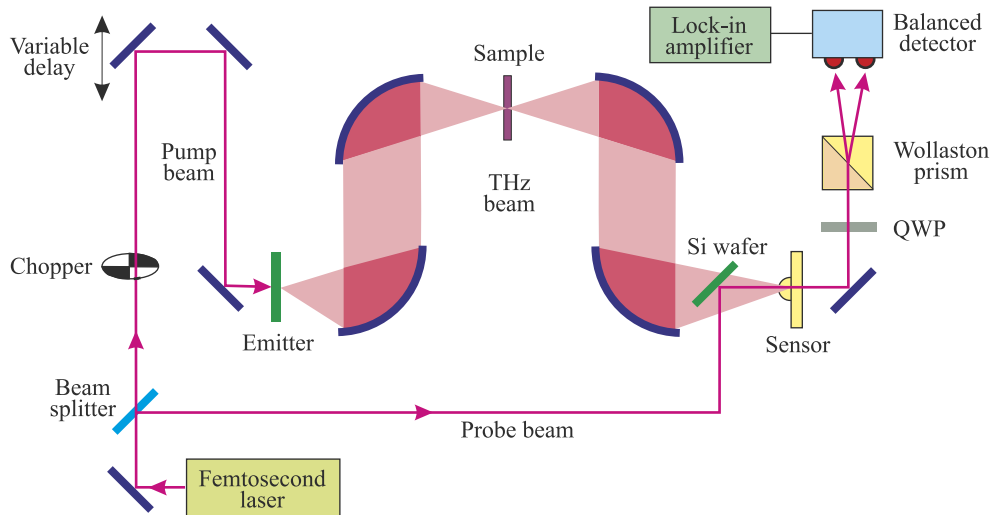


Fig. 17. Schematic diagram of THz-TDS system. The emitters are typically made from a GaAs photoconductive switch, semiconductors (InAs, ZnTe, GaSe) and nonlinear crystals (DAST, GaP). The sensors are often a GaAs photoconductive switch or electro-optic crystals (ZnTe, GaSe, GaAs, DAST). In the second case a quarter wave plate (QWP), Wollaston prism and balanced detectors are used.

of the photocurrent can be measured. Since the laser pulse is narrow in comparison to the time duration of the THz pulse from laser induced semiconductor emitter [Fig. 16(b)], the laser acts as a gated sampling signal.

The detectors as photoconductive antennas (see Fig. 16) on the base of highly resistive semiconductors (e.g., low temperature grown GaAs [75–77] or narrow-gap InGaAs [78]) are frequently used in TDS technique. During the laser pulse, the excited carriers are accelerated by the electrical field component of the incident THz pulse with the time-dependent electrical field  $E(t)$ . The current signal, which arises in outer circuit, can be analysed by inverse Fourier transform procedure. The photoconductive antenna can be considered as a dipole of the length  $L$ , which is in resonance with the radiation wavelength  $\lambda_n$  inside the semiconductor. The resonance condition is  $L = m(\lambda/2n)$ , where  $m$  is the integer and  $n$  is the semiconductor refractive index.

The time domain signal  $I(\tau)$  (where  $\tau$  is a delay time), is the convolution of THz pulse electric field  $E(t)$  and the detector response  $D(t)$

$$I(t) = \frac{1}{T} \int_0^T E(t)D(t - \tau)dt. \quad (9)$$

If the detector response is a delta function, the time domain signal would be equal to the electric field. In the real situation, the bandwidth of the pulse is limited by the detector response. The reason for this is that the analysis is performed by dividing the sample signals with the reference signal in the frequency domain where the time domain convolution becomes a product leaving only the ratio of the electric fields.

There are quite a lot of designs of antennas (e.g., bow-type, horn structure, fractal) and publications devoted to this question [79–84].

## 6. General classification of THz detectors

The majority of THz detectors can be classified in two broad categories: photon detectors and thermal detectors.

### 6.1. Photon detectors

In photon detectors, the radiation is absorbed within the material by interaction with electrons either bound to lattice atoms or to impurity atoms or with free electrons. The observed electrical output signal results from the changed electronic energy distribution. The fundamental optical excitation processes in semiconductors are illustrated in Fig. 18. The photon detectors show a selective wavelength dependence of response per unit incident radiation power (see Fig. 19). They exhibit both good signal-to-noise performance and a very fast response. But to achieve this, the photon detectors require cryogenic cooling. This is necessary to prevent the thermal generation of charge carriers. The thermal transitions compete with the optical ones, making non-cooled devices very noisy.

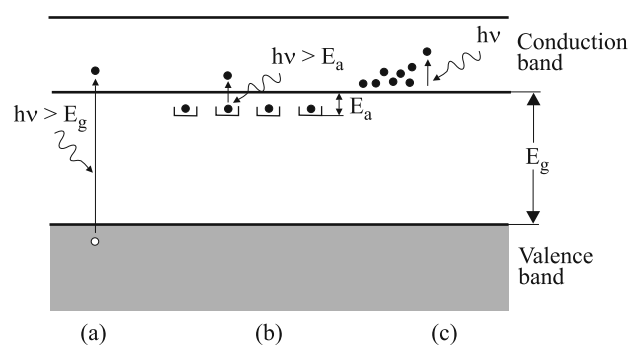


Fig. 18. Fundamental optical excitation processes in semiconductors: (a) intrinsic absorption, (b) extrinsic absorption, (c) free carrier absorption.

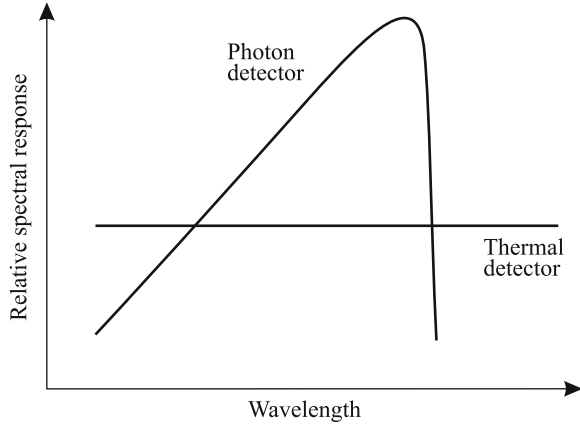


Fig. 19. Relative spectral response for a photon and thermal detectors.

The spectral current responsivity of photon detectors is equal to

$$R_i = \frac{\lambda \eta}{hc} qg, \quad (10)$$

where  $\lambda$  is the wavelength,  $h$  is the Planck's constant,  $c$  is the velocity of light,  $q$  is the electron charge, and  $g$  is the photoelectric current gain. The current that flows through the contacts of the device is noisy due to the statistical nature of the generation and recombination processes – fluctuation of optical generation, thermal generation, and radiative and nonradiative recombination rates. Assuming that the current gain for the photocurrent and the noise current are the same, the noise current is

$$I_n^2 = 2q^2 g^2 (G_{op} + G_{th} + R) \Delta f, \quad (11)$$

where  $G_{op}$  is the optical generation rate,  $G_{th}$  is the thermal generation rate,  $R$  is the resulting recombination rate, and  $\Delta f$  is the frequency band.

It was found by Jones [85] that for many detectors the NEP is proportional to the square root of the detector signal that is proportional to the detector area  $A_d$ . The normalized detectivity  $D^*$  (or  $D$ -star) suggested by Jones [85,86] is defined as

$$D = \frac{(A_d)^{1/2}}{NEP}. \quad (12)$$

The detectivity  $D^*$  is the main parameter to characterize normalized signal-to-noise performance of detectors, and can be also defined as

$$D = \frac{R_i (A_d \Delta f)^{1/2}}{I_n}. \quad (13)$$

The importance of  $D^*$  is that this figure of merit permits comparison of detectors of the same type, but having different areas. Either a spectral or blackbody  $D^*$  can be defined in terms of corresponding type of NEP.

At equilibrium, the generation and recombination rates are equal to each other. In this case

$$D = \frac{\lambda \eta}{2hc(Gt)^{1/2}}. \quad (14)$$

Background radiation frequently is the main source of noise in a detector. Assuming no contribution due to recombination,

$$I_n^2 = 2 B A_d \eta q^2 g^2 \Delta f, \quad (15)$$

where  $B$  is the background photon flux density. Therefore, at the background limited performance conditions (BLIP performance)

$$D_{BLIP} = \frac{\lambda}{hc} \frac{\eta}{B}^{1/2}. \quad (16)$$

Once background-limited performance is reached, the quantum efficiency  $\eta$ , is the only detector parameter that can influence a detector's performance.

Depending on the nature of the interaction, the class of photon detectors is further sub-divided into different types. The most important are: intrinsic detectors, extrinsic detectors, photoemissive (Schottky barriers). Different types of detectors are described in details in the monograph *Infrared Detectors* [86] and they are briefly characterized in Table 4. Figure 20 shows spectral detectivity characteristics of different types of THz detectors [87].

Photoconductors that utilize excitation of an electron from the valence to conduction band are called intrinsic detectors. Instead those which operate by exciting electrons into the conduction band or holes into the valence band from impurity states within the band (impurity-bound states in energy gap, quantum wells or quantum dots), are called extrinsic detectors. A key difference between intrinsic and extrinsic detectors is that extrinsic detectors require much

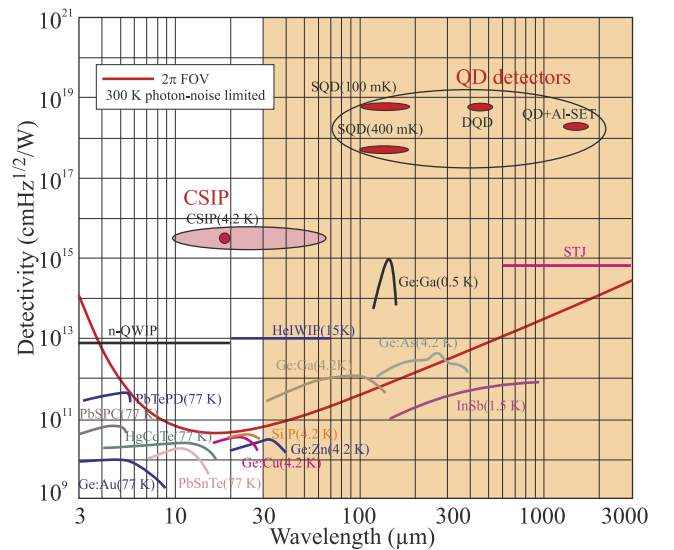
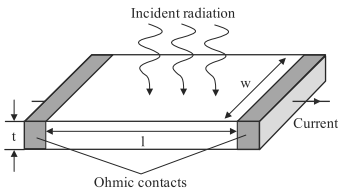
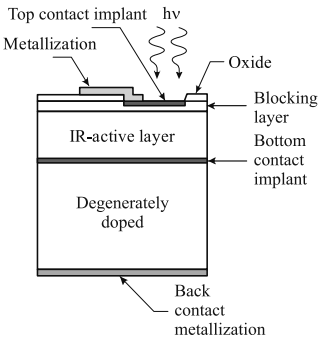
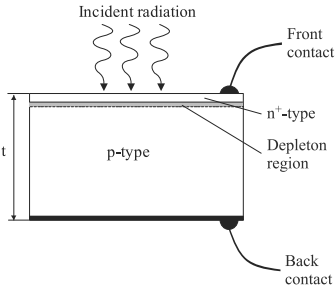
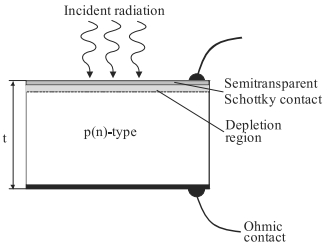
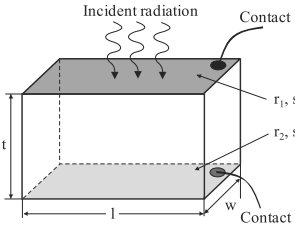


Fig. 20. Spectral dependence of detectivity of various infrared detectors (adapted after [87]).

Table 4. Photon detectors.

| Mode of operation              | Schematic of detector   | Operation and properties   |
|--------------------------------|---|--|
| Photoconductor                 |    | <p>It is essentially a radiation-sensitive-resistor, generally a semiconductor, either in thin-film or bulk form. A photon may release an electron-hole pair or an impurity-bound charge carrier, thereby increasing the electrical conductivity. In almost all cases, the change in conductivity is measured by means of electrodes attached to the sample. For low resistance material, the photoconductor is usually operated in a constant current circuit. For high resistance photoconductors, a constant voltage circuit is preferred and the signal is detected as a change in current in the bias circuit.</p>  |
| Blocked impurity band detector |    | <p>The active region of BIB detector structure, usually based on epitaxially grown n-type material, is sandwiched between a higher doped degenerate substrate electrode and an undoped blocking layer. Doping of active layer is high enough for the onset of an impurity band in order to display a high quantum efficiency for impurity ionization (in the case of Si:As BIB, the active layer is doped to <math>\approx 5 \times 10^{17} \text{ cm}^{-3}</math>). The device exhibits a diode-like characteristic, except that photoexcitation of electrons takes place between the donor impurity and the conduction band. The heavily doped n-type IR-active layer has a small concentration of negatively charged compensating acceptor impurities. In the absence of an applied bias, charge neutrality requires an equal concentration of ionized donors. Whereas the negative charges are fixed at acceptor sites, the positive charges associated with ionized donor sites (<math>D^+</math> charges) are mobile and can propagate through the IR-active layer via the mechanism of hopping between the occupied (<math>D^0</math>) and the vacant (<math>D^+</math>) neighboring sites. A positive bias to the transparent contact creates a field that drives the pre-existing <math>D^+</math> charges towards the substrate, while the undoped blocking layer prevents the injection of new <math>D^+</math> charges. A region depleted of <math>D^+</math> charges is therefore created, with a width depending on the applied bias and on the compensating acceptor concentration.</p> |
| p-n junction photodiode        |  | <p>It is the most widely used photovoltaic detector, but rather rarely used as THz detector. Photons with energy greater than the energy gap create electron-hole pairs in the material on both sides of the junction. By diffusion, the electrons and holes generated within a diffusion length from the junction reach the space-charge region where they are separated by the strong electric field; minority carriers become majority carriers on the other side. This way a photocurrent is generated causing a change in voltage across the open-circuit cell or a current to flow in the short-circuited case. The limiting noise level of photodiodes can ideally be <math>\sqrt{2}</math> times lower than that of the photoconductor, due to the absence of recombination noise. Response times are generally limited by device capacitance and detector-circuit resistance.</p>   |
| Schottky barrier photodiode    |  | <p>Schottky barrier photodiode reveals some advantages over p-n junction photodiode: fabrication simplicity (deposition of metal barrier on n(p)-semiconductor), absence of high-temperature diffusion processes, and high speed of response. Since it is a majority carrier device, minority carrier storage and removal problems do not exist and therefore higher bandwidths can be expected. The thermionic emission process in Schottky barrier is much more efficient than the diffusion process and therefore for a given built-in voltage, the saturation current in a Schottky diode is several orders of magnitude higher than in the p-n junction.</p>  |
| Dember detector                |  | <p>Dember detector, rather rarely used as THz detector, is a type of photovoltaic device based on bulk photodiffusion voltage in a simple structure with only one type of semiconductor doping supplied with two contacts. When radiation is incident on the surface of a semiconductor generating electron-hole pairs, a potential difference is usually developed in the direction of the radiation as a result of difference in diffusion of electrons and holes. The Dember effect electrical field restrains the electrons with higher mobility, while holes are accelerated, thus making both fluxes equal.</p>  |

cooling to achieve high sensitivity at a given spectral response cutoff in comparison with intrinsic detectors. Low-temperature operation is associated with longer-wavelength sensitivity in order to suppress noise due to thermally induced transitions between close-lying energy levels. Intrinsic detectors are most common at the short wavelengths, below 20  $\mu\text{m}$ . Terahertz photoconductors are operated in extrinsic mode. One advantage of photoconductors is their current gain which is equal to the recombination time divided by the majority-carrier transit time. This current gain leads to higher responsivity than is possible with nonavalanching photovoltaic detectors. However, series problem of photoconductors operated at low temperature is nonuniformity of detector element due to recombination mechanisms at the electrical contacts and its dependence on electrical bias.

Recently, interfacial workfunction internal photoemission (IWIP) detectors [88] and quantum well [89] and quantum dot detectors [20], which can be included to extrinsic photoconductors, have been proposed as THz sensors. The very fast time response of quantum well and quantum dot semiconductor detectors make them attractive for THz heterodyne detection and THz free space communications.

A schematic diagram of the architecture of a p-type IWIP structure is shown in Fig. 21(a). A typical IWIP consists of a doped emitter followed by an undoped barrier, which is in turn sandwiched in two highly doped contact layers. The top contact layer is formed as a ring surrounding the active area to minimize absorption loss. The detection mechanism is a three-stage process: free carrier absorption of the incoming photons in the emitter, internal photoemission, and collection of emitted carriers by an applied electric field across the contacts. The emitter-barrier junction introduces the workfunction  $\Delta$ , which corresponds to the energy difference between the top of the barrier and the Fermi level in the emitter. Carriers in the emitter with the energy  $> \Delta$  pass over the barrier, escape the emitter, and they are collected at the contact by an applied electric field, as shown in Fig. 21(b). If in IWIP detectors, both the emitter and barrier are made of the same material but with higher doping in the emitter they are called homojunction IWIP, while in a hetero-

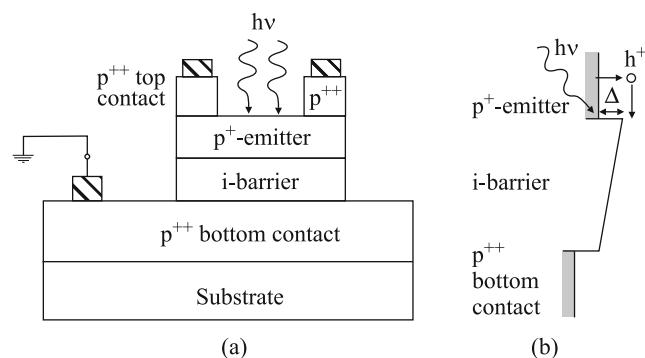


Fig. 21. p-type IWIP structure: (a) schematic diagram and (b) band diagram showing the valence band profiles of the structure under an electric field. The work function  $\Delta$  is also indicated.

ojunction IWIP structure the emitter and the barrier are made of materials with different bandgaps. A detailed explanation on designing and optimization of IWIP detectors can be found in Ref. 90. A comparative discussion of several IWIP detectors, based on p-type AlGaAs/GaAs, n-type GaAs/AlGaAs, n-type GaN/AlGaN, and p-type GaSb/GaSb, is presented in Ref. 88. The major problem of these detectors is the low quantum efficiency in the THz region. One approach to overcome this problem is the use of surface plasmons to enhance THz radiation absorption in the active layer of the structure.

Also quantum well (QW) and quantum dot (QD) structures are used in fabrication of THz detectors. In general, quantum dot infrared photodetectors (QDIPs) are similar to quantum well infrared photodetectors (QWIPs) but with the quantum wells replaced by quantum dots, which have size confinement in all spatial directions.

The energy position of QD (also QW) level essentially depends on geometrical sizes and even one monolayer variation of the size can significantly affect the energy of optical transition. Fluctuations of the geometrical parameters result in corresponding fluctuation of the quantum level over the array of dots. Random fluctuations also affect the density of states on nonuniform array of QDs.

Figure 22(a) shows the schematic layers of a QWIP and a QDIP. In both cases, the detection mechanism is based on the intraband photoexcitation of electrons from confined states in the conduction band wells or dots into the continuum. The emitted electrons drift towards the collector in the electric field provided by the applied bias, and photocurrent is created. It is assumed, that the potential profile at the con-

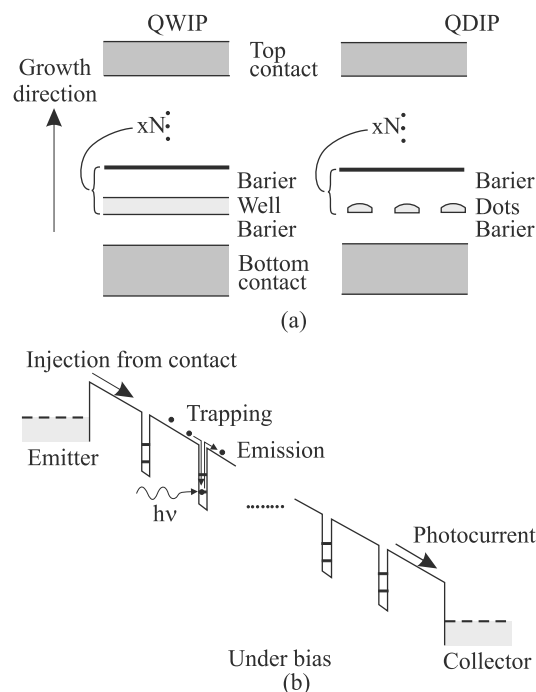


Fig. 22. Schematic layers of QWIP and QDIP (a) and potential profile for both structures under bias and (b). For QDIP, influence of wetting layer is neglected (after Ref. 91).



duction band edge along the growth direction for both structure have a similar shape as shown in Fig. 22(b). In fact, however, the potential distribution in the QW (QD) region is sag down to provide higher electric field from the emitter at least in several periods of structure.

The quantum well AlGaAs/GaAs structures are mainly grown by MBE on semi-insulating GaAs substrate [see Fig. 23(a)]. At present, GaAs substrates are available with diameter up to 8 inch, however, in QWIP processing lines are typically used 4 inch substrates. Process technology starts with epitaxial growth of structure with a periodic array of Si-doped ( $N_d \approx 10^{18} \text{ cm}^{-3}$ ) GaAs quantum wells and sequential growth of an etch-stop layer (usually AlGaAs) used for substrate removal. The QWIP active region is sandwiched between two n-type GaAs contact layers about 1- $\mu\text{m}$ -thick (also heavily doped to  $N_d \approx 10^{18} \text{ cm}^{-3}$ ), and an etch stop followed by a sacrificial layer for the grating. For optical coupling, usually 2D reflective diffraction gratings are fabricated. Further process technology includes etching mesas through the superlattice to the bottom contact layer, followed by ohmic contacts to the  $n^+$ -doped GaAs contact layers. These steps can be accomplished using wet chemical or dry etching techniques. In selective etching, usually ion beam etching is practical for patterning the grating coupler into each pixel.

The self-assembling method for fabricating QDs has been recognized as one of the most promising methods for forming QDs. In the crystal growth of highly lattice-mismatched materials system, self-assembling formation of na-

nometer-scale 3D islands has been reported. The lattice mismatch between a QD and the matrix is the fundamental driving force of self-assembling. In(Ga)As on GaAs is the most commonly used material system because lattice mismatched can be controlled by the In alloy ratio up to about 7%.

In a vertical QDIP [Fig. 23(b)], the photocurrent is collected through the vertical transport of carriers between top and bottom contacts. The device heterostructure comprises repeated InAs QD layers buried between GaAs barriers with top and bottom contact layers at active region boundaries. The mesa height can vary from 1 to 4  $\mu\text{m}$  depending on the device heterostructure. The quantum dots are directly doped (usually with silicon) in order to provide free carriers during photoexcitation, and an AlGaAs barrier can be included in the vertical device heterostructure in order to block dark current created by thermionic emission.

## 6.2. Thermal detectors

The second class of detectors is composed of thermal detectors. In a thermal detector, shown schematically in Fig. 24, the incident radiation is absorbed to change the material temperature, and the resultant change in some physical property is used to generate an electrical output. The detector is suspended on legs, which are connected to the heat sink. The signal does not depend upon the photonic nature of the incident radiation. Thus, thermal effects are generally wavelength independent (see Fig. 19), the signal depends upon the radiant power (or its rate of change) but not upon its spectral content. Since the radiation can be absorbed in a black surface coating, the spectral response can be very broad. Attention is directed toward three approaches which have found the greatest utility in infrared technology, namely, bolometers, pyroelectric and thermoelectric effects. In pyroelectric detectors, a change in the internal electrical polarization is measured, whereas in the case of thermistor bolometers a change in the electrical resistance is measured.

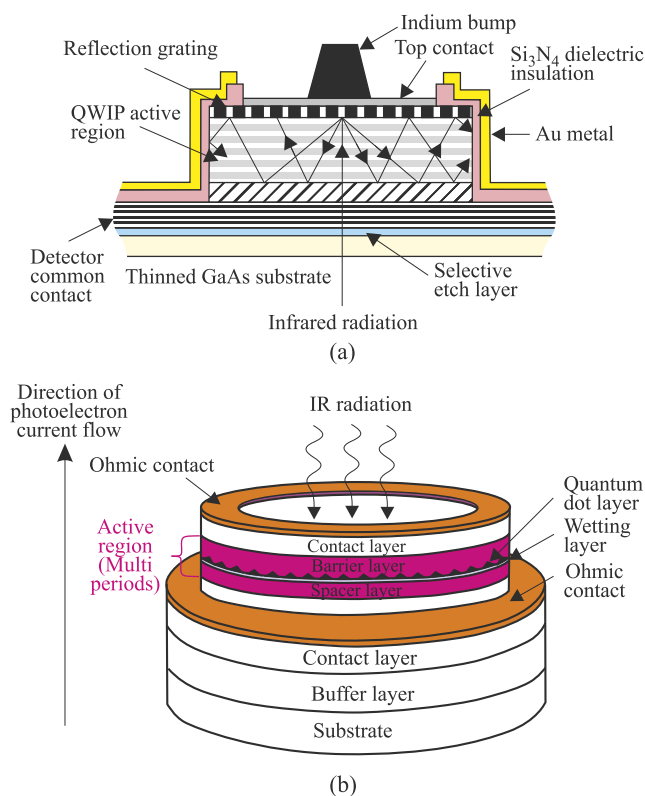


Fig. 23. Schematic diagram of QWIP (a) and QDIP (b).

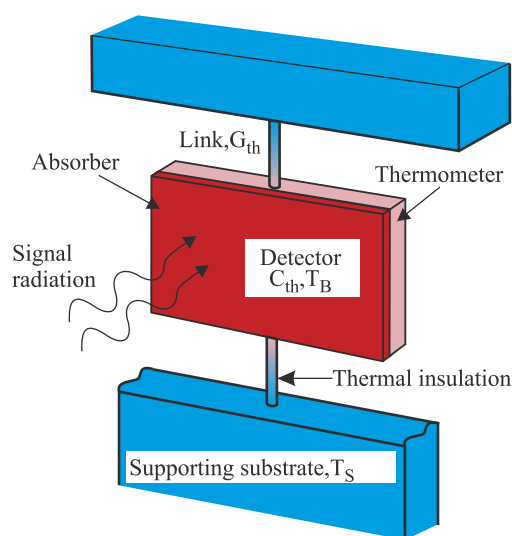


Fig. 24. Schematic diagram of thermal detector.

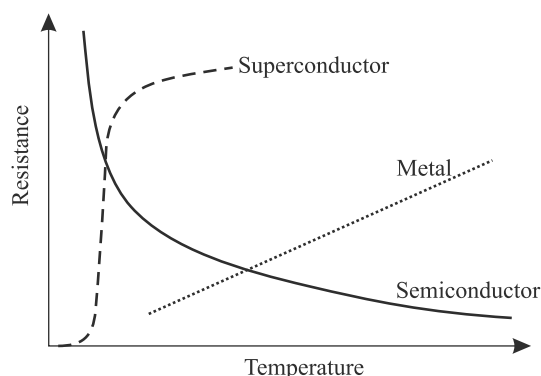


Fig. 25. Temperature dependence of resistance of three bolometer material types.

Usually, bolometer is a thin, blackened flake or slab, whose impedance is highly temperature dependent. Bolometers may be divided into several types. The most commonly used are the metal, the thermistor, and the semiconductor bolometers. A fourth type is the superconducting bolometer. This bolometer operates on a conductivity transition in which the resistance changes dramatically over the transition temperature range. Figure 25 shows schematically the temperature dependence of resistance of different types of bolometers.

In the simplest representation of the thermal detector shown in Fig. 24, the detector is represented by an absorbing element with the heat capacity  $C_{th}$ , which converts the incident radiation to heat, and which is attached to a heat sink (thermal reservoir) at the temperature  $T_S$  via the thermal conductance  $G_{th}$ . In the absence of a radiation input, the average temperature of the detector is constant, although it exhibits a fluctuation about this value. When the radiation input power  $P$ , is received by the detector, the temperature  $T_B$  of absorbing element initially increases with time at the rate  $dT_B/dt = P/C_{th}$  and approaches the limiting value  $T_B = T_S + P/G_{th}$  with the thermal time constant  $\tau_{th} = C_{th}/G_{th}$ . When the radiation is turned off, it relaxes back to  $T_S$  with the time constant  $\tau_{th}$ . Thermal detectors are frequently used to give a periodic response to a signal which is modulated at the frequency  $\approx 1/\tau_{th}$ .

The key trade-off with respect to conventional uncooled thermal detectors is between sensitivity and response time. The detector sensitivity is often expressed by noise equivalent temperature ( $NEDT$ ) represented by the temperature change, for incident radiation, that gives an output signal equal to the rms noise level. The thermal conductance is an extremely important parameter, since  $NEDT$  is proportional to  $(G_{th})^{1/2}$ , but the thermal response time of the detector  $\tau_{th}$ , is inversely proportional to  $G_{th}$ . Therefore, a change in thermal conductance due to improvements in material processing technique improves sensitivity at the expense of time response. Typical calculations of the trade-off between  $NEDT$  and time response carried out in Ref. 92 are shown in Fig. 26.

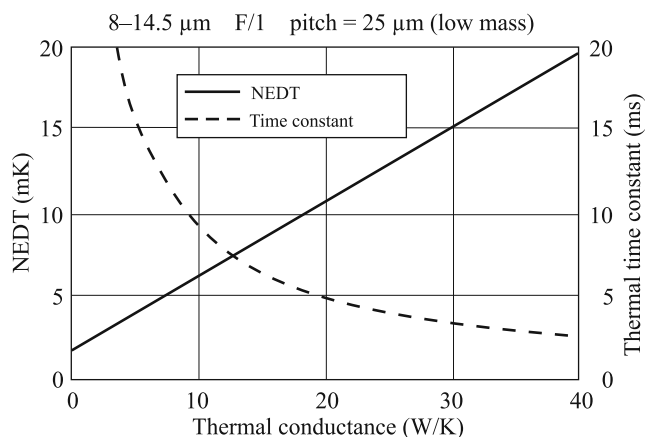


Fig. 26. Trade-off between sensitivity and response time of uncooled thermal imaging systems (after Ref. 92).

If the  $NEDT$  is dominated by a noise source that is proportional to  $G_{th}$ , what has the place when Johnson and  $1/f$  noises are dominated, and since  $\tau_{th} = C_{th}/G_{th}$ , then the figure of merit given by

$$FOM = NEDT \tau_{th}, \quad (17)$$

can be introduced for long wavelength IR bolometers [93]. Users are interested not only in the sensitivity, but also in their thermal time constants and the  $FOM$ , described by Eq. (17), recognizes the tradeoffs between thermal time constant and sensitivity. Figure 27 shows the dependence of  $NEDT$  on thermal time constant for two  $NEDT \times \tau_{th}$  products.

Many types of thermal detectors operated in LWIR and far-IR regions (including bolometers, pyroelectric detectors and Golay cells) are also used in THz band. The operation principles of thermal detectors are described in many books; see e.g., Refs. 94–96 and briefly described in Table 5.

Bolometers, as other thermal devices, for a long time were treated traditionally as slow devices. In many applications, their performance is limited by a trade-off between speed and sensitivity. For conventional uncooled microbolometers, operated in the wavelength range 10–100  $\mu\text{m}$  at

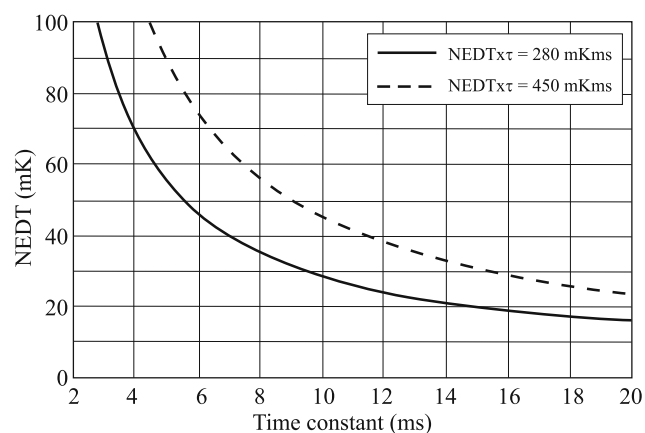
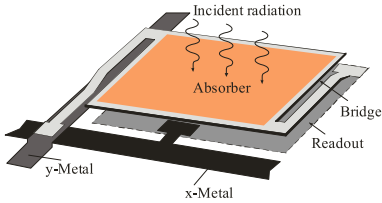
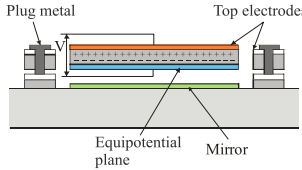
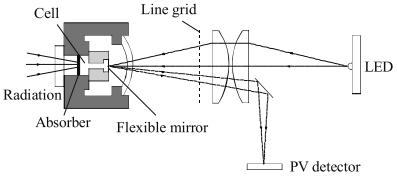


Fig. 27. Calculated microbolometer  $NEDT$  and the thermal time constant  $\tau_{th}$ , for two  $NEDT \times \tau_{th}$  products (after Ref. 93).

Table 5. Thermal detectors.

| Mode of operation   | Schematic of detector  | Operation and properties   |
|---|--|--|
| Bolometer<br>Metal<br>Semiconductor<br>Superconductor<br>Hot electron |   | <p>The bolometer is a resistive element constructed from a material with a very small thermal capacity and large temperature coefficient so that the absorbed radiation produces a large change in resistance. The change in resistance is like to the photoconductor, however, the basic detection mechanisms are different. In the case of a bolometer, radiant power produces heat within the material, which in turn produces the resistance change. There is no direct photon-electron interaction.</p> <p>Most bolometers in use today are of the thermistor type made from oxides of manganese, cobalt, or nickel. Their construction is very rugged for system applications. Some extremely sensitive low-temperature semiconductor and superconductor bolometers are used in THz region.</p>  |
| Pyroelectric detector   |   | <p>The pyroelectric detector can be considered as a small capacitor with two conducting electrodes mounted perpendicularly to the direction of spontaneous polarization. During incident radiation, the change in polarization appears as a charge on the capacitor and a current is generated, the magnitude of which depends on the temperature rise and the pyroelectrical coefficient of the material. The signal, however, must be chopped or modulated. The detector sensitivity is limited either by amplifier noise or by loss-tangent noise. Response speed can be engineered making pyroelectric detectors useful for fast laser pulse detection, however with proportional decrease in sensitivity.</p>   |
| Golay cell  |  | <p>The Golay cell consists of a hermetically sealed container filled with gas (usually xenon for its low thermal conductivity) and arranged, so that expansion of the gas under heating by a photon signal distorts a flexible membrane on which a mirror is mounted. The movement of the mirror is used to deflect a beam of light shining on a photocell and so, producing a change in the photocell current as the output. In modern Golay cells, the photocell is replaced by a solid state photodiode and light emitting diode is used for illumination. The performance of the Golay cell is only limited by the temperature noise associated with the thermal exchange between the absorbing film and the detector gas, consequently the detector can be extremely sensitive with <math>D^* \approx 3 \times 10^9 \text{ cmHz}^{1/2} \text{ W}^{-1}</math>, and responsivities of <math>10^5</math> to <math>10^6 \text{ V/W}</math>. The response time is quite long, typically 15 msec.</p> |

room temperature, the typical value of heat capacity is about of  $2 \times 10^{-9} \text{ J/K}$  (for bolometer with dimensions  $50 \times 50 \times 0.5 \mu\text{m}$ ) and thermal conductance of  $10^{-7} \text{ W/K}$  (a-Si or  $\text{VO}_x$  bolometers). Both parameters define the time constant  $\tau_{th}$ , equal to about 20 ms. The upper NEP limit of thermal detector defines intrinsic temperature fluctuation noise [see Eq. (1)]. Then, the upper limit of NEP for a bolometer, limited only by radiation exchange with the environment, is  $NEP_R \approx 2.7 \times 10^{-13} \text{ W/Hz}^{1/2}$ . The upper limit value of  $NEP_R \approx 1.7 \times 10^{-19} \text{ W/Hz}^{1/2}$  can be achieved only at the expense of large  $\tau$  values ( $\tau \approx 3.5 \times 10^4 \text{ s}$ ) [23].

Whenever a pyroelectric crystal undergoes a change of temperature, surface charge is produced in a particular direction as a result of the change in its spontaneous polarization with temperature. The choice of pyroelectric materials is not an obvious one as it will depend on many factors including the size of the detector required, the operating temperature and the frequency of operation. An ideal material should have large pyroelectric coefficient, low dielectric constant, low dielectric loss and low volume specific heat. The possibility of satisfying these requirements

in a single material is not promising. While it is generally true that a large pyroelectric coefficient and a small dielectric constant are desirable, it is also true that these two parameters are not independently adjustable. Thus, we find that materials having a high pyroelectric coefficient also have a high dielectric constant, and materials having a low dielectric constant also have a low pyroelectric coefficient. This means that different detector-preamplifier sizes and configurations will be optimized with different materials [98,99].

## 7. Schottky barrier diodes

In spite of achievements of other kind of detectors for THz waveband (mainly SIS, HEBs, and TESs), the Schottky barrier diodes (SBDs) are among the basic elements in THz technologies. They are used either in direct detection and as nonlinear elements in heterodyne receiver mixers operating in temperature range of 4–300 K [1,5,23,24,48,58,100]. The cryogenically cooled SBDs were used in mixers preferably in the 1980-s and the early 1990-s and then they have been

replaced widely by SIS or HEB mixers [12], in which mixing processes are similar to that observed in SBDs, but, e.g., in SIS structures, the rectification process is based on quantum-mechanical photon-assisted tunnelling of quasiparticles (electrons).

Analysis of the state of the art in the development of SBDs and mixers for THz receivers is carried out, e.g., in Refs. 5, 58, and 100. The nonlinearity of SBD  $I$ - $V$  characteristic (the current increases exponentially with the applied voltage) is the prerequisite for mixing to occur. In the presence of a THz electric field, one can consider four groups of electron components: thermionic emission, tunnelling through the barrier, and generation-recombination inside or outside the depletion region marked as 1, 2, 3, and 4 in Fig. 28. In THz mixer diodes, the last two components can be neglected, because there are almost no holes available for recombination. The electrons of group I (see energy distribution of electrons inside Fig. 26) move toward the barrier where they are reflected or tunnel. Only the current generated by the electrons of group II affects THz electric field [101]. When the voltage generated by the THz field is close to its maximum value, electrons are able to cross the barrier; when the voltage is at its minimum – the electrons cannot cross the barrier. The electrons of this group suffer from transit time effects. Within half a period of the THz field, they have to transverse the depletion layer in order to cross the barrier. Such effects as skin effect, charge inertia, dielectric relaxation, and plasma resonance, lead to degradation of the detector performance. At THz frequencies, the noise due to series resistance and hot electrons dominates over shot noise. However, cooling of the diode lowers this noise.

Historically, first Schottky-barrier structures were pointed contacts of tapered metal wires (e.g., a tungsten needle) with a semiconductor surface (the so-called crystal detectors). Widely used were, e.g., contacts p-Si/W. At the operation temperature  $T = 300$  K, they have  $NEP \approx 4 \times 10^{-10}$  W/Hz<sup>1/2</sup>. Also pointed tungsten or beryllium bronze contacts to n-Ge, n-GaAs, n-InSb were used (see, e.g., Refs.

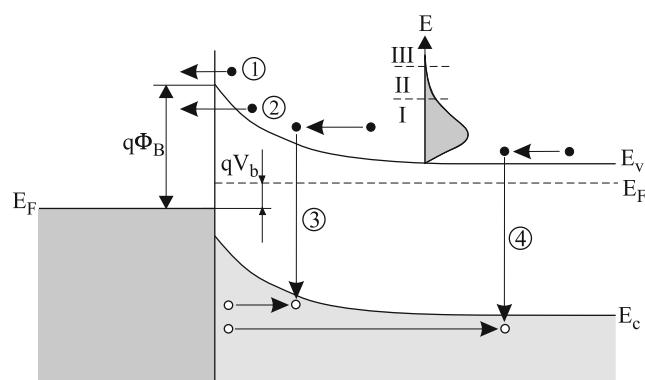
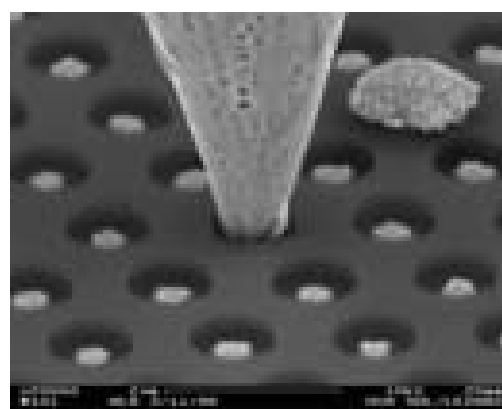


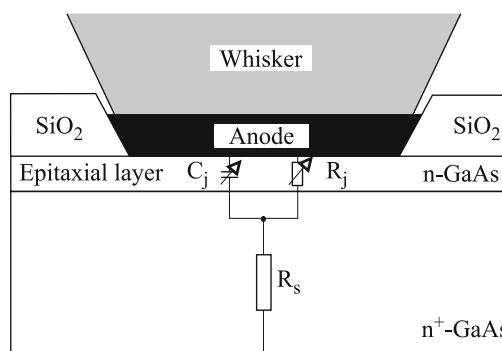
Fig. 28. Four basic transport processes in forward-biased Schottky barrier on an n-type semiconductor: 1 – thermionic emission, 2 – tunnelling current, and generation-recombination current inside (3) and outside (4) the depletion region.

102 and 103). In the mid 1960s, Young and Irvin developed the first lithographically defined GaAs Schottky diodes for high frequency applications [104]. Their basic diode structure was next replicated by a variety of groups. The basic whiskered diode structure, depicted in Fig. 29(a), greatly improved the quality of the diode due to inherently low capacity of the wicker contact. The pointed metal wire has a tip diameter of about 0.5  $\mu$ m and contacts a single anode in the array. The metal anodes are about 0.2  $\mu$ m where they contact the GaAs surface which is located below the silicon dioxide passivation layer. A tipped metal whisker provides the electrical contact to the anode and serves as a long wire antenna to couple in an external radiation.

The SBD structure shown in Fig. 29(a) is similar to the so-called “honeycomb” diode chip design, first produced by Young and Irvin in 1965 [104,107]. This design has been the most important steps toward a practical Schottky diode mixer for THz frequency applications, with several thousand diodes on a single chip and where parasitic losses such as the series resistance and the shunt capacitance are minimized. On highly doped GaAs substrate ( $\approx 5 \times 10^{18}$  cm<sup>-3</sup>) with an ohmic contact on the back side, a thin GaAs epitaxial layer, with a thickness of 300 nm to 1  $\mu$ m, is grown on the top of the substrate. Holes filled with a metal (Pt) in the SiO<sub>2</sub> insulating layer on top of the epitaxial layer define the anode area (0.25–1  $\mu$ m) [108]. In order to couple the signal



(a)



(b)

Fig. 29. GaAs Schottky barrier whisker contacted diode: (a) SEM image of a contacted chip used up to 5 THz (after Ref. 105) and (b) cross-section with equivalent circuit of the junction (after Ref. 106).



and the LO radiation to the mixer, a long-wire antenna in a 90° corner-cube reflector is used [109,110]. The required LO power ranges from 1 to 10 mW.

Cross-section of whisker SBD with the equivalent circuit of the junction is shown in Fig. 29(b). In heterodyne operation, mixing occurs in the nonlinear junction resistance  $R_j$ . The diode series resistance  $R_s$ , and the voltage-dependent junction capacitance  $C_j$  are parasitic elements which degrade the performance.

Due to limitation of whisker technology, such as constraints on design and repeatability, starting in the 1980s, the efforts were made to produce planar Schottky diodes. Nowadays, the whisker diodes are almost completely replaced by planar diodes. In the case of the discrete diode chip, the diodes are flip-chip mounted into the circuit with either solder or conductive epoxy. Using advanced technology elaborated recently, the diodes are integrated with many passive circuit elements (impedance matching, filters and waveguide probes) onto the same substrate [105]. By improving the mechanical arrangement and reducing loss, the planar technology is pushed well beyond 300 GHz up to several THz. For example, Fig. 30 shows photographs of a bridged Schottky diode and a four-Schottky diodes• chip arrayed in a balanced configuration to increase power handling. The air-bridged fingers replace the now obsolete whisker contact.

Schottky diode mixers in a waveguide configuration have an improved coupling efficiency compared to the open structure mount. To overcome a large shunt capacitance caused by the coplanar contact pads, a surface channel

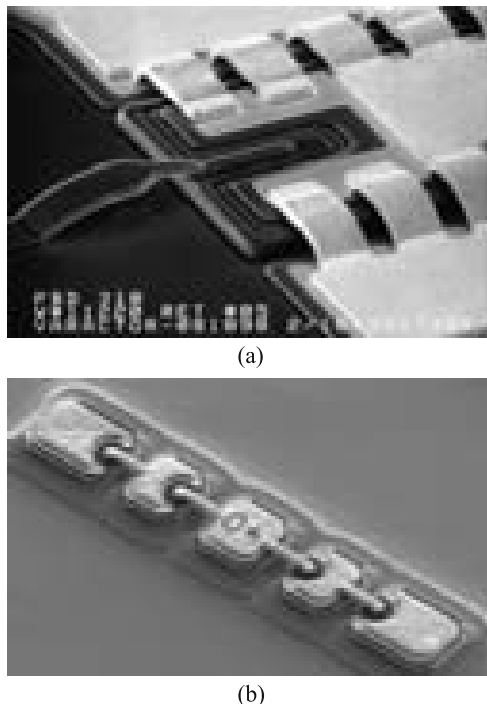


Fig. 30. Photographs of a bridged Schottky diode (a) (after Ref. 111) and a four-Schottky diodes• chip arrayed in a balanced configuration to increase power handling (b) (after Ref. 105).

diode, shown in Fig. 31(a), was proposed [112]. The planar diode soldered onto a microstrip circuit (e.g., a thin quartz substrate) is mounted into a waveguide mixer block. The required LO power is about 1 mW. For mixers operating at  $\approx 600$  GHz, double-sideband (DSB) noise temperature is about 1000 K. To eliminate losses, caused by support (influence of surface modes), fabrication of Schottky diodes on thin membrane was developed [113]. In this approach, the diodes are integrated with the matching circuit and most of the GaAs substrate is removed from the chip and the entire circuit is fabricated on the remaining GaAs membrane. Figure 31(b) shows an example of this type of SBD with 3- $\mu\text{m}$  thick membrane in a  $600 \times 1400 \mu\text{m}^2$  GaAs frame.

The current-voltage characteristic of Schottky barrier junction for the bias voltage values  $V > 3kT/q$ , can be approximated by

$$J_{MSI} = J_{st} \exp \frac{V}{V_o}, \quad (18)$$

where the device slop parameter  $V_o = kT/q$ . Differentiating Eq. (18) we can obtain the junction resistance

$$R_j = \frac{V_o}{I_{MSI}}. \quad (19)$$

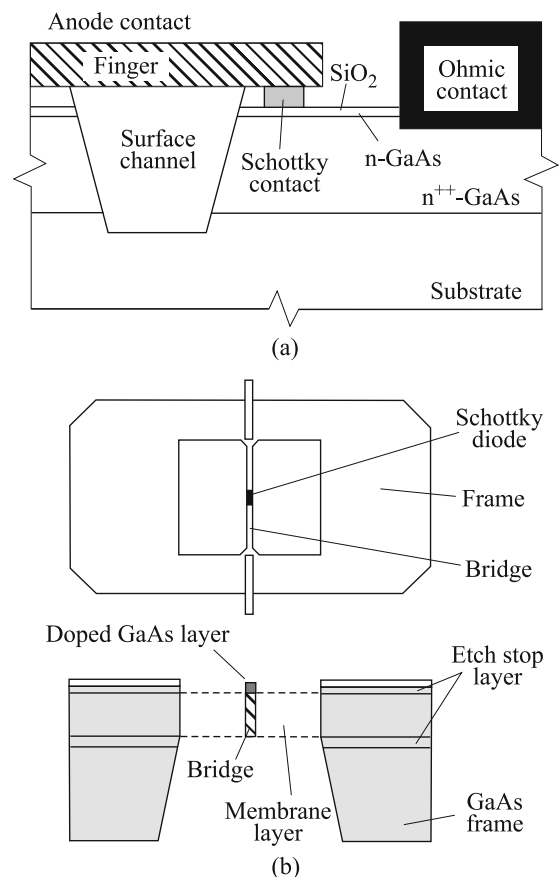


Fig. 31. Designs of planar Schottky diodes: (a) a surface channel design for frequencies below 1 THz (after Ref. 110), and (b) a GaAs Schottky diode on a membrane (after Ref. 113).

The parasitic parameters  $R_s$  and  $C_j$  define diode critical frequency called also cut-off frequency

$$\nu_C = (2 R_s C_j)^{-1}, \quad (20)$$

which should be notably higher compared to operation frequency.

The junction space-charge capacitance can be approximated by [114]

$$C_j(V) = \frac{\varepsilon A}{w} + 3 \frac{\varepsilon A}{d}. \quad (21)$$

Here  $\varepsilon$  is the semiconductor permittivity,  $A$  and  $d$  are the anode area and the diameter, respectively, and  $w$  is the depletion region thickness dependent on the carrier density, diffusion potential and bias. The second term is the peripheral capacitance. The junction capacitance is voltage dependent as depletion region depends on the bias applied. The specific capacity as a rule is not less than  $C \approx 10^{-7}$  F/cm<sup>2</sup>.

To achieve good performance at high frequencies, the diode area should be small. Reducing junction area one reduces junction capacities to increase operating frequency. But at the same time one increases the series resistance. The state-of-the-art devices have anode diameters about 0.25  $\mu\text{m}$  and capacitances 0.25 fF. For high-frequency operation, the GaAs layers are doped up to  $n \approx (5-10) \times 10^{17}$  cm<sup>-3</sup> [5,106,115].

In the lower frequency range ( $\nu < \approx 0.1$  THz), the operation of Schottky barrier diodes is well understood and could be described by mixer theories taking into account Schottky diode stray parameters (variable-capacitance and series resistance). In the THz range, however, the design and performance of the devices becomes increasingly complex. At higher frequencies there appear several parasitic mechanisms credit with not only, e.g., skin effect, but also with high-frequency processes in semiconductor material such as carrier scattering, carrier transit time through the barrier, dielectric relaxation, etc., which become important.

Figure 32 presents frequency dependent voltage sensitivity characteristic of SBDs at room temperature. VDI offers zero biased detectors with full waveguide band operation, high sensitivity, and high responsivity for a variety of THz applications [see Fig. 32(a)]. Planar construction yields a mechanically robust design. Figure 32(b) compares experimental data with theoretical prediction for diodes with different anode shapes. The solid line shows the theoretical dependence with allowance for the skin effect, the carrier inertia, the plasma resonance in the epitaxial layer  $f_{pe}$  and in the substrate  $f_{ps}$ , the phonon absorption ( $f_t$  and  $f_l$  are the frequencies of the transverse and longitudinal polar optical phonons), and the transit effects. The dashed line shows the same without allowance for the transit effect. The experimental results are related to SBDs with different anode shapes. A satisfactory agreement between the experiment and the calculation takes place on the whole range of frequency. Owing to the further improvement in the antenna, the detector sensitivity presented in the figure was increased by one order of magnitude – to approximately 350 V/W

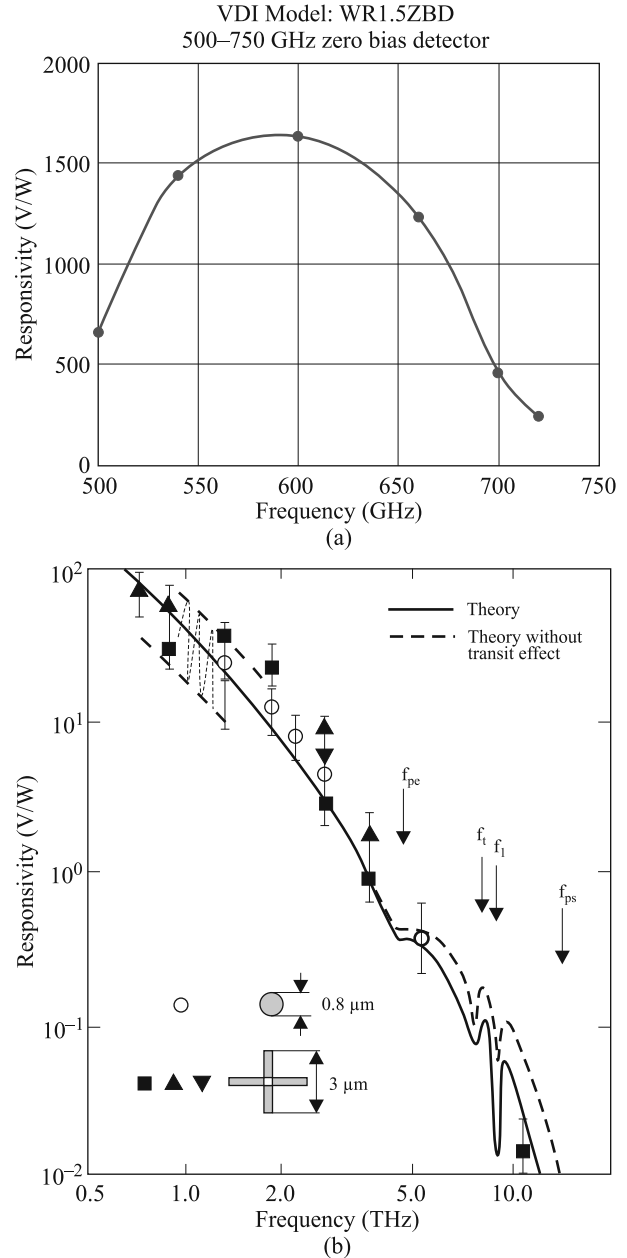


Fig. 32. Dependence of SBD voltage sensitivity on radiation frequency dependence for diodes: (a) produced by VDI, Virginia Diode, Inc. (after Ref. 116) and (b) with different anode shapes – experimental data are compared with theory (after Ref. 100).

near 1 THz. In the direct detection, SBDs reach  $NEP \approx 3 \times 10^{-10} - 10^{-8}$  W/Hz<sup>1/2</sup> at  $\nu = 891$  GHz [100].

The typical Schottky diodes usually have high low-frequency noise levels due to introduction of oxides, contaminants, and damage to the junction in the fabrication process. More recently, an alternative method of Schottky barrier formation has been elaborated by molecular beam epitaxy (MBE) *in-situ* deposition of a semimetal on semiconductor to reduce the imperfections that give rise to excess low-frequency noise, particularly  $1/f$  noise. The semimetal used is an ErAs film grown on Si-doped  $(\text{In}_{0.53}\text{Ga}_{0.47}\text{As})_{1-x}(\text{In}_{0.52}\text{Al}_{0.48}\text{As})_x$  on InP substrates – see Fig. 33 [117,118].

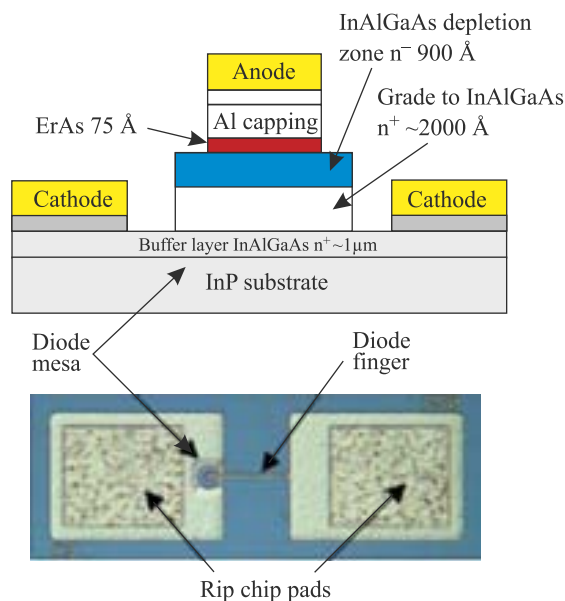


Fig. 33. Epitaxial layer structure of the ErAs detector scaled to micron size in a planar flip chip structure (after Ref. 117).

ErAs is a semimetal with the rock salt crystal structure and a lattice constant of 5.74 Å. This is close enough to both GaAs (5.65 Å) and InP (5.87 Å) so that, high-quality epitaxial films (up to 75 Å) of ErAs can be grown by MBE on either substrate, or on  $\text{In}_x\text{Al}_{1-x-y}\text{Ga}_y\text{As}$  films lattice matched to InP. The performance of the ErAs detector can be varied by controlling the Al percentage in the InAlGaAs Schottky layer. This results in the modification of the Schottky barrier height from approximately  $-0.05\text{eV}$  to  $0.45\text{eV}$  in a highly controlled manner. The noise equivalent power (NEP) for these detectors at 639 GHz reach  $4 \times 10^{-12} \text{ W/Hz}^{1/2}$ , what is about two orders of magnitude better than for typical GaAs Schottky diodes (see Fig. 34). A goal of terahertz imaging focal-plane technology (TIFT) programme provided by DARPA is improvement in NEP value to about  $10^{-12} \text{ W/Hz}^{1/2}$  [119].

The heterodyne SBD receivers are worse compared to cooled HEB receivers and SIS mixers (see Fig. 15). At the

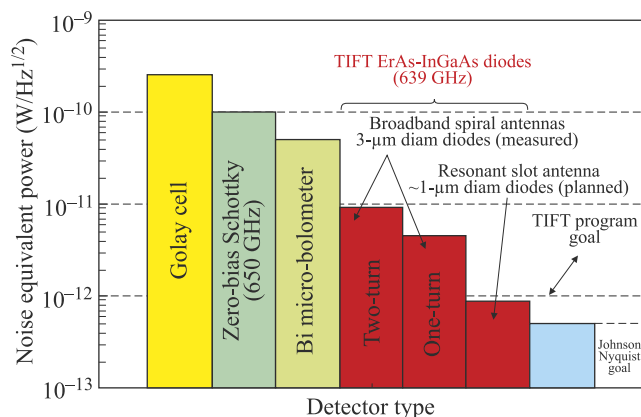


Fig. 34. Comparison of NEP values of several room-temperature THz detectors (after Ref. 119).

same time, SBD receivers operation without cooling gives opportunities for using SBD mixers in different mm and sub-mm applications. Their sensitivity is quite suitable to be used in mm wave spectrometers with moderate resolution [120,121]. Superconducting mixers typically require microwatt LO powers, which is roughly 3–4 orders of magnitude lower than their SBD predecessors. As a result, a broader range of LO sources can be used. The technologies being used or investigated include diode multipliers, lasers and optoelectronics, and “vacuum tube” oscillators such as klystrons, including novel nano-fabricated versions.

## 8. Extrinsic detectors

Historically, an extrinsic photoconductor detector based on germanium was the first extrinsic photodetector. After it, photodetectors based on silicon and other semiconductor materials, such as GaAs or GaP, have appeared [86].

Extrinsic photodetectors are used in a wide range of the IR spectrum extending from a few  $\mu\text{m}$  to approximately 300  $\mu\text{m}$ . They are the principal detectors operating in the range  $\lambda > 20 \mu\text{m}$ . The spectral range of particular photodetectors is determined by the doping impurity and by the material into which it is introduced. For the shallowest impurities in GaAs, the long wavelength cutoff of photoresponse is around 300  $\mu\text{m}$ . Detectors, based on silicon and germanium, have found the widest application as compared with extrinsic photodetectors on other materials.

Research and development of extrinsic IR photodetectors have been ongoing for more than 50 years [122,123]. In the 1950s and 1960s, germanium could be made purer than silicon; doped Si then needed more compensation than doped Ge and was characterized by shorter carrier lifetimes than extrinsic germanium. Today, the problems with producing pure Si have been largely solved, with the exception of boron contamination [124]. Si has several advantages over Ge; for example, three orders of magnitude higher impurity solubilities are attainable, hence thinner detectors with better spatial resolution can be fabricated from silicon. Si has lower dielectric constant than Ge, and the related device technology of Si has now been more thoroughly developed, including contacting methods, surface passivation and mature MOS and CCD technologies. Moreover, Si detectors are characterized by superior hardness in nuclear radiation environments.

### 8.1. Extrinsic germanium photoconductors

Silicon detectors have largely supplanted germanium extrinsic detectors for both high and low background applications where comparable spectral response can be obtained. However, for wavelengths longer than 40  $\mu\text{m}$  there are no appropriate shallow dopants for silicon; therefore germanium devices are still of interest for very long wavelengths. Germanium photoconductors have been used in a variety of infrared astronomical experiments, both airborne and space-based. As an example of the space application is

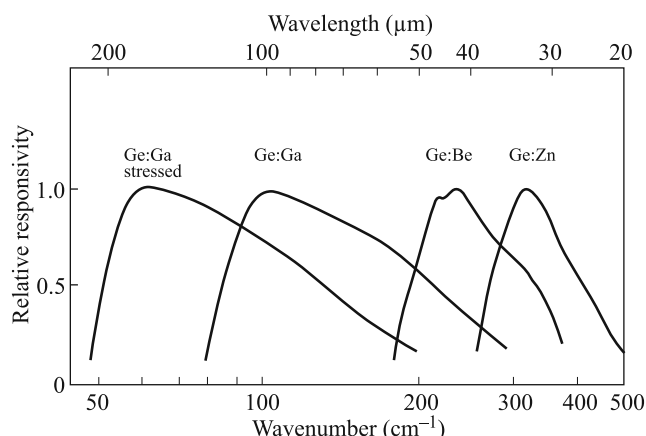


Fig. 35. Relative spectral response of some germanium extrinsic photoconductors (after Ref. 127).

ISOPHOT, the photometer for ESA's infrared space observatory (ISO), which uses extrinsic photoconductors at the wavelength ranging from 3 to more than 200  $\mu\text{m}$  [125]. The highly successful IRAS mission marks the beginning of modern, far infrared photoconductor research and development [126]. Very shallow donors, such as Sb, and acceptors, such as B, In or Ga, provide cut-off wavelengths in the region of 100  $\mu\text{m}$ . Figure 35 shows the spectral response of the extrinsic germanium photoconductors doped with Zn, Be, Ga and of stressed gallium doped germanium [127]. Despite a large amount of effort, recently in the development of very sensitive thermal detectors, germanium photoconductors remain the most sensitive detectors for wavelength shorter than 240  $\mu\text{m}$ .

The achievement of low  $NEP$  values in the range of a few parts  $10^{-17} \text{ WHz}^{-1/2}$  (see Table 6, Ref. 128) was made possible by advances in crystal growth development and control the residual minority impurities down to  $10^{10} \text{ cm}^{-3}$  in a doped crystal [129,130]. As a result, a high lifetime and mobility value and thus a higher photoconductive gain have been obtained.

Ge:Be photoconductors cover the spectral range from  $\approx 30$  to 50  $\mu\text{m}$ . Beryllium, a double acceptor in Ge with energy levels at  $E_v + 24.5 \text{ meV}$  and  $E_v + 58 \text{ meV}$ , poses special doping problems because of its strong oxygen affinity.

Be doping concentrations of  $5 \times 10^{14} \text{ cm}^{-3}$  to  $1 \times 10^{15} \text{ cm}^{-3}$  give significant photon absorption in 0.5–1 mm thick detectors, while at the same time keeping dark currents caused by hopping conduction at levels as low as a few tens of electrons per second. Ge:Be detectors with responsivities  $> 10 \text{ A/W}$  at  $\lambda = 42 \mu\text{m}$  and quantum efficiency 46% have been reported at low background [129].

Ge:Ga photoconductors are the best low background photon detectors for the wavelength range from 40 to 120  $\mu\text{m}$ . Since the absorption coefficient for a material is given by the product of the photoionization cross-section and the doping concentration, it is generally desirable to maximize this concentration. The practical limit occurs when the concentration is so high that impurity band conduction results in excessive dark current. For Ge:Ga, the onset of impurity banding occurs at approximately  $2 \times 10^{14} \text{ cm}^{-3}$ , resulting in an absorption coefficient of only  $2 \text{ cm}^{-1}$  and typical values of quantum efficiency range from 10% to 20% [131]. Consequently, the detectors must either have long physical absorption path lengths or be mounted in an integrating cavity.

However, there are a number of problems with the use of germanium. For example, to control dark current the material must be lightly doped and therefore absorption lengths become long (typically 3–5 mm). Because the diffusion lengths are also large (typically 250–300  $\mu\text{m}$ ), pixel dimensions of 500–700  $\mu\text{m}$  are required to minimize crosstalk. In space applications, large pixels imply higher hit rates for cosmic radiation. This in turn implies very low readout noise for arrays operated in low background limit, what is difficult to achieve for large pixels with large capacitance and large noise. A solution is using the shortest possible exposure time. Due to small energy band gap, the germanium detectors must operated well below the silicon "freeze-out" range – typically at liquid helium temperature.

Application of uniaxial stress along the [100] axis of Ge:Ga crystals reduces the Ga acceptor binding energy, extending the cutoff wavelength to  $\approx 240 \mu\text{m}$  [132,133]. At the same time, the operating temperature must be reduced to less than 2 K. In making practical use of this effect, it is essential to apply and maintain very uniform and controlled pressure to the detector so that the entire detector volume is

Table 6. Status summary of Ge IR detectors for low-background applications (after Ref. 128).

| Detector                            | $(\Delta E)_{opt}$<br>(meV) | $\lambda_p$<br>( $\mu\text{m}$ ) | $\lambda_c$ (T)<br>$\mu\text{m}$ (K) | $\eta(\lambda_p)$<br>(%) | $B$<br>( $\text{phcm}^{-2}\text{s}^{-1}$ ) | $NEP(\lambda; T; f)$<br>( $\text{WHz}^{-1/2}$ ) | $\lambda$ ( $\mu\text{m}$ );<br>$T$ (K); $f$ (Hz) |
|-------------------------------------|-----------------------------|----------------------------------|--------------------------------------|--------------------------|--|---|---|
| Ge:Li                               | 9.98                        | 125 (calc)                       |                                      |                          | $8 \times 10^8$                            | $1.2 \times 10^{-16}$                           | (120;2;13)  |
| Ge:Cu                               | 43.21                       | 23                               | 29.5 (4.2)                           | 50                       | $5 \times 10^{10}$                         | $1.0 \times 10^{-15}$                           | (12;4.2;1)  |
| Ge:Be <sup>a</sup>                  | 24.81                       | 39                               | 50.5 (4.2)                           | 100 <sup>b</sup>         | $1.9 \times 10^{10}$                       | $1.8 \times 10^{-16}$                           | (43;3.8;20)                                       |
| Ge:Ga                               | 11.32                       | 94                               | 114 (3)                              | 34                       | $6.1 \times 10^9$                          | $5.0 \times 10^{-17}$                           | (94;3;150)  |
| Ge:Ga <sup>a</sup>                  | 11.32                       | 94                               | 114 (3)                              | $\sim 100^b$             | $5.1 \times 10^9$                          | $2.4 \times 10^{-17}$                           | (94;3;150)  |
| Ge:Ga <sup>a</sup> (s) <sup>b</sup> | $\sim 6$                    | 150                              | 193 (2)                              | 73 <sup>b</sup>          | $2.2 \times 10^{10}$                       | $5.7 \times 10^{-17}$                           | (150;2;150)                                       |

<sup>a</sup>Results obtained with an integrating cavity.

<sup>b</sup>(s): stress =  $6.6 \times 10^3 \text{ kgcm}^{-2}$ .



placed under stress without exceeding its breaking strength at any point. A number of mechanical stress modules have been developed. The stressed Ge:Ga photoconductor systems have found a wide range of astronomical and astrophysical applications [134–139].

The standard planar hybrid architecture, commonly used to construct near and mid-infrared focal-plane arrays [86], is not suitable for far IR detectors where readout glow, lack of efficient heat dissipation, and thermal mismatch between the detector and the readout could potentially limit their performance. Usually, the THz arrays have a modular design with many modules stacked together to form a 2-dimensional array.

The Infrared Astronomical Satellite (IRAS), the Infrared Space Observatory (ISO), and for the far-infrared channels the Spitzer-Space Telescope (Spitzer) have all used bulk germanium photoconductors. In Spitzer mission, a  $32 \times 32$ -pixel Ge:Ga unstressed array was used for the  $70\text{-}\mu\text{m}$  band, while the  $160\text{-}\mu\text{m}$  band had a  $2 \times 20$  array of stressed detectors. The detectors are configured in, the so-called, Z-plane to indicate that the array has substantial size in the third dimension. The poor absorption of the Ge:Ga detector material requires that the detectors in this array are huge – 2 mm long. Due to the long absorption path in germanium, the detectors are illuminated edge-wise with transverse contacts, and the readouts are hidden behind them, what is shown in Fig. 36.

An innovative integral field spectrometer, called the field imaging far-infrared line spectrometer (FIFI-LS) that produces a  $5 \times 5$  pixel image with 16 spectral resolution elements per pixel in each two bands was constructed at the Max Planck Institut für Extraterrestrische Physik under the direction of Albrecht Poglitsch. This array, shown in Fig. 37, was developed for the Herschel Space Observatory and SOFIA [138,139]. To accomplish this, the instrument has two  $16 \times 25$  Ge:Ga arrays, unstressed for the  $45\text{--}110\text{-}\mu\text{m}$  range and stressed for the  $110\text{--}210\text{-}\mu\text{m}$  range. The low-stressed blue detectors have a mechanical stress on the pixels which is reduced to about 10% of the level needed for the long-wavelength response of the red detectors. Each

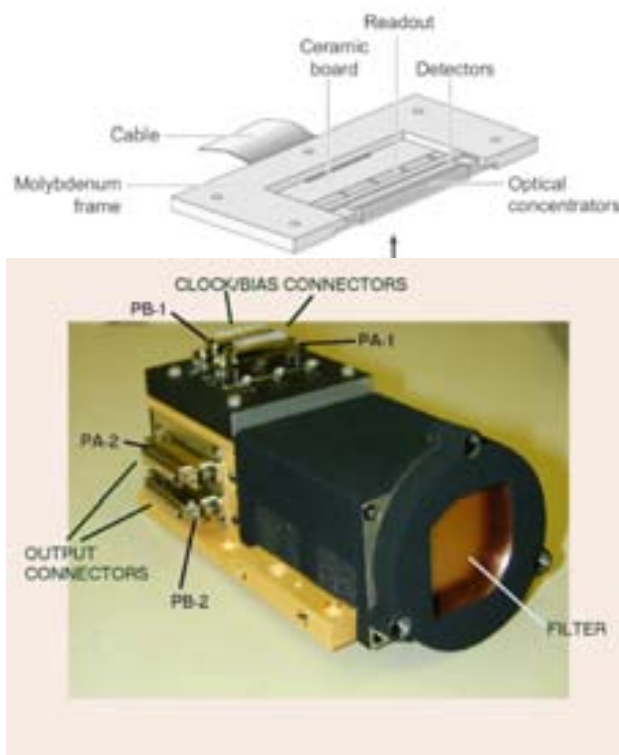


Fig. 36. The Spitzer Space Telescope  $70\text{-}\mu\text{m}$  array design of a  $4 \times 32$  module of the edge-illuminated detectors. Eight such modules are stacked to create the full  $32 \times 32$  array, which covers the wavelength range  $50\text{--}110\text{-}\mu\text{m}$  (after Ref. 138).

detector pixel is stressed in its own subassembly, and a signal wire is routed to preamplifiers housed nearby what obviously limits this type of array to much smaller formats than they are available without this constraints.

The photodetector array camera and spectrometer (PACS) is one of the three science instruments on ESA's far infrared and sub-millimetre observatory – Herschel Space Laboratory. Apart from two Ge:Ga photoconductor arrays (stressed and unstressed) with  $16 \times 25$  pixels, each, it employs two filled silicon bolometer arrays with  $16 \times 32$  and  $32 \times 64$  pixels, respectively, to perform integral-field spec-

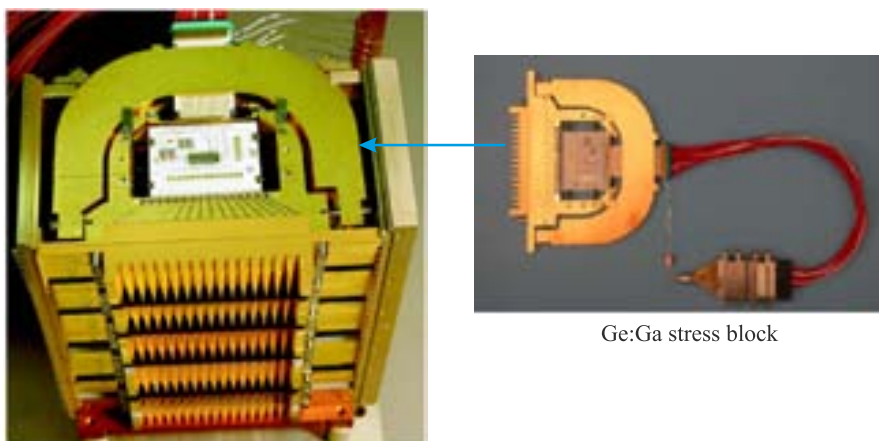


Fig. 37. PACS photoconductor focal plane array. The 25 stressed and low-stress modules of PACS instrument (corresponding to 25 spatial pixels) in the red and blue arrays are integrated into their housing (after Ref. 140).

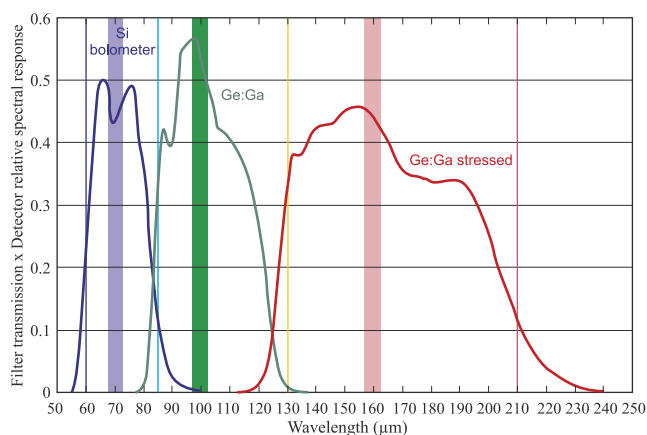


Fig. 38. Effective spectral response of the filter/detector chain of the PACS photometer in its three bands (after Ref. 141).

troscopy and imaging photometry in the 60–210  $\mu\text{m}$  wavelength regime. Figure 38 shows the spectral response of the filter/detector chain of the PACS photometer in its three bands. Median  $NEP$  values are  $8.9 \times 10^{-18} \text{ W/Hz}^{1/2}$  for the stressed and  $2.1 \times 10^{-17} \text{ W/Hz}^{1/2}$  for the unstressed detectors, respectively. The detectors are operated at  $\sim 1.65 \text{ K}$ . The readout electronics is integrated into the detector modules – each linear module of 16 detectors is read out by a cryogenic amplifier/multiplexer circuit in CMOS technology but operates at temperature 3–5K.

Far-infrared photoconductor arrays suffer from the standard bulk photoconductor photometric issues. Especially germanium detectors have complicated responses that affect calibration, observing strategies and data analysis in low background applications. The devices operate at very low bias voltages and even small changes in the operating points of amplifiers can result in unacceptable bias changes on the detectors. More details can be found in Ref. 142.

As is mentioned above, the standard hybrid focal plane array (FPA) architecture is not generally suitable for far-IR arrays (although also this architecture is used, Ref. 143) primarily because glow from the readout is sensed by the detector, degrading its performance. In response, a new layered-hybrid structure was introduced to alleviate these problems and make possible the construction of large format far-IR FPAs (see Fig. 39) [144,145]. In this design, an intermediate substrate is placed between the detector and the readout, which is pixelized on both sides in a format identical to that of the array and the electrical contact between corresponding pixel pads are made through embedded vias. The substrate material must be chosen to have sufficient IR-blocking property, high thermal conductivity, and an expansion coefficient that is between that of germanium and silicon. Alumina ( $\text{Al}_2\text{O}_3$ ) and aluminium nitride ( $\text{AlN}$ ) have these properties and are possible choices as substrate materials. Blocking of the readout glow from reaching the detector, provide more efficient heat dissipation, improve temperature uniformity across the array, and mitigate the thermal mismatch between the detector and the readout. In addition,

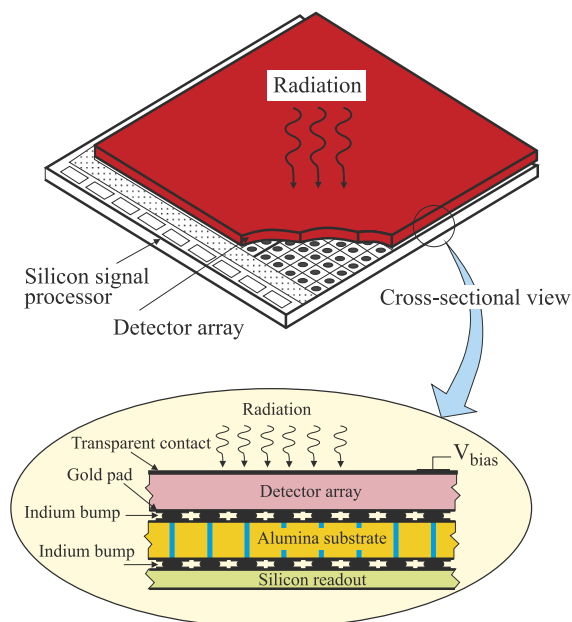


Fig. 39. The layered-hybrid design suitable for large format far IR and sub-mm arrays.

tion, the substrate serves as a fanout board providing a simple and robust way to connect the FPA to the external electronics with no additional packaging requirement. Figure 40 shows an assembled Ge:Sb FPA ( $\lambda_c \approx 130 \mu\text{m}$ ) using the layered-hybrid architecture. For low bias voltage photoconductor operated at low temperatures, a capacitive transimpedance amplifier (CTIA) design offers an effective readout solution. It is predicted that using this structure, very large format FPAs with sensitivities better than  $10^{-18} \text{ W/Hz}^{1/2}$  could be realized, fulfilling the technology goals of the upcoming astronomical instruments.

## 8.2. Another extrinsic detectors

Nowadays, the promise of a new generation of large format far-IR detector arrays seems to be attainable using another material system. Silicon-based BIB detectors doped with



Fig. 40. The fully assembled layered-hybrid Ge:Sb FPA ( $\lambda_c \approx 130 \mu\text{m}$ ) with SB349 readout (CTIA readout). The readout side is shown; the detector is located on the other side of the fanout board (after Ref. 145).

arsenic and antimony have the materials of choice for astronomical detectors at the wavelengths from 5  $\mu\text{m}$  to 40  $\mu\text{m}$ . Conventionally designed and processed Si:As BIB detectors have a cut-off wavelength of about 28  $\mu\text{m}$ , but wavelength extension to approximately 50  $\mu\text{m}$  is possible [146]. Attempts have been also made to provide a similar direct detector technology for operation in the far-IR by switching from silicon to a semiconductor material that would provide a shallower impurity band [147]. Both Ge-based and GaAs-based BIB systems have been attempted, with greater success achieved in germanium [148]. However, the smaller binding energy of shallow donors in GaAs compared to Ge results in response at wavelengths exceeding 300  $\mu\text{m}$  without uniaxial stress.

Among THz low-temperature cooled detectors there exist many publications about the possibility of using  $\text{Pb}_{1-x}\text{Sn}_x\text{Te:In}$  ( $x \approx 0.25$ , In content is about 2 atomic %) photoconductors as THz detectors in the range of 1 THz [23,24,149–154]. Persistent photoresponse with current responsivity about  $10^3$  A/W at 40 mV bias and integration time  $\approx 1$  s at the wavelengths of 90  $\mu\text{m}$  and 116  $\mu\text{m}$  has been observed in  $\text{Pb}_{0.25}\text{Sn}_{0.75}\text{Te:In}$  photoconductors [149]. This value is larger by a factor of about 100 than the responsivity of the Ge:Ga photoconductor in the same conditions of the experiments ( $T \approx 4$  K, detectors protected from the background radiation). The photoresponse signals were observed at wavelengths up to 337  $\mu\text{m}$  [151]; it is one of the highest cut-off wavelengths observed so far for extrinsic semiconductor photodetectors.

Investigation of III-group doped impurity states in narrow-gap IV-VI alloys based on the lead telluride semiconductors has begun in the early 1970•s. The persistent photoconductivity effects observed in these materials are analogous to the features of III-V and II-VI semiconductors with the DX-centres [155]. It was shown that in the group of III-doped IV-VI semiconductors at low temperatures,  $T \ll T_c$ , photoconductivity relaxation consists of two compo-

nents: the “fast” one (varies between 1 ms and 1 s) and the slow one, which may exceed  $10^5$  s [156]. The  $T_c$  value is about 25 K for indium-doped and about 80 K for the Ga-doped materials.

The persistent photoconductivity induced by THz radiation in  $\text{Pb}_{1-x}\text{Sn}_x\text{Te:In}$  alloys at low temperatures is clearly connected with the existence of a barrier between the localized deep and free electron states, as it is observed in other semiconductors at shorter wavelengths. The evidence of such a barrier in IV-VI semiconductors with deep impurities is also become apparent by current instabilities like Gunn effect, but with much lower frequency of oscillations [157].

## 9. Pair braking photon detectors

One of the methods of photon detection consists in using superconductivity materials. If the temperature is far below the transition temperature  $T_c$ , most of electrons in them are banded into Cooper pairs. Photons with energies exceeding the binding Cooper pair energies in superconductor  $2\Delta$  (each electron must be supplied with the energy  $\Delta$ ), can break these pairs producing quasiparticles (electrons) [see inside of Fig. 41(a)]. This process resembles the interband absorption in semiconductors, with the energy gap equal to  $2\Delta$ , when under the photons absorbed the electron-hole pares are created. One of the advantages of these detectors is that the fundamental noise due to the random generation and recombination of thermal quasiparticles decreases exponentially with temperature as  $\exp(-\Delta/k_B T)$  [158]. The best SSB noise temperature  $T_n$ , that can be gained is  $k_B T_n = h\nu/\eta$ . With  $\eta = 1$  the quantum limit can be achieved but it never can be overcome [159]. In pair breaking detectors, it is possible to get  $\eta = 1$  and thus one can approach nearly the quantum operation limit (see Fig. 15).

The superconductor tunnel junction (STJ) is used to let quasiparticles pass through the junction and to separate off the Copper pairs. First proposition of pair-breaking detector

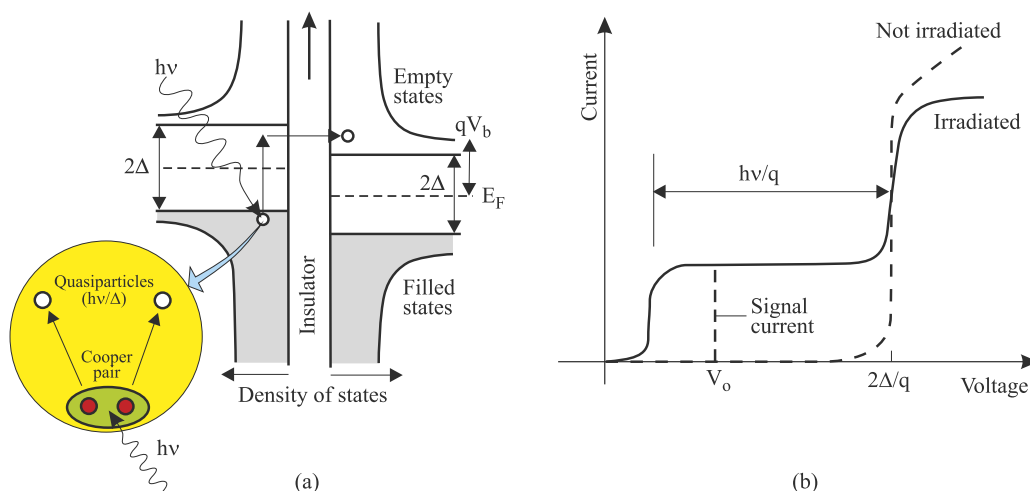


Fig. 41. SIS junction: (a) energy diagram with applied bias voltage and illustration of photon assisted tunnelling and (b) current-voltage characteristic of a non-irradiated and irradiated barrier. The intensity of the incident radiation is measured as an excess of the current at the certain bias voltage  $V_0$ . Schematic creation of quasiparticle is shown inside (a).



with STJ was made in the early 1960s [160]. Next, several structures of pair braking detectors which use different ways to separate quasiparticles from Cooper pairs have been proposed. Among them there are: superconductor-insulator-superconductor (SIS) and superconductor-insulator-normal metal (SIN) detectors and mixers, radio frequency (RF) kinetic inductance detectors, and superconducting quantum interference device (SQUID) kinetic inductance detectors. Superconducting detectors offer many benefits: outstanding sensitivity, lithographic fabrication, and large array sizes, especially through the development of multiplexing techniques. The basics physics of these devices and recent progress in their developments are described in Ref. 12. Here, we concentrate on the most important, SIS detectors.

The SIS detector is a sandwich of two superconductors separated by a thin ( $\approx 20$  Å) insulating, what is schematically shown in Fig. 42. Nb and NbTiN are almost exclusively used as superconductors for the electrodes. For a standard junction process, the base electrode is 200-nm sputtered Nb, the tunnel barrier is made using a thin 5-nm sputtered Al layer which is either thermally oxidized ( $\text{Al}_2\text{O}_3$ ) or plasma nitridized (AlN). The counterelectrode is 100-nm sputtered Nb or reactively sputtered NbTiN. Typical junction areas are about  $1 \mu\text{m}^2$ . The entire SIS structure is deposited in a single deposited run. The junction is defined by photolithography or electron-beam lithography and reactive ion etching of the counterelectrode. Finally, 200-nm thick thermally evaporated SiO or sputtered  $\text{SiO}_2$  are deposited. A  $\text{SiO}_x$  layer insulates the junction and serves as the dielectric for the wiring and RF tuning circuit on top of the junction.

The SIS operation is based on photoassisted tunnelling of quasi-particles through the insulating layer. Although the physics of this effect was demonstrated and theoretically explained already in the 1960s [161,162], it took almost two decades to make use of the effect in a mixer [163,164]. Nowadays, SIS tunnel junctions are mainly used as mixers in heterodyne type mm and sub-mm receivers because of their strong non-linear I-V characteristic. They can be also used as direct detection detectors [164,165]. Operating temperature of SIS junctions is below 1 K, typically  $T \approx 300$  mK.

The SIS operation can be described by using the energy band representation known for semiconductors. The states below the energy gap are considered to be occupied, and those above the gap are empty [Fig. 41(a)]. The curves indicate the electron density of states. When the bias voltage  $V_b$

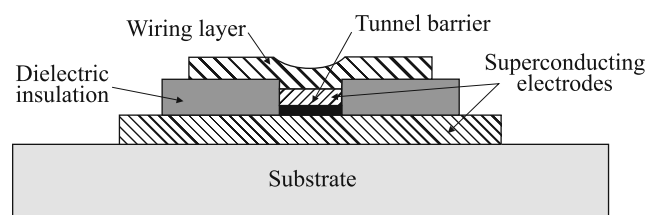


Fig. 42. A cross section of a typical SIS junction.

is applied to the junction, there is a relative energy shift of  $qV_b$  between the Fermi levels of the two superconductors. If  $qV_b$  is lower than the energy gap  $2\Delta$ , no current flows (electrons may only tunnel into unoccupied states at the same energy). However, if the junction is irradiated, photons of the energy  $h\nu$  may assist the tunnelling, which now may occur for  $qV_b > 2\Delta \dots h\nu$ .

The current-voltage characteristic of an SIS device is shown in Fig. 41(b). When the bias voltage reaches the gap voltage, a steep increase in the current occurs. At this particular voltage, the divergent densities of states of both superconductor layers cross, and Cooper pairs on one side of the insulating layer break up into two electrons (quasi-particles). Next, these quasi-particles tunnel from one side of the insulator to the other, where they recombine. A sharp onset of normal tunnelling current is arising beyond a DC threshold voltage equal to the superconductor energy gap  $2\Delta$ , and this abrupt nonlinearity in the single-particle tunnelling is used for mixing. The I-V nonlinearity is small; about few tenths of a millivolt, and might be compared with the nonlinearity of a Schottky diode (of the order of 1 mV). However, the SIS nonlinearity at the gap voltage is substantially less than the energy of THz photons and the classical mixer theory cannot be applied. To explain possibility of using SIS in THz detection, detailed description of mixing theory including quantum effects is necessary [165].

Although the IF bandwidth of and SIS junction itself is very large due to the inherently fast tunnelling process, it is limited in practical applications by the electric circuitry. A typical IF band is 4–8 GHz. One of the main challenges for high-frequency SIS mixer design is dealing with the large parallel-plate capacitance of the SIS junction. Although the area of an SIS junction is similar to the area of a Schottky diode, its parasitic capacitance is much higher (typically 50–100 fF compared to  $\approx 1$  fF), because the two superconducting electrodes form a parallel plate capacitor. As a consequence, on-chip tuning circuits are needed to compensate for the capacitance, and their proper design is a key issue for an SIS mixer [12,48]. At higher frequencies, especially over 1 THz ( $\lambda = 300 \mu\text{m}$ ), the losses in the tuning circuit become important and cause the mixer performance to deteriorate. Nevertheless, good performance has been obtained up to around 1.5–1.6 THz ( $\lambda = 200\text{--}188 \mu\text{m}$ ).

There are two major ways to accomplish proper design issues for SIS mixers: waveguide coupling and quasi-optical coupling [12]. Figure 43 shows the examples of both configurations. The more traditional approach is waveguide coupling, in which the radiation is first collected by a horn into a single-mode waveguide and then coupled onto a lithographed thin-film transmission line on the SIS chip itself. The chip shown in Fig. 43(a) is approximately 2-mm long and 0.24-mm wide and it is fabricated on 25- $\mu\text{m}$  thick silicon utilizing silicon-on-insulator bonded wafers. The 1- $\mu\text{m}$ -thick gold beam leads extend beyond the edges of substrate and they are an electrical contact to the metal waveguide probe [11]. Serious complication of waveguide



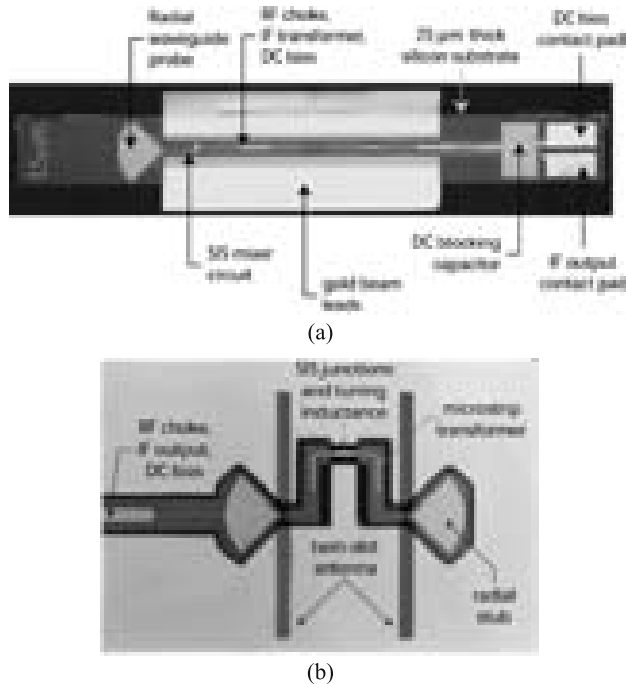


Fig. 43. Images of a waveguide SIS mixer operated in the 200–300 GHz band (a) and a quasi-optical SIS mixer (b) (after Ref. 12).

coupling is that the mixer chip must be very narrow, and must be fabricated on ultrathin substrate.

In the quasi-optical coupling, the intermediate step of radiation collection into a waveguide is omitted, and instead uses a lithographed antenna on the SIS chip itself. Such mixers are substantially simpler to fabricate and may be produced using thick substrates. In the design structure shown in Fig. 43(b), the radial stubs serve as RF short circuits and couple the radiation received by the slots into an Nb/SiO/Nb superconducting microstrip. This chip uses two Nb/Al<sub>2</sub>O<sub>3</sub>/Nb SIS junctions and the short strip section in between the junctions provides the tuning inductance needed to compensate the junction capacitance.

SIS mixers are among the most sensitive and low intrinsic noise structures at  $\nu \approx 0.3$ – $0.7$  THz. Nb-based SIS mixers with Nb wiring yield almost quantum limited, i.e., the noise temperature is below  $3\hbar\nu/kT$  (see Fig. 15) [165,166]. At larger frequencies,  $\nu \approx 1.0$ – $1.3$  THz, SISs intrinsic noise quickly increases due to high-frequency losses. Further gain in sensitivity is possible using multielement or matrix arrays. However, up to now, SIS detectors are difficult to integrate into large arrays. There is only a success in creation of small number element arrays because of appreciable difficulties in their creation [167]. SIS mixers seem to be the best solution for the ground-based radio-astronomy at mm and sub-mm wavelengths region in the frequency range  $\nu < 1$  THz [168].

The signal bandwidth of an SIS mixer is 10–30% of its centre frequency with the large fractional bandwidth at low frequency band. Up to 1 THz, the mixers are in a waveguide mount, while the 1.2–1.25 THz mixers employ a quasi-optical coupling.

Single pixel SIS mixers typically require approximately 40–100  $\mu$ W of LO pump power, which is appreciably lower compared to LO pump power for single pixel SBD mixers ( $P > 1$  mW) [169]. Much lower LO powers require superconductor hot electron bolometer mixers ( $< 100$  nW– $1$   $\mu$ W) [170] though they also operate at very low temperature. Unlike Schottky diodes or SIS detectors, the hot electron bolometers are thermal detectors.

The presence of the capacity in SIS structures is a reason of current shorting in them because of Josephson's effect. To exclude this effect, the superconductor-insulator-normal metal (SIN) structure was proposed to change one of the superconductors by normal metal contact [171]. Though, in SIN structures,  $I$ - $V$  characteristics are not such nonlinear as in SIS structures which is a reason of sensitivity decrease, but the influence of Josephson's effect is excluded. To force the electron tunnelling from the normal metal into the superconductor, the energy of electrons above the Fermi level should be not less than  $\Delta \dots qV_b$ , where  $V_b$  is the junction bias voltage [12]. Thus, the junction current probes the tail of the Fermi distribution of electrons in the normal metal and is exponentially sensitive to the electron temperature  $T_e$ , as  $\exp[-(\Delta \dots qV_b)/kT_e]$ . Thus, SIN junction is a thermometer for measuring the electron temperature in a normal metal.

Figure 44 shows schematic configuration of SIN radiation coupling and temperature readout [172,173]. A thin strip of metal (black strip) with micron dimensions serves as a resistive load to thermalize the RF currents from the superconducting antenna. The resulting temperature rise of the

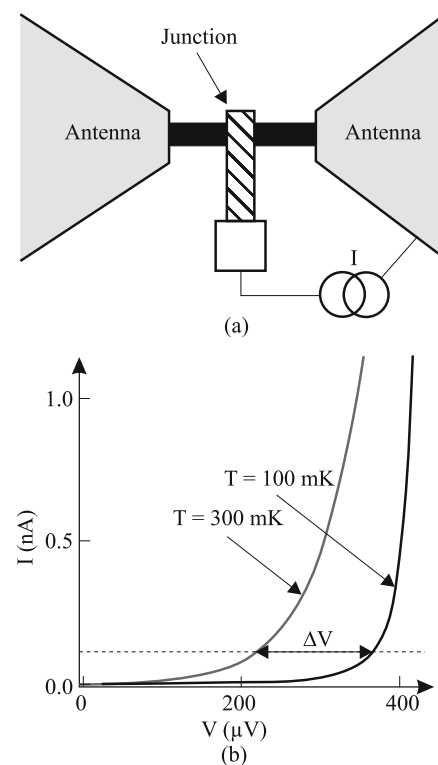


Fig. 44. SIN detector: (a) schematic configuration of radiation coupling and temperature readout (after Ref. 170) and (b) principle of operation (after Ref. 174).

electrons in the strip is measured as a change in the voltage across the junction which is biased at the constant current  $I$ . Variations of the electron temperature in the absorber strip are detected from smearing of  $I$ - $V$  curves of the SIN junction [see Fig. 44(b)]. The contact to the superconducting electrode is made of a superconductor whose  $T_c$  is much higher than that of the electrode. As a normal metal absorber, 300-Å thick Cu layer can be used [172]. In order to avoid energy losses through diffusion of the electrons into the antenna, the absorber layer is contacted via superconducting electrodes (e.g., Al), since the Andreev effect prohibits energy transport from the normal metal to the superconductor at an NS-interface [175].

The principles of SIN structures operation are discussed in Ref. 176.  $NEP$  of these detectors can achieve a value close to  $10^{-17}$  W/Hz at  $T \approx 300$  mK. Schmidt *et al.* have measured  $NEP$  value of  $7 \times 10^{-17}$  W/Hz<sup>1/2</sup> for a normal metal volume of  $4.5 \mu\text{m}^3$  at the operating temperature  $T = 270$  mK with the time constant  $\tau = 1.2 \mu\text{s}$  [177].

High temperature superconductor SIS devices are still under investigation. In spite of possible high frequency operation, the noise level of such devices is appreciably higher.

Progress in detector technology will be connected with successful development of large-format, high-sensitivity focal plane arrays enabling a range of observations from ground-based and orbital platforms. Especially, two detector technologies show promise to develop the arrays needed in the next decade: transition-edge superconducting (TES) bolometers (see Sect. 14) and microwave kinetic inductance detectors (MKIDs) based on different principles of superconductivity. Multiple instruments are currently in development based on arrays up to 10,000 detectors using both time-domain multiplexing (TDM) and frequency-domain multiplexing (FDM) with superconducting quantum interference devices (SQUIDs) [30]. Both sensors show potential to realize the very low  $\sim 10^{-20}$  W/Hz<sup>1/2</sup> sensitivity needed for space-borne spectroscopy.

A MKID is essentially a high-Q resonant circuit made out of either superconducting microwave transmission lines or a lumped element  $LC$  resonator. In the first case, a meandered quarter-wavelength strip of superconducting material is coupled by means of a coupling capacitance to a coplanar waveguide through line used for excitation and readout. Lumped element are instead created from an  $LC$  series resonant circuit inductively coupled to a microstrip feed line. Photons hitting an MKID break the Cooper pairs which changes the surface impedance of the transmission line or inductive element. This causes the resonant frequency and quality factor to shift an amount proportional to the energy deposited by the photon. The readout is almost entirely at room temperature and can be highly multiplexed; in principle hundreds or even thousands of resonators could be read out on a single feedline [178].

MKID devices use superconductors (micro-resonators fabricated from thin aluminium and niobium films) below transition where radiation breaks Cooper pair but with smaller energy gap. Their advantages are: readout of many



Fig. 45. Prototype MKID camera constructed for the Caltech Submillimeter Observatory with 576 spatial pixels, each simultaneously sensitive in four bands at 750, 850, 1100, and 1300 microns.

devices with single coax, simple detector and multiplexer fabrications; but still need ultra low temperatures. For more details see Ref. 176. Figure 45 shows prototype MKID camera constructed for the Caltech Submillimeter Observatory with 576 antenna-coupled spatial pixels each simultaneously sensitive in four bands at 750, 850, 1100 and 1300 microns and with a total 2304 detectors [179].

## 10. Pyroelectric detectors

Many types of thermal detectors operated in LWIR and far-IR regions (including Golay cells, bolometers, pyroelectric detectors) are also used in THz band.

Commercially available uncooled pyroelectric detectors with broadband capability in the 1–1000  $\mu\text{m}$  wavelength range are fabricated using such materials as  $\text{LiTaO}_3$ ,  $\text{LiNbO}_3$ , and DLATGS (deuterated L-alanine doped triglycine sulphate) [86]. Selex Sensors has developed DLATGS pyroelectric detectors sealed and encapsulated within a thermoelectrically stabilized TO-5 package that can survive at higher operating temperature (Curie temperature is around  $59^\circ\text{C}$ ). Performance characteristics of DLATGS detector for far-IR region are given in Table 7 [180].

Improvement in pyroelectric detectors performance can be achieved by reducing the crystal thickness and increasing the coating absorption. Most of pyroelectrics tend to lose their interesting properties as the thickness is reduced. However, some of them seem to maintain their properties better than others. This seems particularly for lithium tantalate oxide ( $\text{LiTaO}_3$ ) and related materials. New material-processing techniques such as ion milling and ion slicing have made available  $\text{LiTaO}_3$  and lithium niobate oxide ( $\text{LiNbO}_3$ ) materials with a thickness of less than  $10 \mu\text{m}$ . Using the new thin-film materials, we have seen current responsivity values higher than  $4 \mu\text{A/W}$ , resulting in hybrid detector optical amplifier performance of less than  $1.0 \times 10^{-10}$  W/Hz<sup>1/2</sup> [181]. Thin-film  $\text{LiTaO}_3$  pyroelectric detectors are now commercially available. However, their absorption in the terahertz

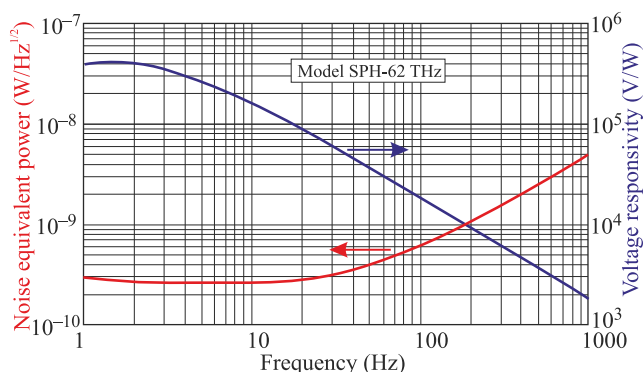
Table 7. Performance characteristics of DLATGS detector for far-IR region (after Ref. 180).

| Parameters                                     | Value  |
|--|--|
| IR spectral range ( $\mu\text{m}$ )            | 1–1000   |
| Operating temperature (K)                      | 298  |
| Element active area diameter (mm)              | 2  |
| Frequency range of operation (Hz)              | 1–3,000  |
| Thermal time constant (ms)                     | 18   |
| Detector window                                | CsI or diamond   |
| Responsivity (V/W)                             | 2440 (10 Hz)<br>300 (100 Hz)<br>30 (1000 Hz)   |
| Detectivity ( $\text{cmHz}^{1/2}/\text{W}$ )   | $6.6 \times 10^8$ (10 Hz)<br>$6.6 \times 10^8$ (100 Hz)<br>$3.5 \times 10^8$ (1000 Hz)             |
| Noise equivalent power ( $\text{W/Hz}^{1/2}$ ) | $2.7 \times 10^{-10}$ (10 Hz)<br>$2.7 \times 10^{-10}$ (100 Hz)<br>$5.1 \times 10^{-10}$ (1000 Hz) |

range remains a challenge. Some promising developments are expected in the area of single- and multiwall carbon nanotube coatings for pyroelectric detectors. Table 8 and Fig. 46 characterise LiTaO<sub>3</sub> THz pyroelectric detector – model SPH-62 THz fabricated by the Spectrum Detector Inc. [182].

## 11. Semiconductor bolometers

The classic bolometers contain a heavily doped and compensated semiconductor which conduct by a hopping process that yields the resistance  $R(T) = R_0 \exp(T/T_0)^p$ , where  $R$  is the resistance at the temperature  $T$ , and  $T_0$ , and  $R_0$  are the constants which depend on the doping and, for  $R_0$ , on the thermistor dimensions [41]. The exponent  $p$  is the constant, and it is often assumed that  $p = 0.5$ . The thermistors are made by ion implantation in Si, or by neutron transmutations doping (NTD) in Ge [54]. Figure 47 shows the experimental results at the temperature range from 70 mK to 1 K for some of the NTD Ge samples together with fitting curves, where  $p$ -value for all samples is about 0.5 [183]. NTD converts <sup>70</sup>Ge to <sup>71</sup>Ga (acceptor) and <sup>74</sup>Ge to <sup>75</sup>As (donor). Doping level depends on neutron flux, instead compensation ratio can be changed by altering isotope ratios.

Fig. 46. Frequency dependent characteristics of LiTaO<sub>3</sub> THz pyroelectric detector – model SPH-62 THz (after Spectrum Detector Inc. in Ref. 182).

The thermistors are typically fabricated by lithography on membranes of Si or SiN. The impedance is selected to a few M $\Omega$  to minimize the noise in JFET amplifiers operated at about 100 K. Limitation of this technology is assertion of thermal mechanical and electrical interface between the bolometers at 100–300 mK and the amplifiers at  $\approx 100$  K. Usually, JFET amplifiers are sited on membranes which isolate them so effectively that the environment remains at much low temperature (about 10 K), see Fig. 48. In addition, the equipment at 10 K is itself thermally isolated from nearby components at 0.1–0.3 K. There are not practical approaches to multiplexing many such bolometers to one JFET amplifier. Current arrays require one amplifier per pixel and they are limited to a few hundred pixels.

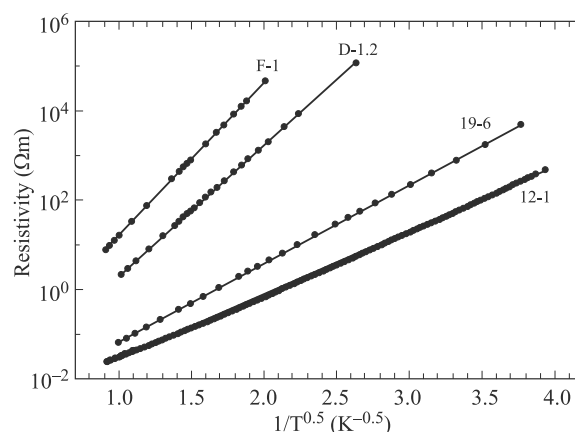


Fig. 47. Zero-bias resistivity as a function of temperature for several different NTD Ge samples (after Ref. 183).

Table 8. LiTaO<sub>3</sub> THz pyroelectric detector – Model SPH-62 THz (after Spectrum Detector Inc.).

| Parameters                                     | Value   |
|--|---|
| Detector size (mm)                             | 2×2   |
| Electronic 3db frequency (Hz)                  | 15  |
| Thermal 3db frequency (Hz)                     | 0.5   |
| Voltage responsivity (V/W)                     | $1.5 \times 10^5$                               |
| Noise equivalent power ( $\text{W/Hz}^{1/2}$ ) | $4 \times 10^{-10}$ (10.6 $\mu\text{m}$ , 5 Hz) |
| Detectivity ( $\text{cmHz}^{1/2}/\text{W}$ )   | $4 \times 10^8$ (10.6 $\mu\text{m}$ , 5 Hz)     |



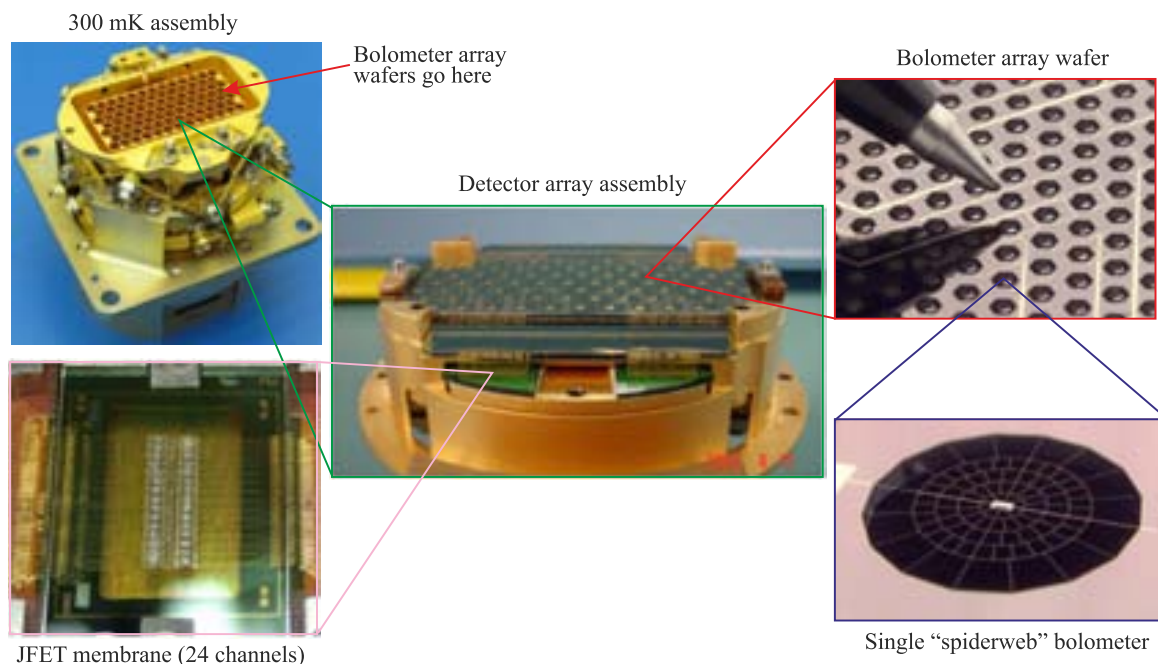


Fig. 48. Bolometer array of the spectral and photometric imaging receiver (SPIRE) (after Ref. 184).

In bolometer, metal films, that can be continuous or patterned in a mesh, absorb the photons. The patterning is designed to select the spectral band, to provide polarization sensitivity, or to control the throughput. Different bolometer architectures are used. In close-packed arrays and spider web, the pop-up structures or two-layer bump bonded structures are fabricated. Agnese *et al.* have described a different array architecture which is assembled from two wafers by indium bump bonds [185]. Other types of bolometers are integrated in horn-coupled arrays. To minimize low frequency noise, an AC bias is used.

The present day technology exist to produce arrays of hundreds of pixels that are operated in the spectral range from 40 to 3000  $\mu\text{m}$  in many experiments including NASA pathfinder ground based instruments, and balloon experiments such as BOOMERANG, MAXIMA, and BAM. In Table 9, there are gathered the requirements for typical astronomic instruments containing bolometers. To fulfil these requirements, the compromise between response time and  $NEP$  is needful. A spider web bolometer from the BOOMERANG experiment, which is being used on space experiments (Planck and Herschel missions) is shown inside Fig. 48.

An alternative approach is array for the SHARCII instrument on SOFIA shown in Fig. 49(a) [186]. This array construction, with 12  $\times$  32 pixels, involves a pop-up configuration, where the absorber is deposited on a dielectric film that is subsequently folded. The 12 $\times$ 32 bolometer array, load resistors, and thermally-isolated JFETs are housed in a structure approximately 18 $\times$ 17 $\times$ 18  $\text{cm}^3$  volume, having a total mass of 5 kg, and heat sink to 4 K. Each bolometer is fabricated on a 1- $\mu\text{m}$  silicon membrane and has a collecting area of 1 $\times$ 1  $\text{mm}^2$ . The full area is ion implanted with phosphorus and boron, to a depth of  $\approx 0.4 \mu\text{m}$ , to form a thermistor. Electrical contact between the thermistor and aluminium traces on the silicon frame is accomplished with degenerately-doped leads on the edge of the thermistor and running down the bolometer legs. Each of the four thermally-isolating legs is 16  $\mu\text{m}$  wide and 420  $\mu\text{m}$  long. Prior to folding, each bolometer is coated with an absorbing  $\approx 200 \text{ \AA}$  bismuth film and a protective  $\approx 160 \text{ \AA}$  SiO film. At a base temperature of 0.36 K and in the dark, the bolometers have a peak responsivity of approximately  $4 \times 10^8 \text{ V/W}$  and a minimum  $NEP$  of approximately  $6 \times 10^{-17} \text{ W/Hz}^{1/2}$  at 10 Hz. Phonon noise is the dominant contributor, followed by bolometer Johnson noise.

Table 9. Requirements for typical astronomic instruments.

| Instrument | Wavelength range ( $\mu\text{m}$ ) | $NEP$ ( $\text{W/Hz}^{1/2}$ ) | $\tau$ (ms) | $NEP\tau^{1/2}$ ( $\times 10^{-19} \text{ J}$ ) | Comments                                  |
|------------|------------------------------------|-------------------------------|-------------|---|---|
| SCUBA      | 350–850                            | $1.5 \times 10^{-16}$         | 6           | 9   | High background, needs reasonable $\tau$  |
| SCUBA-2    | 450–850                            | $7 \times 10^{-17}$           | 1–2         | 1   | Lower background, need faster $\tau$      |
| BoloCAM    | 1100–2000                          | $3 \times 10^{-17}$           | 10          | 3   | Lower background, slower device okay      |
| SPIRE      | 250–500                            | $3 \times 10^{-17}$           | 8           | 2.4   | Space background, slower device okay      |
| Planck-HFI | 350–3000                           | $1 \times 10^{-17}$           | 5           | 0.5   | Lowest background, need quite fast $\tau$ |



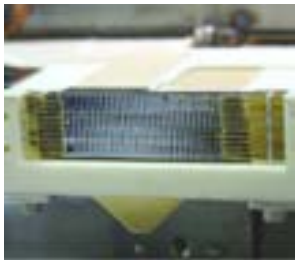

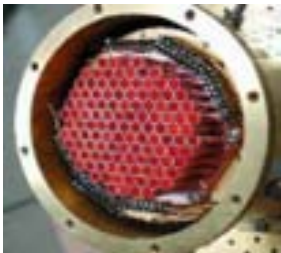
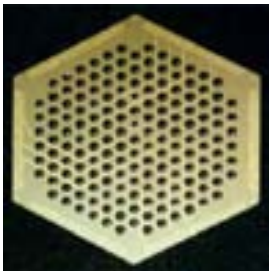
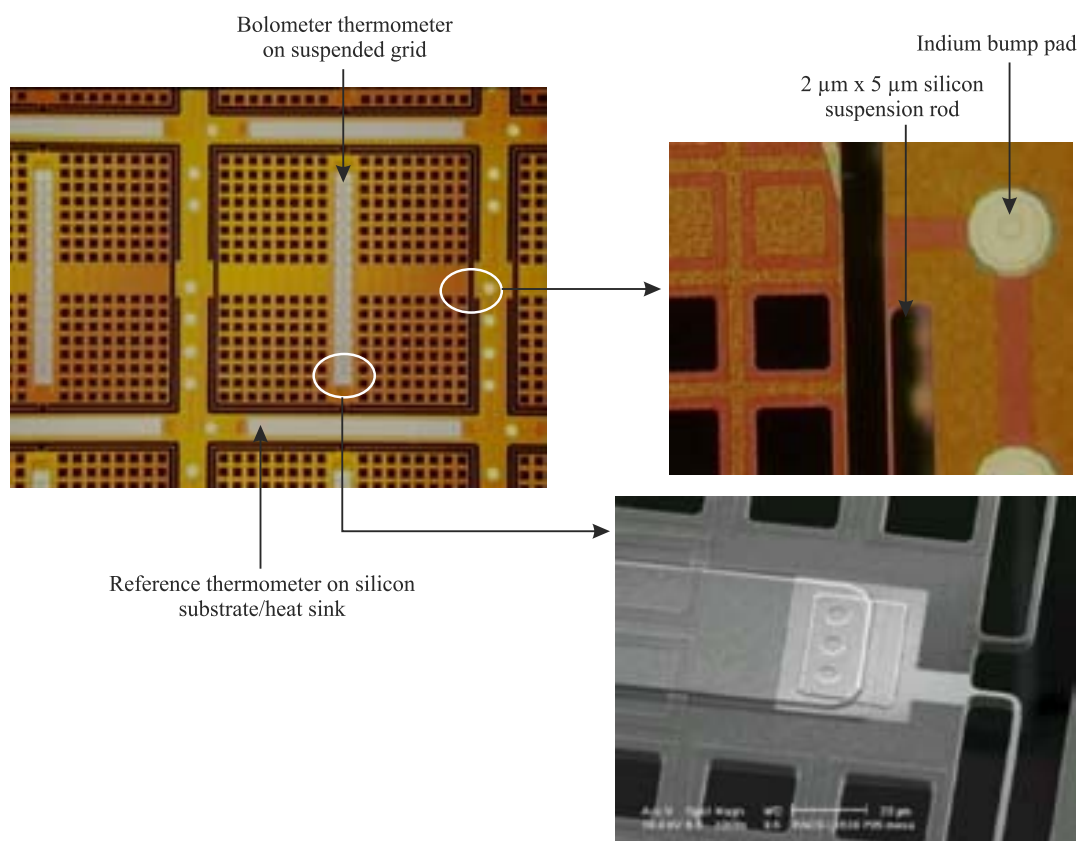
| CSO-SHARCII (2004)<br>$\lambda = 350 \mu\text{m}$                                 | JCMT-SCUBA (1997)<br>$\lambda = 450/850 \mu\text{m}$                              | IRAM-MAMBO-2<br>$\lambda = 1.2 \text{ mm}$   | CSO-BOLOCAM (2001)<br>$\lambda = 1.4 \text{ mm}$                                    |
|---|---|--|---|
|  |  |  |  |
| Si – 384 pixels   | 91/31 pixels  | 117 pixels   | Ge – 151 pixels   |
| (a)   | (b)   | (c)  | (d)   |

Fig. 49. Arrays installed in ground-based telescopes.

With the development of low-noise readouts, that can operate near the bolometer temperature, the first true high-performance bolometer arrays for the far IR and sub-mm spectral ranges are just becoming available. For example, the Herschel/PACS instrument uses a 2048-pixel array of bolometers [142,187] and it is an alternative to JFET amplifiers. The architecture of this array is vaguely similar to the direct hybrid mid-infrared arrays, where one silicon wafer is patterned with bolometers, each in the form of a silicon mesh, as shown in Fig. 50. The development of silicon micromachining has enabled substantial advances in bolometer construction generally and is central to making

large-scale arrays. To achieve appropriate response and time constant characteristics, the rods and mesh are designed carefully. The mesh is blackened with a thin layer of titanium nitride with sheet resistance matched to the impedance of free space ( $377 \Omega$  /  $\square$  section of film) to provide an efficiency of 50% over a broad spectral band. Each bolometer located at the centre of the mesh, containing a silicon-based thermometer doped by ion implantation, is characterized by appropriate temperature-sensitive resistance. Their large resistances ( $> 10^{10} \Omega$ ) are well adjusted to MOSFET readout amplifiers. In final step of hybrid array fabrication, the MOSFET-based readouts and silicon

Fig. 50. The Herschel/PACS bolometer array with pixel size  $750 \mu\text{m}$  (after Ref. 188).

bolometer wafer are joined by indium bump bonding. Performance is currently limited by the noise in the MOSFET amplifiers to the  $NEP \approx 10^{-16} \text{ W/Hz}^{1/2}$  regime, but this technology allows the construction of very large arrays suitable for higher background applications. Further details are in Billot *et al.* [187].

## 12. Semiconductor hot electron bolometers

If the bolometer is to be used as a THz mixer, it has to be fast enough to follow the IF, i.e., the overall time constant of the processes involved in the mixing has to be a few tens of picoseconds at maximum. In other words, high heat conductivity and small heat capacity are required [45]. These requirements can be fulfilled by such subsystem as electrons in semiconductor or superconductor interacting with the lattice (phonons). Electron heat capacity is many orders lower compared to the lattice one.

The term “hot electrons” was introduced to describe nonequilibrium electrons in semiconductors [189]. In this case, the electron distributions could be formally described by the Fermi function distribution, but with an effective elevated temperature. This concept fruitfully was applicable to semiconductors, where the carrier mobility depends on the effective temperature. In metals, mobility changes are much less pronounced and electron heating does not affect the metal resistance unless the change in the effective temperature is comparable with the temperature at Fermi level.

In the normal bolometer, the crystal lattice absorbs energy and transfers it to the free carriers via collisions. However, in hot electron bolometer, the incident radiation power is absorbed directly by free carriers, the crystal lattice temperature remaining essentially constant. Note that this mechanism differs from photoconductivity in that free-electron mobility rather than electron number is created by incident light. At low temperature, the mobility of the electrons varies as  $T_e^{3/2}$ , where  $T_e$  is the electron temperature, and the conductivity of the material is modulated by mobility. This mechanism offers submicrosecond response and broad far-

-infrared coverage out to millimeter wavelengths but requires liquid-helium cooling.

First bolometer with “hot electrons” (hot electron bolometer – HEB) was low temperature bulk n-InSb [190,191]. Currently, this detector uses a specially shaped high purity n-type InSb crystal which may be coupled directly to a very low noise preamplifier. Parameters of InSb HEB manufactured by the Infrared Laboratories are given in Table 10 [192]. Figure 51 shows spectral dependence of detectivity of InSb HEB [193].

Table 10. Parameters of InSb HEB manufactured by the Infrared Laboratories (after Ref. 192).

| Parameter                      | Value   |
|--------------------------------|---|
| Detector area (mm)             | 5×5   |
| Detector mounting              | Sapphire substrate set into an integrating cavity |
| Operating temperature (K)      | 1.5–4.2   |
| Spectral response (mm)         | 0.2–6   |
| Frequency response – 3db (kHz) | 600   |
| $NEP$ (W/Hz <sup>1/2</sup> )   | < 8×10 <sup>-13</sup>                             |

Today, also other semiconductor materials are proposed in HEBs fabrication [194–196]. In spite of the fact that the rate of electron heating is extremely high because of high rate of photon-electron interaction, the maximum transformation frequency is restricted by the thermal relaxation rate, which in semiconductors is governed by electron-phonon interaction time  $\tau \approx 10^{-7}$  s at low temperatures [197]. This response time is relatively short, compared to convention thermal detectors with lattice heating, but long compared to  $\tau$  in superconducting HEBs. Thus, for direct detection semiconductor systems the speed of response is quite suitable, but not for the mixers. Their  $NEP$  can reach  $5 \times 10^{-13} \text{ W/Hz}^{1/2}$  at operation temperature about 4 K and below.

Nonlinearity of semiconductor HEB current-voltage characteristic, needed for heterodyne detector operation, is conditioned by the dependence of conductivity on electron mobility, which is a function of applied electric field, thereby the function of electrons temperature. Higher IFs and broader  $\Delta f$  can be obtained in semiconductor HEB frequency converters increasing their temperature to about 80 K (where electron-phonon interaction is much stronger and  $\tau \approx 10^{-11}$  s), but in this case, the noise level of such frequency converters is increasing appreciably and conversion losses are increasing fast too.

In low-dimensional semiconductor structures, the electron-phonon interaction can be substantially increased ( $\tau$  decreased) and, thus, such kind of structures can be considered as frequency converters with higher IFs and wider bandwidth up to  $10^9$  Hz [198–200]. Direct measurements of photoresponse relaxation time have shown that  $\tau$  is about 0.5 ns in the temperature range 4.2–20 K [201]. Thus, the IF can be increased by about 3 orders compared to bulk semiconductor HEBs.

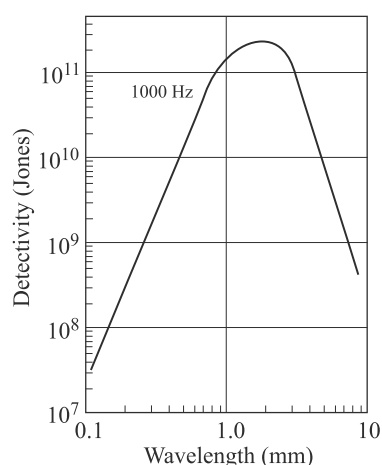


Fig. 51. Detectivity vs. cut-off wavelength for InSb HEB detector (after Ref. 193).

Historically, HEB mixers using semiconductors were invented in the early 1970s [188] and played an important role in early sub-mm astronomy [202], but they were superseded by SIS mixers by the early 1990s. However, the development of superconducting HEB versions led to the most sensitive THz mixers at frequencies beyond the reach of SIS mixers. The main difference between HEB mixers and ordinary bolometers is the speed of their response. HEB mixers are fast enough to allow GHz output IF bandwidths.

### 13. Superconducting hot-electron bolometers

In principle, hot-electron bolometer (HEB) is quite similar to the transition-edge bolometer (see Sect. 14), where small temperature changes, caused by the absorption of incident radiation, strongly influence resistance of biased sensor near its superconducting transition. The main difference between HEBs and ordinary bolometers is the speed of their response. High speed is achieved by allowing the radiation power to be directly absorbed by the electrons in the superconductor, rather than using a separate radiation absorber and allowing the energy to flow to the superconducting TES via phonons, as ordinary bolometers do. After photon absorption, a single electron initially receives the energy  $h\nu$ , which is rapidly shared with other electrons, producing a slight increase in the electron temperature. In the next step, the electron temperature subsequently relaxes to the bath temperature through emission of phonons.

In comparison with TES, the thermal relaxation time of the HEB's electrons can be made fast by choosing a material with a large electron-phonon interaction. The development of superconducting HEB mixers has led to the most sensitive systems at frequencies in the terahertz region, where the overall time constant has to be a few tens of picoseconds. These requirements can be realized with a superconducting microbridge made from NbN, NbTiN, or Nb on a dielectric substrate [12].

HEBs can work according to two mechanisms that allow electrons to exchange their energy faster than they heat the phonons:

- phonon-cooled HEB principle – was suggested by Gerhenzon *et al.* [203] and the first realized by Karasik *et al.* [204],
- diffusion-cooled HEB principle – was suggested by Prober [205] and the first realization reported by Skalar *et al.* [206].

A synthetic presentation of both mechanisms has been given by McGrath [207].

Figure 52(a) shows the basic operation of the phonon-cooled bolometer. In this type of device, hot electrons transfer their energy to the phonons with the time  $\tau_{eph}$ . In the next step, the excess of phonon energy escapes towards the substrate with the time  $\tau_{esc}$ . Several conditions should be fulfilled to make phonon-cooled mechanism effective:

- electron-electron interaction time  $\tau_{ee}$  must be much shorter than  $\tau_{eph}$ ,

- superconducting film must be very thin (a few nm) and the film to substrate thermal conductance must be very high ( $\tau_{esc} < \tau_{eph}$ ) to obtain an efficient phonon escape from superconductor to substrate,
- substrate thermal conductivity must be very high and very good thermal contact between substrate and cold finger must be insured.

In diffusion-cooled bolometer, which principle of mechanism is shown in Fig. 52(b), hot electrons transfer their energy by diffusion to a normal metal that forms the electrical contacts to the external detector readout circuitry and/or the arms of a planar antenna. In this case, the length of the superconducting microbridge must be very short, with the maximum value  $L_{max} = 2(D_e \tau_{ee})^{1/2}$ , where  $D_e$  is the electron diffusivity. As it was shown by Burke *et al.*, the bolometer bandwidth is inversely proportional to the squared microbridge length, which lies in the submicronic range (see Fig. 53) [208]. The bandwidth of diffusion-cooled bolometers is not limited by  $\tau_{eph}$ . As a result, in comparison with phonon-cooled bolometers, larger intermediate frequency values are obtained. For diffusion cooling, the interface between the contact pads and the superconducting film is crucial, while for phonon cooling, the interface between the film and the substrate is crucial. It should be pointed out that the distinction is, to some extent, arbitrary since phonon cooling also exists in diffusion cooled bolometers and vice versa.

The ratio of phonon to electron specific heats  $C_p/C_e$  controls the energy flow from electrons to phonons and the energy backflow due to reabsorption of nonequilibrium

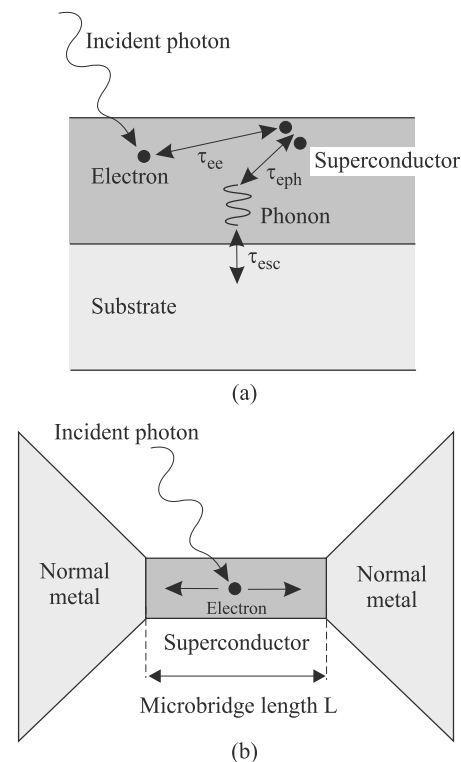


Fig. 52. Hot-electron bolometer mechanisms: phonon-cooled (a) and diffusion-cooled (b) principles.

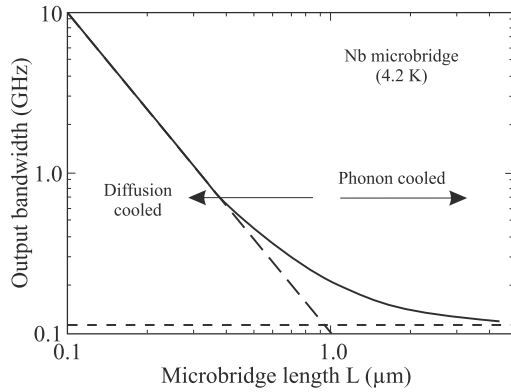


Fig. 53. Output bandwidth as a function of microbridge length for niobium HEB mixers. For  $L$  shorter than  $1\ \mu\text{m}$ , the cooling mechanism is by electron diffusion to a normal metal; for larger  $L$ , the phonon-cooling mechanism is the dominant one (after Ref. 208).

phonons by electrons. This ratio is 0.85 for Nb, 6.5 for NbN, and 38 for YBaCuO layers [209]. In very thin films, the phonons can escape into the substrate before being reabsorbed by the electrons. In thin, below 10-nm thick Nb films, deposited on a substrate,  $\tau_{phe} > \tau_{eph}$  and the effective escape of phonons to the substrate prevail energy backflow to electrons. As a result,  $\tau_{eph}$  alone controls the response time, which is approximately equal to about 5 ns. Thus, Nb devices are sensitive in wide range of spectra, they are much faster compared to bulk semiconductor bolometers (operating at  $T \approx 4\ \text{K}$ ), and they can reach  $NEP \approx 3 \times 10^{-13}\ \text{W/Hz}^{1/2}$  [210].

Karasik *et al.* have demonstrated hot-electron superconducting direct detection Ti nanobolometers fabricated on Si planar bulk substrates with Nb contacts and electrical  $NEP$  value of  $3 \times 10^{-19}\ \text{W/Hz}^{1/2}$  at 300 mK [47]. The time constant of cooled HEBs can reach value in wide range from  $10^{-5}$  to  $10^{-10}$  s. The thermal time constant  $\tau_{eph} = 25\ \mu\text{s}$  at  $T = 190\ \text{mK}$  for larger devices has been demonstrated. For the first time, the record optical  $NEP = 3 \times 10^{-19}\ \text{W/Hz}^{1/2}$  at  $\lambda = 460\ \mu\text{m}$  and  $T = 50\ \text{mK}$  has been achieved [65]. Such high sensitivity meets the requirements for SAFARI instrument on the SPICA telescope.

NbN films in comparison to Nb ones have much shorter  $\tau_{eph}$  and  $\tau_{phe}$  because of stronger electron-phonon interaction. In ultrathin 3-nm thick NbN films, both  $\tau_{eph}$  and  $\tau_{phe}$  determine the response time of the detector, which can be about 30 ps near  $T_c$  ( $\tau_{eph} \approx 10\ \text{ps}$ ) [211].  $NEP$  can reach the values of  $10^{-12}\ \text{W/Hz}^{1/2}$  [212].

Since for YBaCuO detector layers the ratio  $C_p/C_e \approx 38$ , the layers are mainly phonon-cooled type; the energy backflow from phonons to electrons can be neglected and thermalization time is about an order faster ( $\tau_{eph} \approx 1\ \text{ps}$ ) compared to NbN layers. In YBaCuO films excited by fs pulses, the non-thermal (hot-electron) and thermal bolometric (phonon) processes are practically decoupled, with the former one dominating the early stage of electron relaxation. To decouple electrons from phonons, non-equilibrium phonons in the film should escape from it (into the substrate) in short time compared to the phonon-electron time  $\tau_{phe}$ .

A major issue for HEB mixers is achieving a thermal time constant that is fast enough to yield a useful IF output bandwidth of a few GHz. For a fixed thermal relaxation time, the heat capacity sets the required LO power and can be minimized by using a very small volume ( $< 10^{-2}\ \mu\text{m}^3$ ) of a superconducting film. The required LO power is about one order of magnitude lower (typically between 100 and 500 nW) compared to SIS mixers and much lower (roughly 3–4 orders) in comparison with SBDs. The LO power scales with the volume of the microbridge and decreases with increasing critical temperature [213].

The HEB mixers are thermal detectors and belong to the group of square-law mixers. Theory of HEBs is still under development and typically invokes a hot-spot resistive region in the centre, whose size responds to changes in the applied power. This model was originally developed by Skocpol *et al.* [214], and was later applied to superconducting HEB mixers [48,209,215]. The region, where the actual temperature exceeds the critical temperature and switches into the normal state, is called the hot-spot (see Fig. 54, Ref. 216). When LO signal is applied to the superconducting micro-bridge, central part of the microbridge become normal, resistive due to the standing wave then, hot-spot forms and its boundaries begin to move toward the electric contacts until the hot spot reaches thermal equilibrium. When the RF is applied, the LO power is modulated and the length of the hot-spot oscillated periodically, with the frequency the same as the IF frequency. The speed of boundaries determines the response time, but other effects such as the interaction of radiation with magnetic vortices play a role. When comparing diffusion-cooled and phonon-cooled HEBs, the latter provide a smaller noise temperature, and they are therefore, preferred.

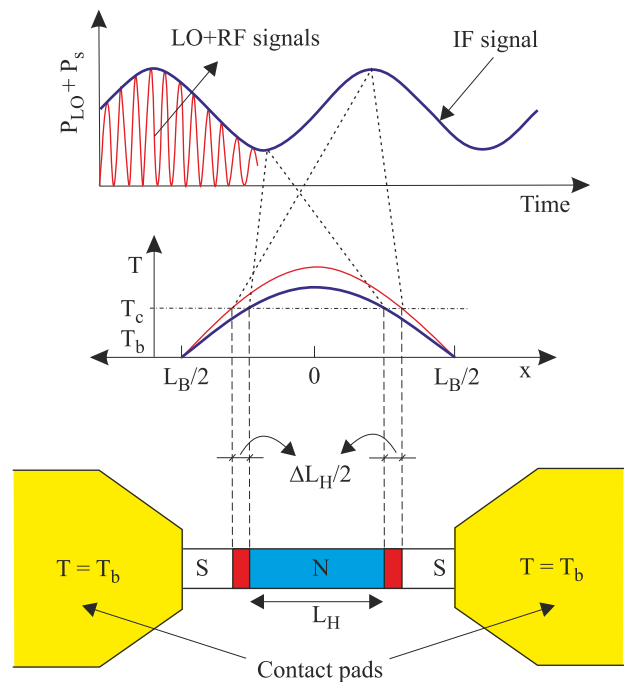


Fig. 54. Hot-spot model of HEB mixer (after Ref. 216).



THz detector is much smaller than the wavelength being received. Therefore, an antenna and associated coupling circuitry are needed to bring the radiation to the detector. In 1977, Schwarz and Ulrich reported the first paper devoted to room temperature antenna coupled metallic film infrared detectors [217]. In contrast to absorbing layer coupling, antenna coupling gives selective responsivity to both the spatial mode and the polarization of the incoming radiation. In the case of microbolometers, an antenna with rather large effective area can feed a superconducting microbridge of much smaller detector area (a few  $\mu\text{m}^2$ ).

A large number of antennas were proposed (see, e.g. Refs. 218 and 219) including dish and horn antennas, log-periodic, spiral, slots/apertures, bow-tie, etc. For printed antennas, for radiation effective transmission and reception, they should be about the half of the wavelength  $\lambda$ . Detector's sensitivity is proportional to the antenna effective area  $S_{\text{eff}}$ . The antenna effective area  $S_{\text{eff}}$  and the antenna gain  $G$  are linked by [218]

$$S_{\text{eff}} = \frac{\lambda^2}{4} G, \quad (22)$$

where  $\lambda$  is the wavelength. Thus, with the frequency  $\nu = c/\lambda$  increase, the effective antenna area reduces, as the gain  $G$  depends on antenna design, dielectric substrate properties, etc. and it much weaker depends on the wavelengths.

Two frequency-independent antenna families, shown in Fig. 55, can be built. In the first one, the antenna geometry is defined by angles (not by geometrical lengths) [220]; bow-tie and spiral antennas fall into so-called equiangular antennas. In the second family [see Fig. 55(c)], the antenna is built up from coupled elements (e.g. dipoles). The finite dimensions of the structures restrict the antenna bandwidth roughly from  $2r_{\text{min}}$  to  $2r_{\text{max}}$  in terms of wavelength. Perturbations in the radiation bandwidth limits are overcome with the log-periodic structure.

Another class of antenna structures belongs to end-fire antennas, which are derived from long wire travelling wave antennas. As opposed to previously described structures, whose radiation direction lies in a plane orthogonal to the antenna plane, it lays into the antenna plane for end-fire geometries. These structures offer the possibility of making compact detector arrays with pixels containing V-antennas.

Two methods are used to obtain useful IF output bandwidth:

- phonon cooling, using ultrathin NbN or NbTiN films characterized by large electron-phonon interaction,
- diffusion cooling, using sub-micron Nb, Ta, NbAu, or Al devices coupled to normal-metal cooling "pads" or electrodes.

Competitive sensitivities have been demonstrated for both types of devices.

Typically, phonon-cooled HEBs are made from ultrathin films of NbN, whereas diffusion-cooled devices use Nb or Al. Current state-of-the-art NbN technology is capable of routinely delivering 3-nm thick devices that are 500 nm<sup>2</sup> in size. NbN films are deposited on a dielectric (typically high resistivity > 10 k  $\Omega\cdot\text{cm}$  silicon). The superconducting bridge is defined by means of electron beam lithography. Its length varies between 0.1 and 0.4  $\mu\text{m}$  and the width between 1 and 4  $\mu\text{m}$ .

Figure 56(a) presents an example cross-section view of NbN mixer chip. About 150-nm thick Au spiral structure is connected to the contacts pads. The superconducting NbN film extends underneath the contact layer/antenna. The central area of a mixer chip shown in Fig. 54(b) is manufactured from a 3.5-nm-thick superconducting NbN film on a high resistive Si substrate with an e-beam evaporated MgO buffer layer [221]. Ultrathin NbN films are deposited by reactive magnetron sputtering in the Ar + N<sub>2</sub> gas mixture. The active NbN film area is determined by the dimensions of the 0.2- $\mu\text{m}$  gap between the gold contact pads. The NbN microstrip is integrated with a planar antenna patterned as log-periodic spiral. The NbN critical temperature depends on thickness of film deposited on a substrate. An improvement in superconducting properties of NbN films, due to the presence of MgO buffer layer on silicon substrates, is evident [see Fig. 56(c)]. The superconducting transition temperature is about 9 K and the transition widths are  $\approx 0.5$  K.

The NbN superconductive HEB mixers are characterized by strong electron-phonon interaction. The response time can achieve the value of  $10^{-11}$  s [211], and because of no principal restrictions for operation at  $\nu > 1$  THz (the absence of their noticeable capacities), these devices can be effectively used for heterodyne detection in wide spectral range up to the visible one, where operation, e.g., of SIS mixers, is hampered. For example, Fig. 57 shows intermediate frequently dependent output power for the 3.5-nm thick NbN film devices deposited on plain of MgO substrate (curve A) and on Si substrate with MgO buffer layer (curve B).

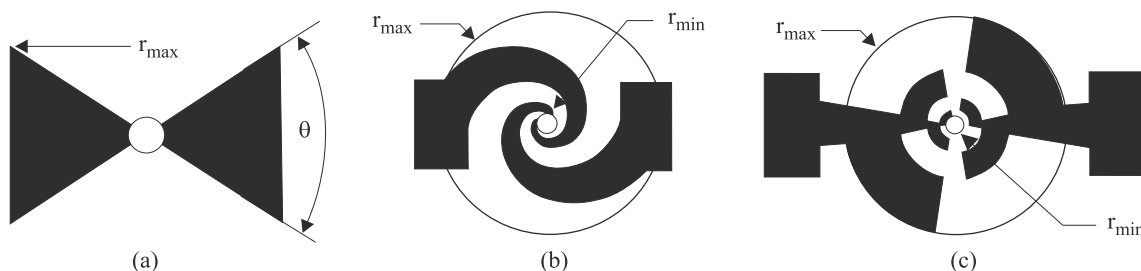


Fig. 55. Frequency-independent planar antenna geometries: (a) bow-tie equiangular, (b) spiral equiangular, and (c) circular log-periodic. The sensing element is located at the centre of the structure (after Ref. 220).

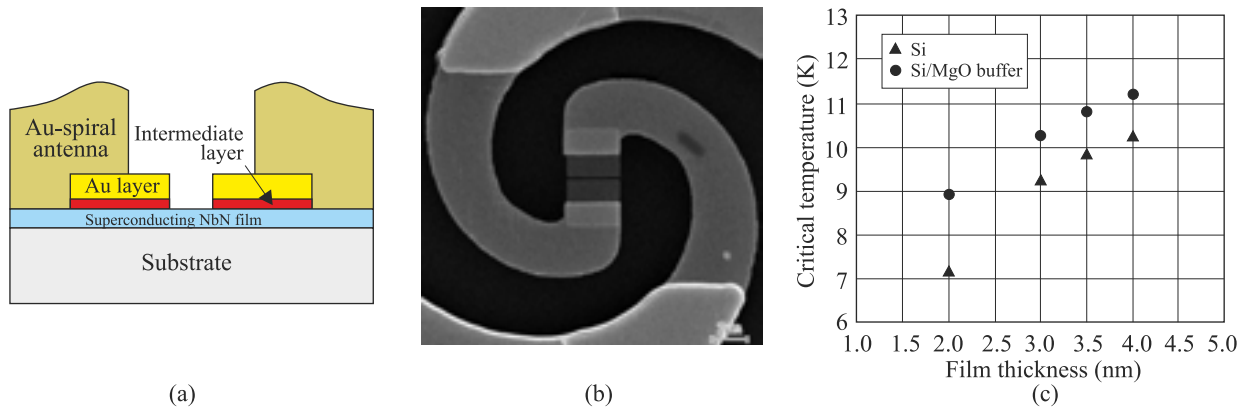


Fig. 56. NbN HEB mixer chip: (a) cross section view, (b) SEM micrograph of the central area of mixer, (c) critical temperature vs. thickness for NbN films deposited on Si substrates (triangles) and on Si with MgO buffer layer (circles) (after Ref. 221).

B). The frequency limited range to several GHz is due to influence of free carrier relaxation rate.

HEB mixers can be made either in a waveguide configuration with a horn antenna or as quasi-optical mixers. The more traditional approach is waveguide coupling, in which radiation is first collected by a horn into a single-mode waveguide (typically a rectangular guide), and then, a transition (probe) couples radiation from the waveguide onto a lithographed thin-film transmission line on the detector chip. One major complication of the waveguide approach is that the mixer chip must be very narrow, and must be fabricated on an ultrathin substrate. These requirements are helpful using modern micromachining techniques (see Fig. 58).

Above  $\sim 1$  THz, the quasi-optical coupling is more common. This coupling approach omits the intermediate step of collecting the radiation into a waveguide, and instead it uses a lithographed (printed) antenna (e.g. twin-slot or a logarithmic spiral antenna) on the detector chip itself. Such mixers are substantially simpler to fabricate and may be produced using thick substrate (see Fig. 59). The substrate with the feed antenna and microbridge is mounted to the reverse side of a hyperhemispherical or elliptical lens. The reflection

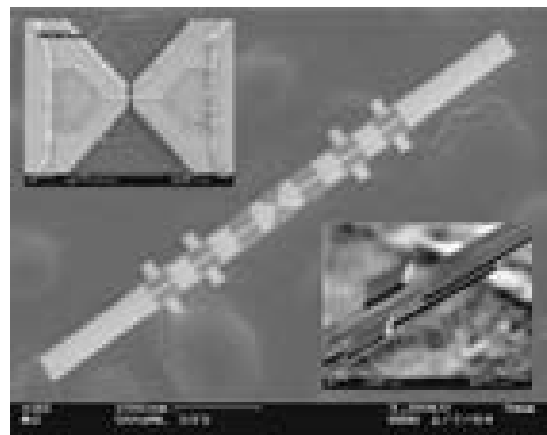


Fig. 58. Images of a 585-GHz diffusion-cooled HEB mixer chip for a waveguide mount, fabricated using an ultrathin silicon substrate. The dimensions of the HEB bridge are 150 nm long by 75 nm wide; the chip itself is 800  $\mu\text{m}$  long and 3  $\mu\text{m}$  thick. Protruding from the sides and ends of the chip there are 2- $\mu\text{m}$  thick gold leads, which provide electrical and thermal contact to the waveguide block, as well as mechanical support for the chip (after Ref. 12).

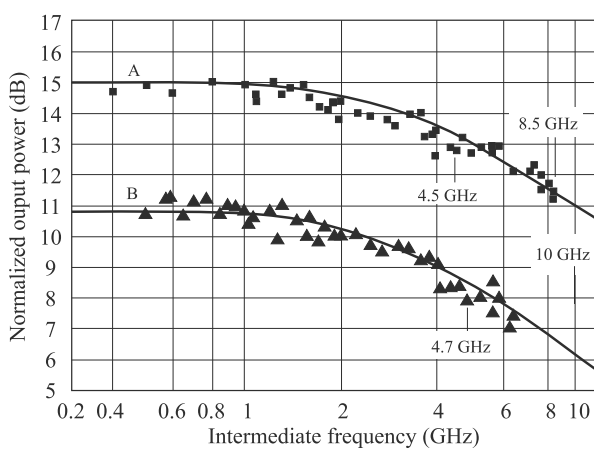


Fig. 57. Output power as a function of intermediate frequency for the 3.5-nm-thick NbN film devices deposited on plain of MgO substrate (curve A) and on Si substrate with MgO buffer layer (curve B) (after Ref. 221).

loss at the lens surface can be minimized with a quarter-wavelength antireflection coating.

HEBs are significantly more sensitive than SBDs but somewhat less sensitive than SIS mixers – see Fig. 15. This figure shows that DSB noise temperature, achieved with HEB mixers, ranges from 400 K at 600 GHz up to 6800 K at 5.2 THz. In the lower frequency range up to 2.5 THz, the

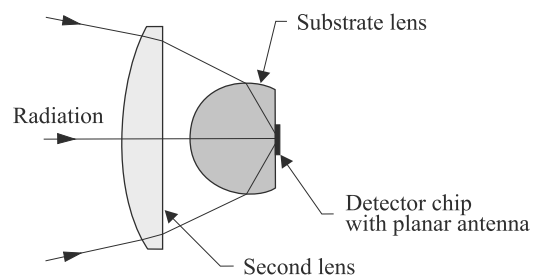


Fig. 59. Schematic diagram of the “reverse-microscope” quasi-optical coupling approach pioneered by Rutledge and Muha [222].

noise temperature follows closely the  $10h\nu/k$  line. Above this frequency, the correspondence becomes somewhat worse, what is caused by increasing losses in the optical components, lower efficiency of the antenna and skin effect contributions in the superconducting bridge.

Because of high sensitivity, NbN HEB mixers are currently the first choice for heterodyne spectroscopy above 1 THz. Examples are mixers used in Herschel and SOFIA missions.

Concerning high temperature superconductor (HTSC) HEBs, it should be noted that there do not exist numerous publications devoted to this kind of receivers. They have not reached high state of technological maturity since their complicated composition does not allow fabrication of very thin layers with high critical temperature. Kreisler and Gauge reviewed antenna-coupled high- $T_c$  bolometers for both homodyne and heterodyne applications in the FIR and THz frequencies [220,223]. HTSC belongs to the phonon cooled type and electron diffusion mechanism is negligible [209, 223,224]. These receivers are noticeably noisier, compared to low temperature devices, as phonon dynamics play an appreciable role due to the relatively high operating temperature and introduce of excess noise [225,226]. Actually, HTSC HEB mixers are not reaching the sensitivity of low temperature superconducting HEBs, but because of very short electron-phonon relaxation time ( $\tau_{eph} \approx 1.1$  ps in YBaCuO [227]), these HTSC HEB mixers are the wide bandwidth devices.

Experimental data for YBa<sub>2</sub>Cu<sub>3</sub>O<sub>7</sub>. Josephson detectors gave  $NEP$  value close to  $8 \times 10^{-15}$  W/Hz<sup>1/2</sup> at  $T = 80$  K ( $\nu = 86$  GHz) and  $NEP \approx 3 \times 10^{-13}$  W/Hz<sup>1/2</sup> for  $T = 55$  K ( $\nu = 692$  GHz) [228]. Lyatti *et al.* have concluded that HTSC HEB mixers can reach  $NEP$  value of  $5 \times 10^{-15}$  W/Hz<sup>1/2</sup> [229].

## 14. Transition edge sensor bolometers

The name of the transmission-edge sensor (TES) bolometer is derived from its thermometer, which is based on thin superconducting films held within transition region, where it changes from the superconducting to the normal state over a temperature range of a few milliKelvin (see Fig. 60). The film has stable but very steep dependence of resistance on temperature in a transition region. Changes in temperature transition can be set by using a bilayer film consisting of a normal material and a layer of superconductor. Such design enables diffusion of the Cooper pairs from the superconductor into the normal metal and makes it weakly superconducting – this process is called the proximity effect. As a result, the transition temperature is lowered relative to that for the pure superconducting film. Thus, in principle, the TES bolometers are quite similar to the HEBs. In the case of HEB, high speed is achieved by allowing the radiation power to be directly absorbed by the electrons in superconductor. In TES bolometers, however, rather a separate radiation absorber is used that allows the energy to flow to the superconducting TES via phonons, as ordinary bolometers do.

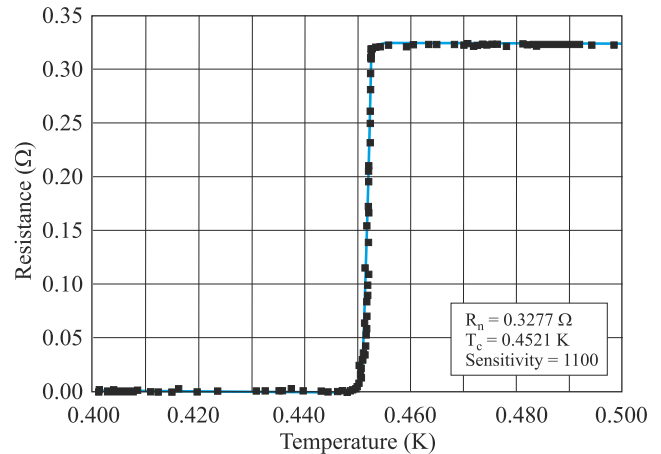


Fig. 60. Resistance vs. temperature for a high-sensitivity TES Mo/Au bilayer with superconducting transition at 444 mK (after Ref. 230).

TES bolometers are superior to current-biased particle detectors in terms of linearity, resolution, and maximum count rate. At present, these detectors can be applied for THz photons counting because of their high sensitivity (electrical  $NEP \sim 3 \times 10^{-19}$  W/Hz<sup>1/2</sup> at  $T = 300$  mK) and low thermal time constant ( $\tau = 25$   $\mu$ s at  $T = 190$  mK) [47,231]. Membrane isolated TES bolometers are capable of reaching a phonon  $NEP \approx 4 \times 10^{-20}$  W/Hz<sup>1/2</sup> [41]. The current generation of sub-orbital experiments largely rely on TES bolometers. Important feature of this sensor is that it can operate in wide spectral band, between the radio and gamma rays [12,232–236].

The temperature of a TES can be tailored by using a bilayer film consisting of a thin layer of normal metal and a thin layer of superconductor, resulting in a tuneable transition temperature. Different type of superconducting metal film pairs (bilayers) can be used including thin Mo/Au, Mo/Cu, Ti/Au, etc. Two metals behave as a single film with a transition temperature between 800 mK (for Mo) and 0 K (for Au). Transition temperature can be tuned within this temperature range. The lower temperature ( $T < 200$  mK) is needed because the energy resolution of these devices scales with temperature.

Traditionally, the superconducting bolometer was biased with a constant current and read out with a voltage amplifier. Then, the bias power  $P_b = I^2 R$  increased with temperature due to the increase in the resistance  $R$  near  $T_c$ . In consequence, a positive electrothermal feedback leads to instability and even thermal runaway. The new idea of a negative electrothermal feedback proposed by Irwin stabilizes the temperature of the TES at the operating point on the transition [232]. When TES temperature rises, due to power from absorbed photons, their resistance rises, the bias current drops, and the electrical power dissipation in them decreases, partially cancelling the effects of the absorbed power and limiting the net thermal excursion. The advantages of TES with negative feedback include linearity, bandwidth, and immunity of the response to changes in external

parameters (e.g., the absorbed optical power and the temperature of the heat sink). Consequently, these devices are suitable for fabrication of large format horn-coupled and filled arrays required for many new missions offering advantages over semiconducting bolometers [237–239].

In practice, the bias voltage  $V_b$  is chosen so that, for the small optical power  $P$ , the TES will be heated to a steep point on the temperature transition. For intermediate values of  $P$ , the electrothermal feedback keeps the total power input  $P + V^2/R$  (and, thus, the temperature) constant. The current responsivity is defined as the response of the bolometer current  $I$  to a change in the optical power. Then, for a thermal circuit with a single pole response is equal to [12,240]

$$R_i = \frac{dI}{dP} = \frac{1}{V_b} \frac{L}{(L+1)} \frac{1}{(1+i\tau)}, \quad (23)$$

where  $L = P/GT$  is the loop gain,  $G = (T/R)dR/dT$  is the measure of the steepness of the superconducting transition and is a bolometer figure of merit,  $G = dP/dT$  is the differential thermal conductance, and  $\tau$  is the effective time constant. For the typical loop gain  $L \approx 10^2$  [232,236,239], the low-frequency responsivity becomes  $R_i \approx -1/V_b$ , and depends only on the bias voltage and is independent of the signal power and the heat sink temperature. The effective time constant  $\tau = \tau_o/(1+L)$  is much shorter than the time constant without feedback  $\tau_o = C/G$  for thermal detectors. Negative electrothermal feedback can make the bolometers operate tens or even hundreds of times faster. The values of  $\tau$  for Mo/Cu proximity-effect layers ( $T_c = 190$  mK) consistent with thermal fluctuation noise [241] are within 100–250 [242].

The resistance of a TES is low, so it can deliver significant power only to low-input impedance amplifiers, which rules out JFETs and MOSFETs. Instead, the signals are fed into superconducting quantum interference devices (SQUIDs), which are the basis for a growing family of electronic devices that operate by superconductivity. In this case, the TES is transformer coupled to the SQUID by an input coil. A current-biased shunt resistor is used to provide a constant voltage bias to the TES. When the shunt resistor is operated close to the detector temperature, a negligible Johnson noise from the bias network is given. The SQUID readout has a number of advantages including: it operates near the bolometer temperature, has very low power dissipation and large noise margin, and low sensitivity to microphonic pickup. In addition, the fabrication and lithographic processes used in both SQUID readouts and TES bolometers are similar what helps in their integration on the same chip.

Figure 61 shows the typical TES circuit wired in series with the coil of a SQUID amplifier. The voltage bias is achieved by current bias of the cold shunt resistor  $R_{sh}$  whose about 10 mW resistance is much smaller than the  $R \approx 1$  resistance of the TES. The current through the TES is measured with a SQUID ammeter, and the in-band reactance of

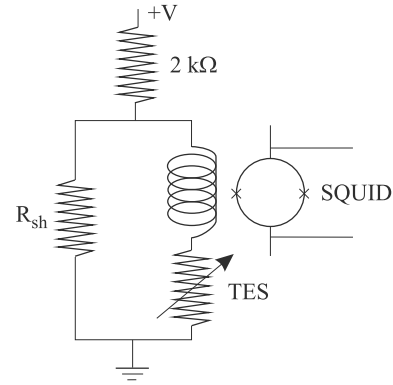


Fig. 61. Typical TES bias circuit and low noise, low power SQUID.

the SQUID input is much less than  $R$ . When the bias to a SQUID is turned off, the whole device goes into a superconducting state where it adds no noise. Thus, by switching on or off rows or columns of SQUIDs in an array (one for each pixel) a cold multiplexer may be realized. The biases across the SQUIDs are controlled by the address lines. Each SQUID can be switched from an operational state to a superconducting one if it is biased to carry about 100  $\mu$ A. The address lines are set so all the SQUIDs in series are superconducting except one, and then only that one contributes to the output voltage. By a suitable series of bias settings, each SQUID amplifier can be read out in turn. To avoid very large numbers of leads leaving the cryostat, lines of 30–50 detectors can be multiplexed before amplification.

In general, SQUID-base multiplexers developed for TES bolometers and microcalorimeters used both time-division [243] and frequency division [244] approaches. We have described the time-division approach, where multiplexer uses a SQUID for each bolometer to switch the outputs sequentially through a single SQUID amplifier. In the case of frequency domain case, each TES is biased with a sinusoidally varying voltage and the signals from a number of TESs are encoded in amplitude-modulated carrier signals by summing them. The signals are then amplified by a single SQUID and recovered with ambient temperature lock-in amplifiers. For more SQUID multiplexer details, see e.g., Refs. 245–249.

The most ambitious example of TES bolometer array is that used in the submillimeter camera – submillimetre common-user bolometer array (SCUBA -2) with 10,240 pixels [238,250]. The camera operated at wavelengths of 450 and 850  $\mu$ m has been mounted on the James Clerk Maxwell Telescope in Hawaii. Each SCUBA-2 array is made of four side-butable sub-arrays, each with 1280 (32×40) transition-edge sensors. The design is illustrated in Fig. 62 together with cross-section of the detector architecture. The detector technology is based on silicon micromachining. Each pixel consists of two silicon wafers bonded together. The upper wafer with its square wells supports the silicon nitride membrane on which Mo-Cu bi-layer TES detectors and the absorbing silicon brick are suspended. The lower wafer is thinned to 1/4 wavelength in silicon (70  $\mu$ m at 850



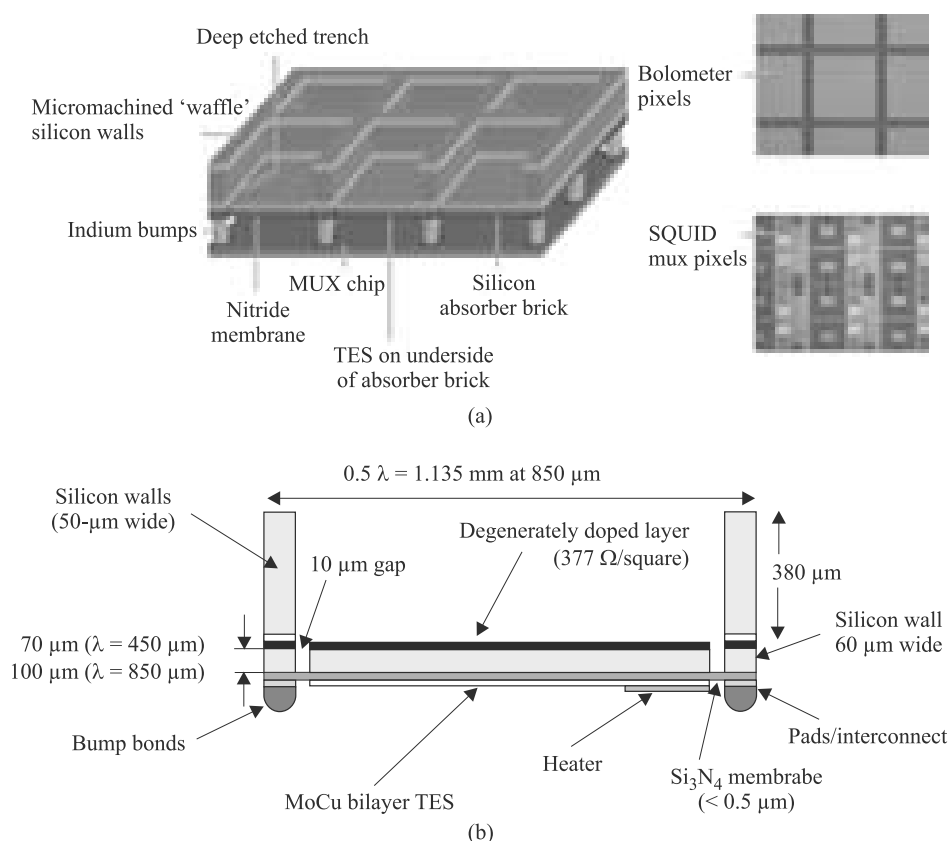


Fig. 62. SCUBA-2 bolometer array: (a) design features and (b) cross-section of single pixel (after Ref. 238).

$\mu\text{m}$ ). The upper surface of this wafer has been previously implanted with phosphorus to match the impedance of free space ( $377 \Omega/\text{square}$ ). The detector elements are separated from their heat sinks by a deep etched trench that is bridged by only a thin silicon nitride membrane. The superconducting electronics that read out the bolometers are fabricated on separate wafers (see Fig. 63). The two components are assembled into an array using indium bump bonding. Further details are in Walton *et al.* [238] and Woodcraft *et al.* [251].

In addition to the arrays for SCUBA-2, various forms of TES-based bolometers with SQUID readouts are under active development [49,253]. Large format arrays of antenna-coupled TES bolometers are very attractive candidates for a cosmic microwave background polarization mis-

sion. Broadband antennas with RF diplexing and/or interleaved antennas can make efficient use of the focal plane. Antennas are inherently polarization sensitive, and the excellent gain stability provided by the feedback in TES bolometers facilitates polarization differencing.

The fabrication technologies used for TES bolometers are very flexible and specialized detectors are being developed to meet the needs of specific observations. A bolometer design allows the production of large monolithic detector arrays with a very high fill factor by standard planar lithography. Figure 64 shows the 1024-pixel array structure together with a single pixel [254]. The absorbing element is a square mesh of  $1\text{-}\mu\text{m}$ -thick low-stress (non-stoichiometric) silicon nitride (LSN), which is metallized with gold to produce an average sheet resistance of  $377 \Omega/\text{square}$ .

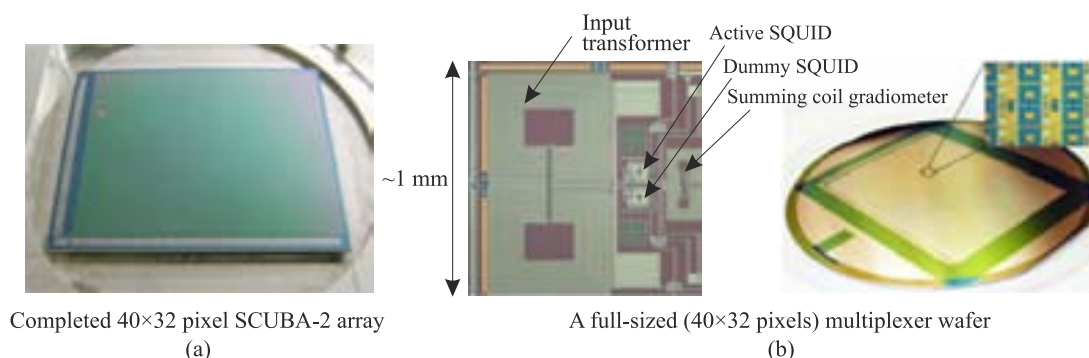


Fig. 63. SCUBA-2: (a) bolometer array and (b) SQUID multiplexer pixel (after Ref. 252).

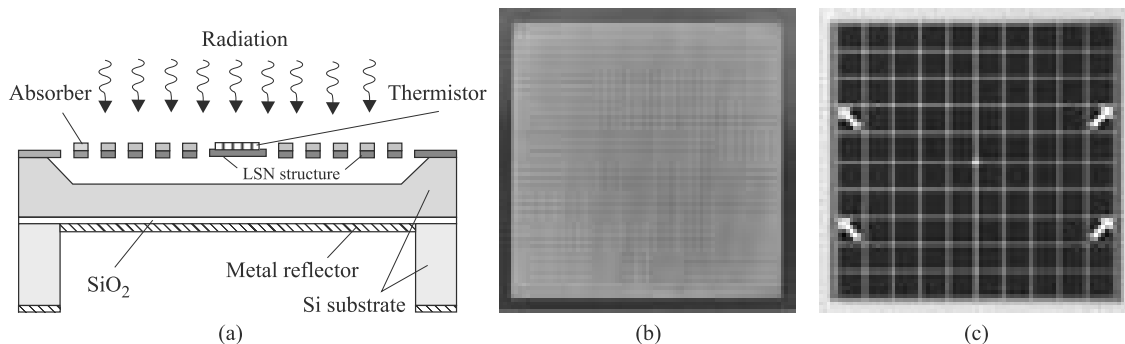


Fig. 64. Monolithic superconducting bolometer array: (a) cross section of pixel, (b) silicon nitride structure for a 1024 element array of bolometers (1.5×1.5 mm<sup>2</sup> pixel size), and (c) complete pixel including sensor and metallization (after Ref. 254).

A conducting backshort is located at the distance  $\lambda/4$  behind the mesh. This mesh absorber is supported at four points [shown by arrows in Fig. 64(c)] by low thermal conductivity beams of LSN. To produce  $T_c \approx 400$  mK, a proximity-effect sandwich of Al and Ti is made at the centre of the mesh. To connect the thermistors to the edges of the array, fully superconducting Nb leads are used by a way of the beams and the dividing strips between pixels. Other designs it is using micromachining and folding to bring the leads out of the third dimension [255].

Figure 65 shows a close-packed horn-coupled array with radial support legs. The bolometers which are located at the small ends of the horns, are then separated sufficiently for easy support and wiring. The array is complete fully lithographed [256].

## 15. Field effect transistor detectors

Nonlinear properties of plasma wave excitations (the electron density waves) in nanoscale FET channels enable their response at frequencies appreciably higher than the device cut-off frequency, what is due to electron ballistic transport. In the ballistic regime of operation, the momentum relaxation time is

longer than the electron transit time. The FETs can be used both for resonant (tuned to a certain wavelength) and non-resonant (broadband) THz detection and can be directly tuneable by changing the gate voltage [257–262].

The transistor receivers operate in wide temperature range up to room temperatures [263,264]. Different material systems are used in fabrication of FET, HEMT, and MOSFET devices including: Si, GaAs/AlGaAs, InGaP/ InGaAs/GaAs, and GaN/AlGaAs [262–268]. Plasma oscillations can be also observed in a two-dimensional (2D) electron channel with a reverse-biased Schottky junction [269] and double quantum well FET with a periodic grating gate [270].

The use of FETs as detectors of THz radiation was first proposed by Dyakonov and Shur in 1993 on the basis of formal analogy between the equations of the electron transport in a gated two-dimensional transistor channel and those of shallow water, or acoustic waves in music instruments [271]. As a consequence, hydrodynamic-like phenomena should exist also in the carrier dynamics in the channel. Instability of this flow in the form of plasma waves was predicted under certain boundary conditions.

The physical mechanism supporting the development of stable oscillations lies in the reflection of plasma waves at the borders of transistor with subsequent amplification of the wave's amplitude. Plasma excitations in FETs with sufficiently high electron mobility can be used for emission as well as detection of THz radiation [272,273].

The detection by FETs is due to nonlinear properties of the transistor, which lead to the rectification of the ac current induced by the coming radiation. As a result, a photo-response appears in the form of a dc voltage between source and drain. This voltage is proportional to the radiation intensity (photovoltaic effect). Even in the absence of an antenna, the THz radiation is coupled to the FET by contact pads and bonding wires. A big progress in sensitivity can be obtained by adding a proper antenna or a cavity coupling.

The plasma waves in FET is characterized by linear dispersion law [271], and in gated region

$$p = sk = k \frac{q(V_g - V_{th})}{m}^{1/2}, \quad (24)$$

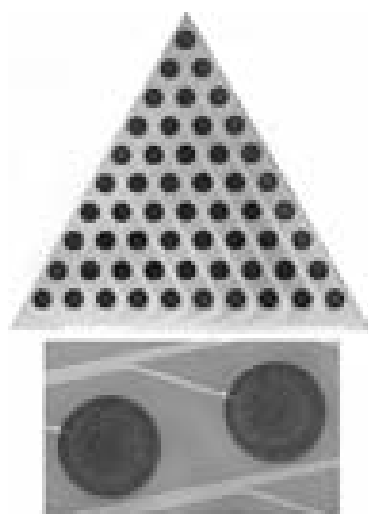


Fig. 65. Array of 55 TES spiderweb bolometers and closeup of bolometers. Six wedges of the type shown are assembled to form a 330-element hexagonal horn-coupled array (after Ref 12).

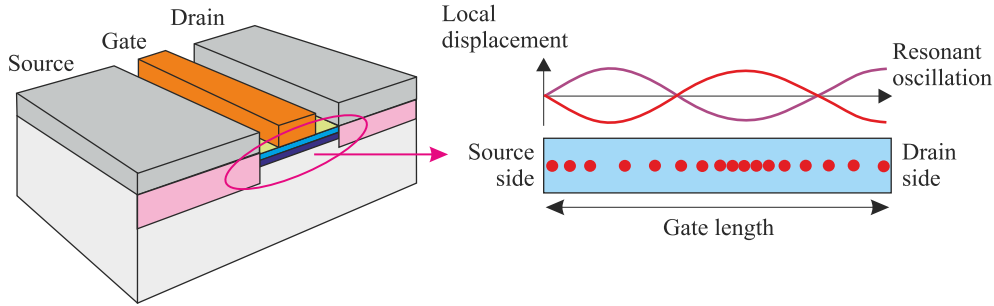


Fig. 66. Plasma oscillations in a field effect transistor.

where  $s \approx 10^8$  cm/s is the plasma wave velocity in GaAs channel,  $V_g$  is the gate voltage,  $V_{th}$  is the threshold voltage,  $k$  is the wave vector,  $q$  is the electron charge, and  $m^*$  is the electron effective mass. Figure 66 schematically shows the resonant oscillation of plasma waves in gated region of FET.

The dispersion relations in bulk (3D) and ungated regions of FET differ from Eq. (24) and are equal to

$$p = \frac{q^2 N}{\epsilon m}^{1/2} \quad \text{and} \quad p = \frac{q^2 n_s}{2\epsilon m} k^{1/2}, \quad (25)$$

respectively. Here  $N$  is the bulk electron concentration for alloyed regions and  $n_s$  is the sheet electron density for channel regions.

The plasma wave velocity in gated region is typically noticeably larger compared the electron drift velocity. A short FET channel with length  $L_g$  acts as a resonant cavity for these waves with the eigen frequencies  $\omega_n = \omega_0(1 + 2n)$  ( $n = 1, 2, 3, \dots$ ). The fundamental plasma frequency is

$$\omega_0 = \frac{q(V_g - V_{th})}{2L_g m}^{1/2}. \quad (26)$$

When  $\omega_0 \tau \ll 1$ , where  $\tau$  is the momentum relaxation time, the detector response is a smooth function of  $\omega$  and  $V_g$  (broadband detector). When  $\omega_0 \tau \gg 1$ , the FET can operate as a resonant detector with tuneable by the gate voltage response frequency, and this device can operate in the THz range. The detection character (resonant or nonresonant) depends on the quality factor of the transistor resonating cavity.

Assuming  $m^* \approx 0.1m_0$  ( $m_0$  is free electron mass),  $L_g \approx 100$  nm, and  $V_g - V_{th} \approx 1$  V, the frequency of plasma waves is estimated as  $\nu_0 = \omega_0/2 \approx 3$  THz. The minimum gate length can approach  $\approx 30$  nm, and thus,  $\nu_0$  can reach 12–14 THz for FETs with GaAs channels.

The plasma wave velocity  $s$  may be presented in another manner. When the thickness of the dielectric layer between the channel and the gate is small compared to the wavelength of plasma waves, it is equal to  $s = (n_s q^2 d / \epsilon m^*)^{1/2}$  [274], where  $\epsilon$  is the permittivity of the dielectric layer and  $d$  is the distance from gate to channel. Then, the fundamental frequency can be expressed by the relation

$$\nu_0 = \frac{s}{4L_g} = \frac{1}{4L_g} \sqrt{\frac{n_s q^2 d}{\epsilon m}}, \quad (27)$$

in which there are no free parameters and from which the locations of the resonant peaks can be to a certain degree predicted, though a discrepancy between the peaks frequencies predicted and those experimentally found at  $T = 4$  K in GaAs/AlGaAs modulation doped single QW were observed [275].

In a simple approximation, the electron concentration  $n_s$  is described by a plane capacitor formula:  $n_s = CV_g/q$ . Here,  $C$  is the capacitance between the gate and channel (per unit surface area) and  $V_o = (V_g - I_{ds}R_s - V_{th})$  is the difference between the gate voltage  $V_g$ , the voltage drop across the contact resistance  $R_s$  ( $I_{ds}$  is the current in the transistor channel), and the threshold voltage  $V_{th}$  of the transistor. In this case, the velocity of plasma waves is defined by the following expression

$$s = \frac{q(V_g - I_{ds}R_s - V_{th})}{m}^{1/2}. \quad (28)$$

The resonance frequency of plasma oscillations in the subgate 2D electron gas is governed by the gate length  $L_g$  and the plasma-wave velocity  $s$ , and is similar to Eq. (26)

$$\nu_r = \frac{1}{4L_g} \frac{q(V_g - I_{ds}R_s - V_{th})}{m}^{1/2}. \quad (29)$$

The resonance frequency is maximal for zero bias at the gate and tend to zero when  $V_{gs} = V_{th}$ . For 2D electron gas in GaN/AlGaN with the gate length  $L_g = 250$  nm at  $T = 4.2$  K, the resonance frequency  $\nu_r = 576$  GHz (the quality factor  $Q_r = 1.81$ ) [266].

Figure 67 shows the characteristics of 60-nm gate length InGaAs/InAlAs transistor [276]. The photoresponse of the device exposed to the radiation of 2.5 THz frequency as function of the gate voltage, measured at various temperatures, is shown in Fig. 67(a). At  $T > 100$  K, only non-resonant detection was observed as a broadband peak. With temperature decreasing below 80 K, the additional peak appears as a shoulder on the temperature-independent background of the non-resonant detection. This behaviour can be attributed to the resonant detection of THz radiation by plasma

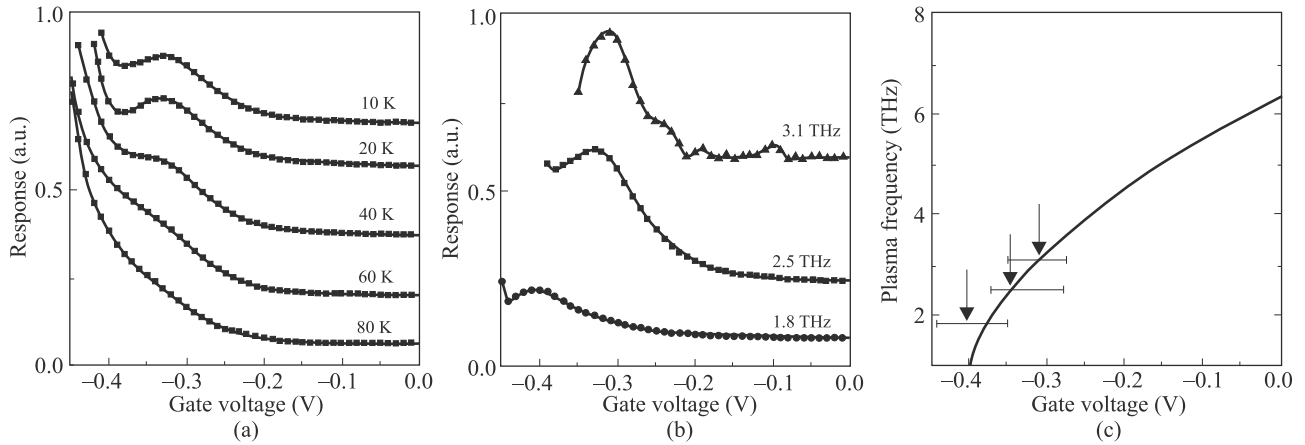


Fig. 67. Characteristics of 60-nm gate length InGaAs/InAlAs transistor: (a) response at 2.5-THz frequency as a function of the gate voltage at different temperatures (80 K down to 10 K), (b) response at 10 K as a function of the gate voltage at different frequencies (1.8, 2.5, and 3.1 THz), (c) position (indicated by arrows) of resonance maxima as a function of gate voltage. The calculated plasmon frequency as a function of the gate voltage, using Eq. (25) for  $V_{th} = .041$  V, is shown by the solid line. The error bars correspond to the line width of the measured plasmon resonance peaks (after Ref. 276).

waves. To support this assumption, additional measurements were carried out at 10 K for excitation frequencies of 1.8, 2.5, and 3.1 THz. The experimental results are displayed in Fig. 67(b). For comparison, the theoretical prediction of plasma frequency as a function of gate voltage according to Eq. (25) is plotted as a continuous line in Fig. 67(c). One can see that the increasing excitation frequency from 1.8 to 3.1 THz causes moving of the plasmon resonance with the gate voltage, roughly in agreement with the theory.

Veksler *et al.* have predicted that applying a drain-to-source current it is possible to observe room temperature THz radiation resonant detection [277]. It appears, that driving a transistor into the saturation region enhances the non-resonant detection and can lead to the resonant detection even if the condition  $\omega\tau \gg 1$  is not satisfied [264,266]. The physical reason is that the effective decay rate for plasma oscillations, in the condition of hot drifting electrons, becomes equal to  $1/\tau_{eff} = 1/\tau - 2v/L_g$ , where  $v$  is the electron drift velocity, and becomes longer when applying current. As  $\tau_{eff}$  becomes of the order of unity, the detection becomes resonant.

Tauk *et al.* have studied Si MOSFETs with 20–300-nm gate lengths at room temperature and the frequency  $\nu = 0.7$  THz [265]. It was found that response depends on the gate length and the gate bias. The responsivity value of 200 V/W and  $NEP = 10^{-10}$  W/Hz<sup>1/2</sup> (see Fig. 68, Ref. 261) that is comparable to the best current commercial room temperature THz detectors. The inset of Fig. 68 shows the detection signal for transistors with different gate lengths. One can see that the detected signal decreases when the gate length is reduced from 300 nm to 120 nm.

An important progress has been reported recently – a 3×5 Si MOSFET FPA processed by a 0.25-μm CMOS technology [278]. Each pixel of the array consists of a 645-GHz patch antenna coupled to a FET detector and a

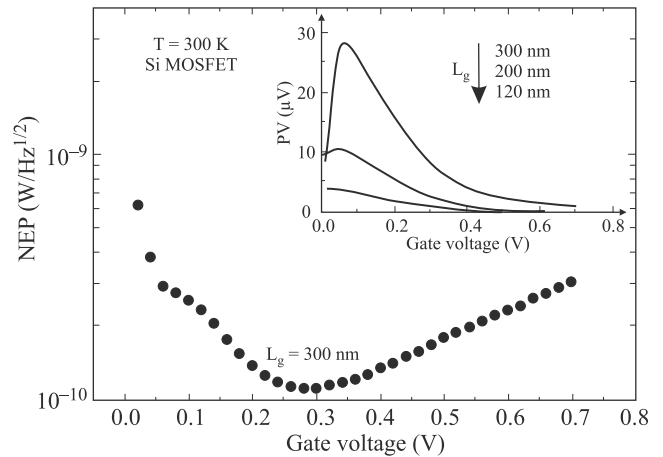


Fig. 68.  $NEP$  as a function of the gate voltage for Si MOSFETs with a 300 nm gate length,  $T = 300$  K. The inset shows the detection signal as a function of the gate length (after Ref. 261).

43-dB voltage amplifier with a 1.6-MHz bandwidth. The  $NEP$  value of  $3 \times 10^{-10}$  W/Hz<sup>1/2</sup> was achieved that paves the way for the realization of broad-band THz detectors and FPAs for high frame-rate imaging on the basis of CMOS technology. The performance of these fast detectors at room temperature is of the order of other uncooled detectors in THz radiation frequency range (see Table 3) with the advantage of a low-cost and a multi-pixel integration capability offered by the CMOS technology. Using modern electronic technology, FET detectors can be easily integrated to make THz FPAs.

The first integrated a 600 GHz CMOS FPAs have been demonstrated that operate FETs well beyond their 35 GHz cutoff frequency [278,279]. It was shown that the low-frequency operation of a non-biased source-drain FET power-detection circuit can be extended to frequencies above the device cut-off frequency by the use of distributed resistive self-mixing.



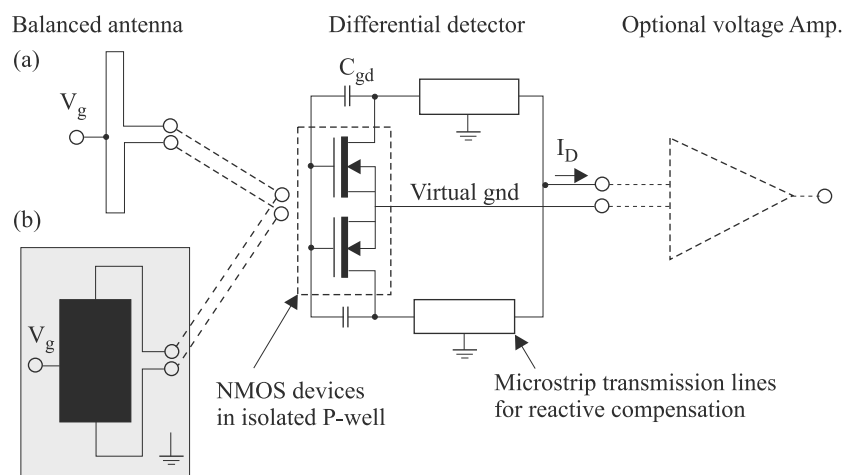


Fig. 69. Schematic diagram of one pixel of the designed 650 GHz array with integrated folded dipole antenna (a) and differential patch antenna (b). Pixels with an optical voltage amplifier have also been realized (after Ref. 278).

Square-law power detection remains as one possible operating principle for terahertz focal-plane imaging array. Figure 69 shows a schematic of a single pixel. The detector circuit is designed with two  $0.78 \times 0.25 \mu\text{m}^2$  large NMOS transistors in a differential configuration. The metal-insulator-metal capacitors  $C_{gd}$  are used to tie drain terminal of each transistor to the same signal voltage as the gate. Microstrip transmission lines are used to detect currents of the two devices combined at another virtual ground. The length of these 50 transmission lines is selected to create a shunt inductance from each drain to ground, which tunes out the capacitive part of the detector input impedance at the operating frequency.

A version of a  $3 \times 5$  pixel CMOS FPA implemented in a  $0.25\text{-}\mu\text{m}$  NMOS technology and equipped with  $0.65\text{ THz}$  on-chip patch antennas is presented in Fig. 70. Each pixel achieved a responsivity of  $80\text{ kV/W}$  and a  $NEP$  of  $300\text{ pW/Hz}^{1/2}$ , which is comparable with conventional detectors of THz radiation (see Table 11). However, in contrast to bolometers, the presented detectors can be integrated with the readout electronics and implemented in a standard CMOS process technology.

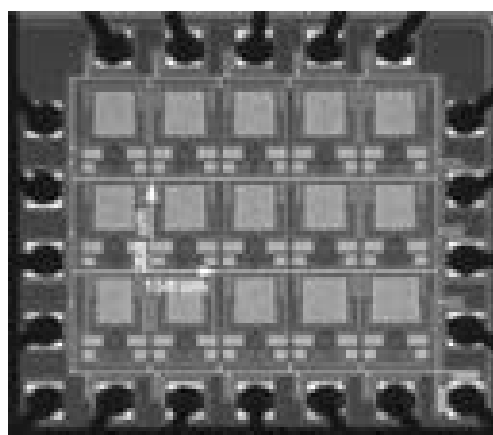


Fig. 70. Micrograph of a wire-bonded  $3 \times 5$ -pixel  $0.65\text{-THz}$  CMOS FPA. The third row contains pixels with the centre frequency of the antennas stepwise tuned from  $550\text{ GHz}$  to  $750\text{ GHz}$ . The die size is  $0.85 \times 0.90\text{ mm}^2$  (after Ref. 279).

Hitherto, the signal current levels in FET channels compared to dark (noise) current levels in biased source-drain channels are still relatively small which requires to use, e.g., the lock-in amplifiers with a narrow bandwidth to suppress

Table 11. Comparison of non-cooled terahertz direct detector technologies (after Ref. 279).

| Frequency (THz) | Technology ( $\mu\text{m}$ ) | Voltage sensitivity (kV/W) | $NEP$ ( $\text{pW/Hz}^{1/2}$ ) | Pixels           | Monolithic integration |
|-----------------|------------------------------|----------------------------|--------------------------------|------------------|------------------------|
| $0.65^a$        | 0.25 CMOS                    | 80                         | 300                            | $5 \times 3$     | Yes                    |
| $0.60^b$        | 0.25 CMOS                    | 50                         | 400                            | $5 \times 3$     | Yes                    |
| 0.2–30          | Golay cell                   | 0.1–45                     | 200–400                        | –                | No                     |
| 0.094           | Ni microbolometer            | 0.017                      | 19                             | $8 \times 8$     | Yes                    |
| 4.3             | $\text{VO}_x$ microbolometer | 4.97                       | 100–300                        | $128 \times 128$ | Yes                    |
| 0.80            | SBD                          | 0.4                        | 20                             | –                | No                     |
| 0.1–30          | Pyroelectric                 | 150                        | 400                            | –                | No                     |
| 0.2–30          | Bolometer                    |                            | 3                              | –                | No                     |

<sup>a</sup>Bandwidth of  $45\text{ GHz}$  (patch antenna)

<sup>b</sup>Bandwidth of  $125\text{ GHz}$  (dipole antenna)

the noise in every channel. This is one of the reasons why this kind of facility (for the matrix array presented in Fig. 68 five lock-in amplifiers were used for 5 channels) cannot be exploited for real-time imaging, and one needs to design special circuits with rather wide bandwidth to realize FET detector arrays for real time imaging.

## 16. Novel THz detectors

In comparison to the technical mature of other frequency regions, in the THz region, detectors have not been fully established due to mainly two reasons:

- frequency of the THz wave is too high to be handled with existing high-frequency semiconductor technology,
- photon energy of the THz wave is much lower than the band gap energy of semiconductors.

It is expected that applications of nanoscale materials and devices will open the door to overcome such difficulties. Today, research activities in the field of THz radiation detectors focus also on the development of novel nanoelectronic materials and technologies. Here, we give several examples of new solutions.

Carbon nanotubes (CNT) are the hottest topic in physics and microelectronics. From the material point of view, carbon nanotubes offer an excellent alternative to their solid-state counterparts because of their small junction areas due to their physical dimensions (<1 to 2 nm diameter), high electron mobilities (up to 200 000 cm<sup>2</sup>/Vs, and low estimated capacitances (tens of aF/μm), leading to predicted cutoff frequencies in the THz range. Figure 71 shows predictions of the maximum frequency for nanotube transistors vs. gate length, and compared to other technologies. In the estimations, the largest transconductance,  $g_m = 20 \mu\text{S}$ , has been assumed.

Recent progress in fabricating graphene layer structures with long momentum relaxation time of electrons and holes promises a significant enhancement of the performance of future graphene optoelectronic devices [282]. Recently, Ryzhii *et al.* have proposed to utilize multiple graphene layer structures with lateral p-i-n junctions for THz detection [283]. It was predicted that these structures can exhibit high responsivity and detectivity in the terahertz region at room temperatures. Due to relatively high quantum efficiency and low thermal generation rate, the photodetectors can substantially surpass other THz detectors.

The carbon nanotube with unique one-dimensional structure has attracted much attention and has been extensively studied for future nano-electronics, nano-photonics and nano-mechanics [284]. A sensitive and frequency tuneable terahertz detector based on a carbon nanotube quantum dot (QD) transistor has been also demonstrated (see Fig. 72) [285]. Photon-assisted tunnelling (PAT) is a process that can be used in THz photodetectors. Figure 72(c) presents a schematic diagram of electron tunnelling processes in a QD in the presence of an electromagnetic wave. Energy states in the QD can be tuned by changing the electrostatic potential

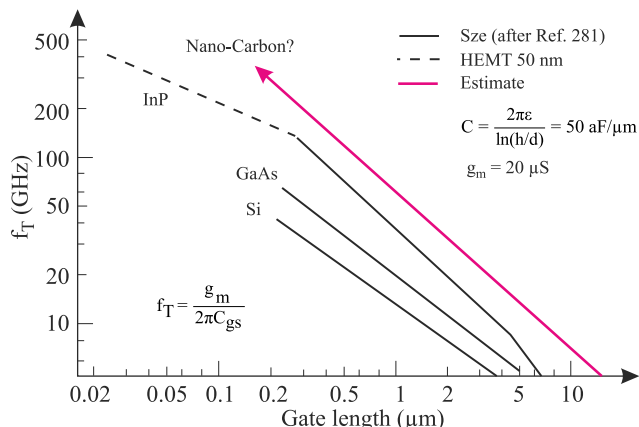


Fig. 71. Predictions of the maximum frequencies vs. gate length for nanotube transistors as compared with other technologies (after Ref. 280).

with application of a gate voltage. When the Fermi level in the source lead aligns with a level in the QD [see middle panel of (c)], a source-drain current flows via elastic tunnelling. When electrons exchange photons, a new current is generated via inelastic tunnelling, i.e., photon-assisted tunnelling (see left and right panels).

These experimental results provide evidence for photon-assisted tunnelling in the THz region and the peak position of the satellite currents varies linearly with the THz photon energy (see Fig. 73). It was thus demonstrated that the carbon nanotube quantum dot works as a THz detector with frequency tunability by changing the gate voltage.

Although the frequency-selective THz detection has been achieved, the detection sensitivity was not high. It is due to detection mechanism, where one-photon absorption generates only one electron even if quantum efficiency of 100% is assumed. To resolve this problem, a carbon nanotube (CNT) single-electron transistor (SET) integrated with a GaAs/AlGaAs heterostructure chip having a two-dimensional electron gas (2DEG) has been proposed [286]. In this hybrid structure, THz absorption takes place in the 2DEG but signal readout in the CNT-SET (see Fig. 74). The operation principle of this device is that the CNT transistor senses electrical polarization induced by terahertz-excited electron-hole pairs in the 2DEG. The CNT-SET has the source drain electrodes with an interval of about 600 nm and the side-gate electrode was operated at 2.5 K. The noise equivalent power of this detector is estimated to be  $10^{-18}$ – $10^{-19}$  W/Hz<sup>1/2</sup>.

It was also shown that nanotubes can be used as bolometers up to the frequencies  $\approx 2.5$  THz [287] as well as the nanoantenna [288,289].

Among a variety of novel THz detection schemes [25, 26,87,290–292], only semiconductor quantum devices have demonstrated to produce clear single-photon signal against incident THz photons. Komiyama has described analyzed two types of detectors [26]:

- quantum dot (QD) detector, where a QD is electrically polarized by photoexcitation and the induced polariza-

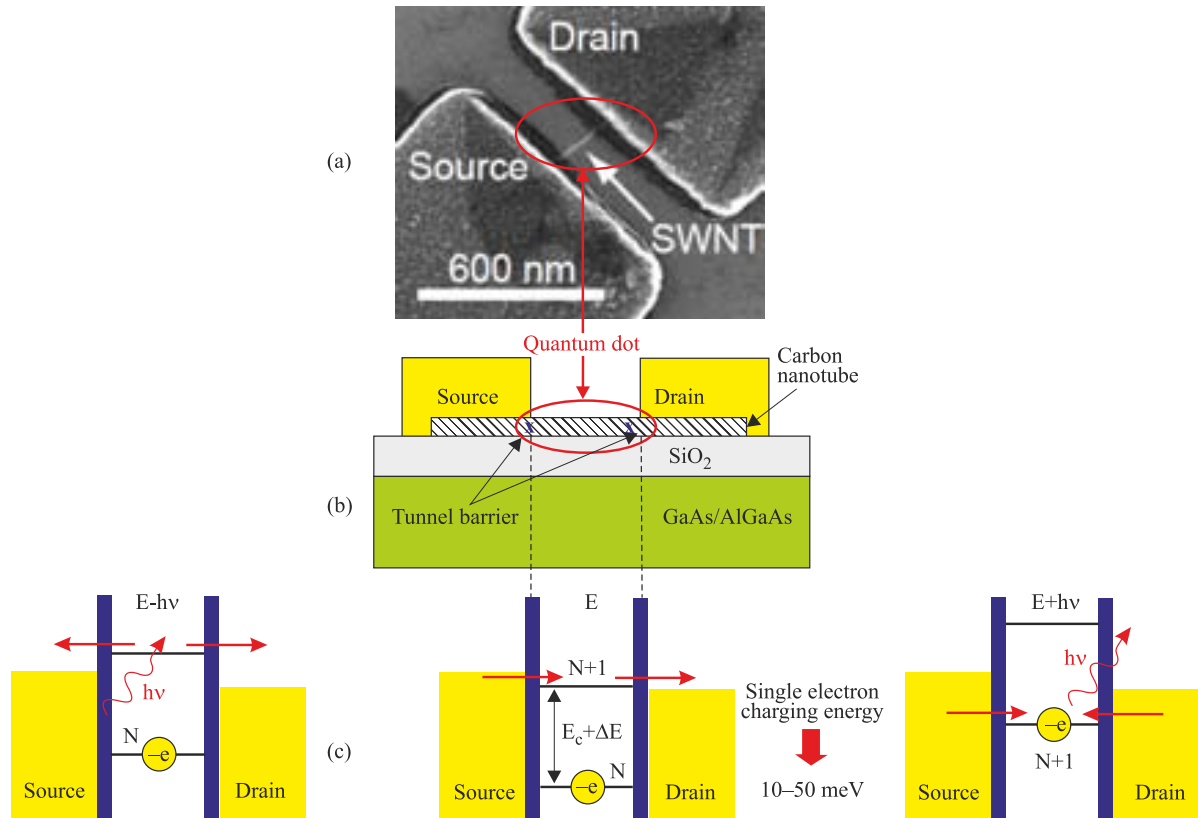


Fig. 72. Terahertz detector based on a carbon nanotube quantum dot transistor: (a) device's photograph, (b) device structure, and (c) schematic diagram of electron tunnelling processes in a QD in the presence of an electromagnetic wave. When the Fermi level in the source lead aligns with a level in the QD [see middle panel of (c)], a source-drain current flows via elastic tunnelling. When electrons exchange photons, a new current is generated via inelastic tunnelling, i.e., photon-assisted tunnelling (see left and right panels) (after Ref. 285).

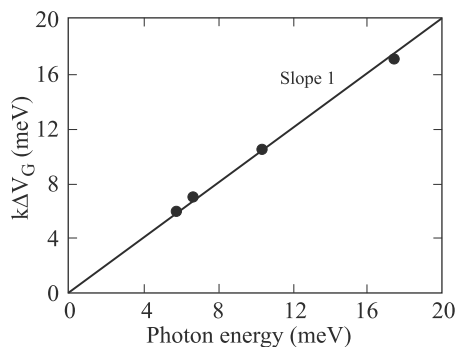


Fig. 73. Carbon nanotube quantum dot device: the energy spacing between the original and satellite peaks as a function of the photon energy of the terahertz wave measured at temperature 1.5 K (after Ref. 285).

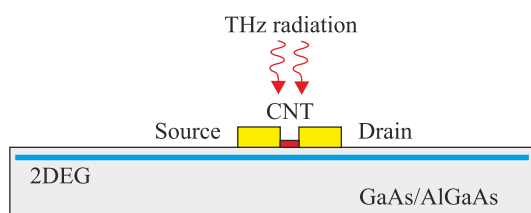


Fig. 74. Schematic representation of the CNT/2DEG terahertz detector (after Ref. 286).

tion is sensed by a nearby single-electron transistor (SET), and

- charge-sensitive IR phototransistor (CSIP) in which an isolated quantum well (QW) island is charged up by photoexcitation and the induced charge is detected by a conducting channel of 2-D electron gas (2DEG).

In conventional photoconductor [see Fig. 75(a)], an electron is excited by one photon, next it is carried to the drain, and usually the photoconductivity gain is below 1. Several of THz single-photon detectors described by Komiyama adopt a different detection scheme. As is shown in Fig. 75(b), a photon absorbed by an isolated small semiconductor island creates an electron which next tunnels out of the island. Losing one electron, the island is positively charged – referred as a “hole”. The excited electron outside the island is separated from the hole by a potential barrier and as a result – yields the long recombination time  $\tau_{life}$  of the excited electron-hole pair. A charge-sensitive device is placed nearby the island to detect the charging-up of the island.

Historically, a single QD has been first developed [25,286–288]. The detector shown in Fig. 74 is fabricated in GaAs/AlGaAs single heterostructure crystals and utilizes cyclotron resonance excitation in magnetic field. The metal gates forming a SET [Fig 76(a)] extend to the opposite directions. A bowtie antenna [Fig 76(b)] couples incident radiation to the QD.

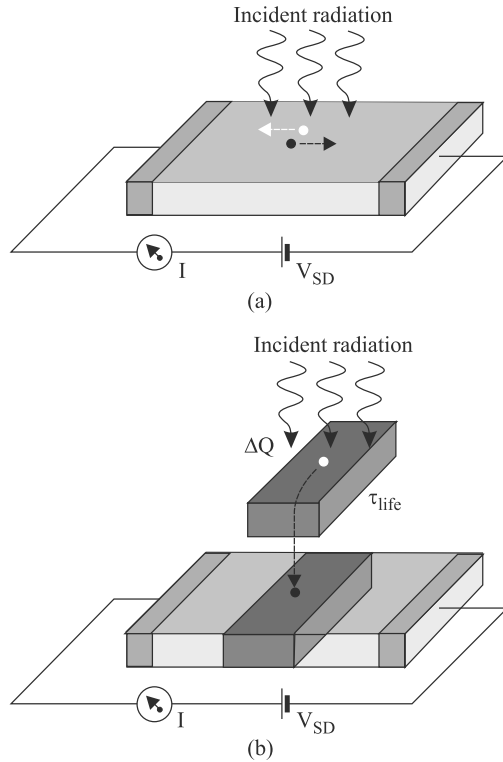


Fig. 75. Schematic representation of the detection mechanism: (a) conventional scheme and (b) novel scheme (adapted after Ref. 26).

The most straightforward realization of the QD detector is a double QD (DQD) single-photon detector implemented in a GaAs/AlGaAs heterostructure crystal [290]. Figure 77 shows an example of DQD detector, where metal gates [cross gate (CG), barrier gate (BG), FG, and antenna] are deposited on top of the crystal surface. About 100 nm below the crystal surface, a heterointerface with a high-mobility 10-nm thick 2DEG layer, with electron sheet density of  $3 \times 10^{11} \text{ cm}^{-2}$ , is located. By negatively biasing the gates, the 2DEG is depleted from the regions below the gates, forming an SET (QD1) coupled with QD2. Two electrodes define QD2 and form a planar dipole antenna to couple incident radiation with QD2. The radiation is absorbed by plasma resonance mechanism in which collective oscillation of electrons in the confining potential of QD2 is excited.

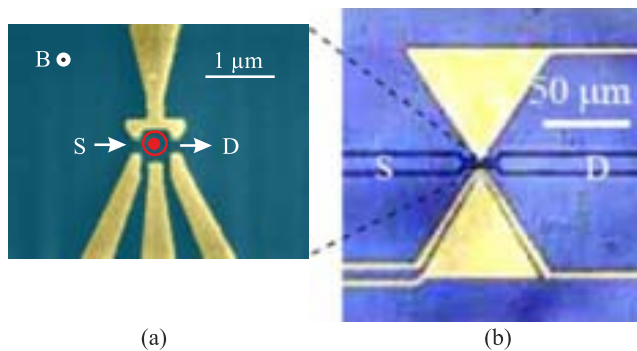


Fig. 76. Single quantum dot THz detector: (a) closed-up top view and (b) bird view (after Ref. 26).

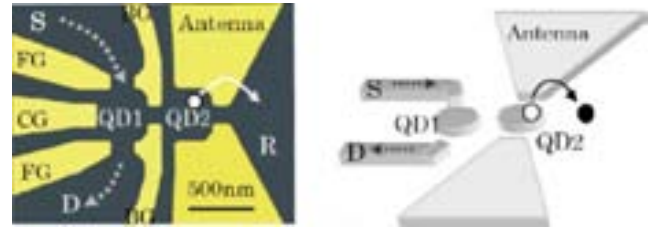


Fig. 77. Double QD single-photon detector: (a) top view and (b) schematic representation including antennas (after Ref. 26).

The outstanding sensitivity is the distinct advantage of QD detectors. However, the application of these detectors is restricted because of ultralow temperature operation (below 1 K) and sophisticated fabrication technique. It appears also that the spectral range of detection is limited to relatively long wavelengths due to excitation mechanism relying on plasma resonance and magneto-plasma resonance. An attractive solution alternative is the photosensitive field-effect transition fabricated in a double-quantum well (DQW) structure, called a CISP [87,293,294].

Figure 78 demonstrates operation of the CISP detector. The photoexcited electrons generated via intersubband transition in the upper quantum well (QW) escape out of upper QW through the tunnel barrier, and relax into the lower QW. Upper QW is electrically isolated from the lower QW by negatively biasing the surface metal gates and then the isolated upper QW is positively charged up due to photoexcitation. The gathered positive charge in the isolated upper QW is detected by an increase in conductance through the lower QW, what is shown in Fig. 78(b). Summarizing, the CISP detector operates as a photosensitive FET with a photoactive floating gate served by the upper QW.

The detection sensitivity demonstrated by the quantum dot and CISP detectors is more than order of magnitude superior to any other detectors at low background conditions (see Fig. 20). In addition, remarkable signal amplitude is a consequence of large current responsivity or the large photoconductive gain. Their low output impedance (about 200 k for QD detectors and 0.1–10 k for CISPs) makes them unique detectors [87]. Small submicrometer CSIPs are promising for integration to large-scale arrays.

A new approach demonstrating possibilities of modern semiconductor nanotechnology to fabricate compact THz detector has been presented by Seliuta *et al.* [295,296]. This device is an example of a combination of nanostructure physics (GaAs/AlGaAs modulation doped structure) and antennae approach and relies on the non-uniform two-dimensional electron gas heating in external high frequency fields. Figure 79 shows the voltage sensitivity of this structure as a function of frequency. The detector exhibits broad detection bandwidth ranging from microwaves up to terahertz frequencies (between 10 GHz and 0.8 THz) with nearly constant voltage sensitivity of around 0.3 V/W.

Detection in THz region has been recently demonstrated using quantum rings (QRs) [297,298]. Quantum rings are derived from epitaxially grown self-organized QDs by post



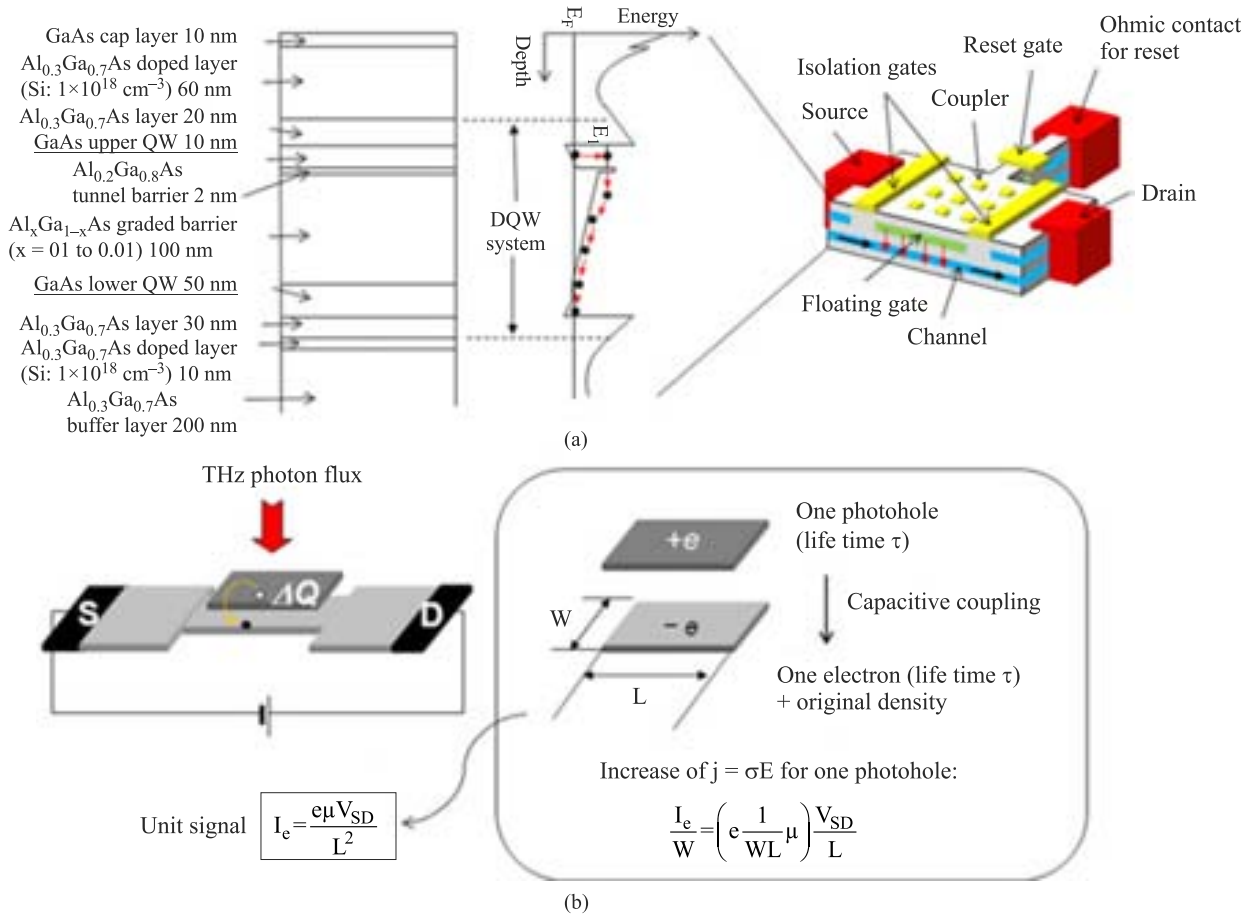


Fig. 78. CISP detector: (a) schematic representation of crystal structure (left), the energy diagram (centre), and device structure (right) and (b) CISP as a photoactive FET (left) (after Ref. 87).

growth annealing. Confinement in these nanostructures is stronger than that in dots because of the altered shape. It is found that the quantum ring intersublevel detectors

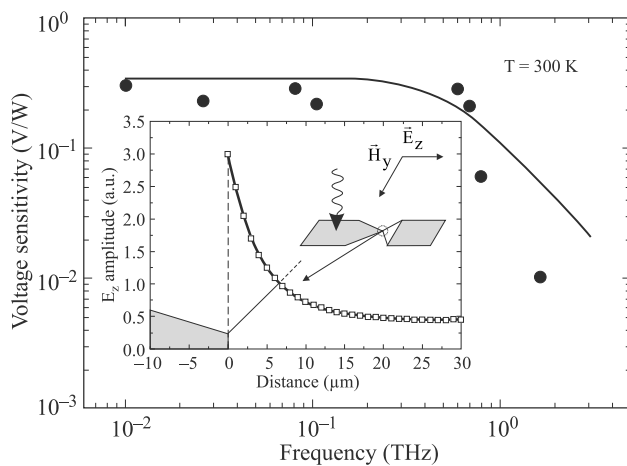


Fig. 79. Voltage sensitivity as a function of frequency for the two-dimensional electron gas bow-tie diode. Dark circles denote experimental data, solid line shows the fit using a phenomenological approach. Insert: distribution of the amplitude of electric field in the active part of the diode exposed to radiation of 0.75 THz. The background of the insert is decorated schematically as the shape of the device (after Ref. 296).

(QRIDs) exhibit very low dark current and strong response in the 1–3 THz range, with the peak response measured at 1.82 THz (165  $\mu\text{m}$ ) in the temperature range of 5–10 K. This detection peak is characterized by a peak responsivity of 25 A/W and specific detectivity of  $1 \times 10^{16}$  Jones [298].

THz detector response can be enhanced by surface plasmon effects [299–301]. When the energy of the plasma-wave frequencies is quantized, the quanta are called plasmons. Two key factors are important:

- matching the size and shape of the metal pattern so the desired wavelength will generate plasmons,
- coupling of the plasmons to the detector.

The generation of plasmons depends significantly on the metallic pattern. Dimensions of metal grating should be similar to the metal strip width to permit the plasmon fields to enter the detector below the grating. Usually, a thin dielectric layer is placed over the detector and a metal grid is placed on top of the dielectric layer. As the plasmons are travelling parallel to the surface, a large optical path can be obtained for absorption without requiring a thick absorbing layer.

As it is explained in Sect. 15, the channel of a FET can act as a resonator for plasma waves. The plasmon frequency depends on its dimension and easily exceeds THz by setting the gate length at hundreds of nanometers. However, effi-

ciently coupling nonradiative plasmons to radiative electromagnetic waves proved a major challenge. To improve operating frequency, a novel detector which exploits electronic-charge vibrations has been proposed by introducing an interdigitated dual-grating gate structure into a standard HEMT [302]. This new HEMT-based plasmon-resonant detector is well suited to spectroscopic measurement in the low-to-mid THz range, roughly 0.5 to 6.5 THz.

## 17. Conclusions

THz technologies are actively spreading in different areas of human activity. Progress in THz detector technology achieves the level that performance many discrete and low pixel arrays operated at low or sub-Kelvin temperature are close to ultimate performance at low background in the whole THz range. Detector development is at the heart of all current plants. There exist a large variety of traditional deeply cooled mm and sub-mm wavelength detectors as well as new propositions based on novel optoelectronic quantum devices, e.g. carbon nanotube sensors and plasma wave detection by field effect transistors.

Low-temperature operating heterodyne detectors based on SIS structures operated at low or sub-Kelvin temperature are now the most sensitive devices, giving high spectral resolution ( $\nu/\Delta\nu \approx 10^6$ ) and operation close to quantum limit at  $\nu < 0.7$  THz. But today they can have only limited number of pixels, because of limited power of solid state sources used as LOs in these spectral regions to satisfy the needs of very high resolution spectroscopy. The future sensitivity improvement in instruments will come with the use of large format arrays with readouts in the focal plane to provide the demands of high-resolution spectroscopy (with  $\nu/\Delta\nu \approx 10^7$  at  $\nu \approx 1$  THz) and vision demands. In the frequency range above 1 THz, HEB mixers on the base of superconducting ultrathin NbN layers have the best performance and are promising to be used in large format arrays, due to low LO powers needed for their operation. Superconducting HEB detectors are also promising as single-photon counters in near IR with low dark counts and GHz counting rate. HTSC HEBs, because of their excess noise, are not expected to reach the sensitivity of low temperature superconducting HEBs, but due to short electron-phonon relaxation time, these materials are candidates for wide-band devices.

Uncooled and cooled heterodyne SBDs can provide relatively high sensitivity appropriate to many applications in mm and sub-mm spectral range, but they can be assembled hardly in large number pixel arrays, because of the lack of high power compact solid state LO sources with needed power above 1 mW. Today systems with single pixel coherent SBD detectors and arrays with modest number of pixels are available but they failure in applications at  $\nu > 1$  THz because of physical restrictions in their operation. It is predicted that an alternative method of Schottky barrier formation based on ErAs/InGaAlAs films on InP substrates will

give about two orders of magnitude better sensitivity than typical GaAs Schottky diodes.

Uncooled or slightly cooled detectors on the base of 2D electrons plasmon resonance in FETs, though they are still in the stage of research and optimisation, are promising to be used in large format arrays of the low-cost systems. One of the important tasks lies in designing the arrays with ROICs, obtaining really fully integrated FPAs. Other well established uncooled THz thermal direct detection detectors with  $NEP$  between  $10^{-10}$  and  $10^{-11}$  W/Hz<sup>1/2</sup> could be used in many low-resolution spectroscopy applications and active vision systems.

Direct detection detectors like superconducting HEBs have high sensitivity and are fast ( $\tau \approx 10^{-10}$  s). Direct detection TESs (bolometers) with small volumes ( $\approx 3 \times 10^{-3}$   $\mu\text{m}^3$ ) are extremely sensitive at sub-Kelvin operation conditions and are relatively fast ( $\tau \approx 10^{-5}$  s) allowing high data rate transfer and counting of THz phonons. Their performance can be close to BLIP regime in the case of very low cold background. They can be much easier assembled into large format arrays compared to heterodyne detectors, as there is no need of LOs.

Serious obstacles in the THz technology are relatively low detection sensitivity of uncooled detectors used that operate far away of BLIP conditions and the low imaging resolution. However, recently, several types of photon detectors have been created with nano-structured semiconductors, superconductors, and carbon nanotube devices. It is expected that these novel devices will be used in a real-time THz video cameras.

## Acknowledgements

This paper has also been done under financial support of the Polish Ministry of Sciences and Higher Education, Key Project POIG.01.03.01-14-016/08 ••New photonic materials and their advanced application••.

## References

1. P.H. Siegel, "Terahertz technology", *IEEE T. Microw. Theory* **50**, 910–928 (2002).
2. P.H. Siegel and R.J. Dengler, "Terahertz heterodyne imaging Part I: Introduction and techniques", *Int. J. Infrared Millimeter Waves* **27**, 465–480 (2006).
3. P.H. Siegel and R.J. Dengler, "Terahertz heterodyne imaging Part II: Instruments", *Int. J. Infrared Milli.* **27**, 631–655 (2006).
4. G. Chattopadhyay, "Submillimeter-wave coherent and incoherent sensors for space applications," in *Sensors. Advances in Modeling, Design Issues, Fabrication and Practical Applications*, pp. 387–414, edited by S.C. Mukhopadhyay and R.Y.M. Huang, Springer, New York, 2008.
5. T.W. Crowe, W.L. Bishop, D.W. Porterfield, J.L. Hesler, and R.M. Weikle, "Opening the terahertz window with integrated diode circuits", *IEEE J. Solid-St. Circ.* **40**, 2104–2110 (2005).
6. D. Dragoman and M. Dragoman, "Terahertz fields and applications", *Prog. Quant. Electron.* **28**, 1–66 (2004).

7. J. Wei, D. Olaya, B.S. Karasik, S.V. Pereverzev, A.V. Sergeev, and M.E. Gershenzon, "Ultrasensitive hot-electron nanobolometers for terahertz astrophysics", *Nat. Nanotechnol.* **3**, 496–500 (2008).
8. A.H. Lettington, I.M. Blankson, M. Attia, and D. Dunn, "Review of imaging architecture", *Proc. SPIE* **4719**, 327–340 (2002).
9. A.W. Blain, I. Smail, R.J. Ivison, J.-P. Kneib, and D.T. Frayer, "Submillimetre galaxies", *Phys. Rep.* **369**, 111–176 (2002).
10. D. Leisawitz, W.C. Danchi, M.J. DiPirro, L.D. Feinberg, D.Y. Gezari, M. Hagopian, W.D. Langer, J.C. Mather, S.H. Moseley, M. Shao, R.F. Silverberg, J.G. Staguhn, M.R. Swain, H.W. Yorke, and X. Zhang, "Scientific motivation and technology requirements for the SPIRIT and SPECS far-infrared/submillimeter space interferometers", *Proc. SPIE* **4013**, 36–46 (2000).
11. "10 emerging technologies that will change your world", *Technology Review*, 32–50, February 2004.
12. J. Zmuidzinas and P.L. Richards, "Superconducting detectors and mixers for millimeter and submillimeter astrophysics", *Proc. IEEE* **92**, 1597–1616 (2004).
13. B. Ferguson and X.-C. Zhang, "Materials for terahertz science and technology", *Nat. Mater.* **1**, 26–33 (2002).
14. D. Mittleman, *Sensing with Terahertz Radiation*, Springer-Verlag, Berlin, 2003.
15. E.R. Brown, "Fundamentals of terrestrial millimetre-wave and THz remote sensing", *Int. J. High Speed Electron.* **13**, 99–1097 (2003).
16. R.M. Woodward, "Terahertz technology in global homeland security", *Proc. SPIE* **5781**, 22–31 (2005).
17. D.L. Woolard, R. Brown, M. Pepper, and M. Kemp, "Terahertz frequency sensing and imaging: A time of reckoning future applications?", *Proc. IEEE* **93**, 1722–1743 (2005).
18. H. Zhong, A. Redo-Sanchez, and X.-C. Zhang, "Identification and classification of chemicals using terahertz reflective spectroscopic focal-plane imaging system", *Opt. Express* **14**, 9130–9141 (2006).
19. M. Tonouchi, "Cutting-edge terahertz technology", *Nat. Photonics* **1**, 97–105 (2007).
20. A. Rostami, H. Rasooli, and H. Baghban, *Terahertz Technology. Fundamentals and Applications*, Springer, Berlin, 2011.
21. T.G. Phillips and J. Keene, "Submillimeter astronomy", *Proc. IEEE* **80**, 1662–1678 (1992).
22. R. Piesiewicz, T. Kleine-Ostmann, N. Krumbholz, D. Mittleman, M. Koch, J. Schoebel, and T. Kuerner, "Short-range ultra-broadband terahertz communications: concept and perspectives", *IEEE Antenn. Propag. M.* **49**, 24–35 (2007).
23. F. Sizov, "THz radiation sensors", *Opto-Electron. Rev.* **18**, 10–36 (2010).
24. F. Sizov and A. Rogalski, "THz detectors", *Prog. Quant. Electron.* **34**, 278–347 (2010).
25. S. Komiyama, O. Astafiev, V. Antonov, T. Kutsuwa, and H. Hirai, "A single-photon detector in the far-infrared range", *Nature* **403**, 405–407 (2000).
26. S. Komiyama, "Single-photon detectors in terahertz region", *IEEE J. Sel. Top. Quant.* **17**, 54–66 (2011).
27. G. Chattopadhyay, "Heterodyne arrays at submillimeter wavelengths", *38-th General Assembly of Int. Union of Radio Science*, New Delhi, October, 2005.
28. P.F. Goldsmith, Ph. Appleton, L. Armus, J. Bauer, D. Benford, A. Blaind, M. Bradford, G. Bryden, M. Dragovan, M. Harwit, G. Helou, W.D. Langer, D. Leisawitz, C. Paine, and H. Yorke, "CALISTO: The cryogenic aperture large infrared space telescope observatory", <http://www.ipac.caltech.edu/DecadalSurvey/farir.html>).
29. M. Harwit, G. Helou, L. Armus, C.M. Bradford, P.F. Goldsmith, M. Hauser, D. Leisawitz, D.F. Lester, G. Rieke, and S.A. Rinehart, "Far-infrared/submillimeter astronomy from space tracking an evolving universe and the emergence of life", <http://www.ipac.caltech.edu/DecadalSurvey/farir.html>
30. J.J. Bock, "Superconducting detector arrays for far-infrared to mm-wave astrophysics", [http://cmbpol.uchicago.edu/depot/pdf/white-paper\\_j-bock.pdf](http://cmbpol.uchicago.edu/depot/pdf/white-paper_j-bock.pdf)
31. S. Hargreaves and R.A. Lewis, "Terahertz imaging: Materials and methods", *J. Mater. Sci.: Mater. Electron.* **18**, S299–S303 (2007).
32. N. Karpowicz, H. Zhong, J. Xu, K.-I. Lin, J.-S. Hwang, and X.-C. Zhang, "Non-destructive sub-THz CW imaging", *Proc. SPIE* **5727**, 132–142 (2005).
33. A. Dobroiu, M. Yamashita, Y.N. Ohshima, Y. Morita, C. Otani, and K. Kawase, "Terahertz imaging system based on a backward oscillator", *Appl. Opt.* **43**, 5637–5646 (2004).
34. A.W.M. Lee, Q. Qin, S. Kumar, B.S. Williams, Q. Hu, and J.L. Reno, "Real-time terahertz imaging over a standoff distance (> 25 meters)", *Appl. Phys. Lett.* **89**, 141125 (2006).
35. A.W.M. Lee, B.S. Williams, S. Kumar, Q. Hu, and J. L. Reno, "Real-time imaging using a 4.3-THz quantum cascade laser and a 320×240 microbolometer focal-plane array", *IEEE Photon. Tech. L.* **18**, 1415–1417 (2006).
36. F.F. Sizov, V.P. Reva, A.G. Golenkov, and V.V. Zabudsky, "Uncooled detector challenges for THz/sub-THz arrays imaging", *J. Infrared Millim. Te.*, DOI 10.1007/s10762-011-9789-2 (2011).
37. M.A. Kinch and B.V. Rollin, "Detection of millimetre and sub-millimetre wave radiation by free carrier absorption in a semiconductor", *Brit. J. Appl. Phys.* **14**, 672–676 (1963).
38. Y. Nakagawa and H. Yoshinaga, "Characteristics of high-sensitivity Ge bolometer", *Jpn. J. Appl. Phys.* **9**, 125–131 (1970).
39. T.-L. Hwang, S.E. Scharz, and D.B. Rutledge, "Microbolometers for infrared detection", *Appl. Phys. Lett.* **34**, 773–776 (1979).
40. E.E. Haller, M.R. Hueschen, and P.L. Richards, "Ge:Ga photoconductors in low infrared backgrounds", *Appl. Phys. Lett.* **34**, 495–497 (1979).
41. P.L. Richards, "Bolometers for infrared and millimeter waves", *J. Appl. Phys.* **76**, 1–24 (1994).
42. J.E. Huffman, "Infrared detectors for 2 to 220  $\mu\text{m}$  astronomy", *Proc. SPIE* **2274**, 157–169 (1995).
43. W.W. Hübers, S.G. Pavlov, K. Holldack, U. Schade, and G. Wüstefeld, "Long wavelength response of unstressed and stressed Ge:Ga detectors", *Proc. SPIE* **6275**, 627505 (2008).
44. A. Poglisch, R.O. Katterloher, R. Hoenle, J.W. Beeman, E.E. Haller, H. Richter, U. Groezinger, N.M. Haegel, and A. Krabbe, "Far-infrared photoconductors for Herschel and SOFIA", *Proc. SPIE* **4855**, 115–128 (2003).
45. M. Kenyon, P.K. Day, C.M. Bradford, J.J. Bock, and H.G. Leduc, "Progress on background-limited membrane-isolated TES bolometers for far-IR/submillimeter spectroscopy", *Proc. SPIE* **6275**, 627508 (2006).
46. A.D. Turner, J.J. Bock, J.W. Beeman, J. Glenn, P.C. Hargrave, V.V. Hristov, H.T. Nguyen, F. Rahman, S. Sethuraman, and A.L. Woodcraft, "Silicon nitride micromesh bolo-



- meter array for submillimeter astrophysics", *Appl. Optics* **40**, 4921–4932 (2001).
47. B.S. Karasik, D. Olaya, J. Wei, S. Pereverzev, M.E. Gershenson, J.H. Kawamura, W.R. McGrath, and A. V. Sergeev, "Record-low NEP in hot-electron titanium nanobolometers", *IEEE T. Appl. Supercon.* **17**, 293–297 (2007).
  48. H.-W. Hübers, "Terahertz heterodyne receivers", *IEEE J. Sel. Top. Quant.* **14**, 378–391 (2008).
  49. D.J. Benford, "Transition edge sensor bolometers for CMB polarimetry", [http://cmbpol.uchicago.edu/workshops/technology2008/depot/cmbpol\\_technologies\\_benford\\_jcps\\_4.pdf](http://cmbpol.uchicago.edu/workshops/technology2008/depot/cmbpol_technologies_benford_jcps_4.pdf)
  50. P.L. Richards, "Cosmic microwave background experiments – past, present and future", <http://sciencestage.com/d/5334058/>
  51. F. Sizov, *Photoelectronics for Vision Systems in Invisible Spectral Ranges*, Akademperiodika, Kiev, 2008. (in Russian).
  52. N. Kopeika, *A System Engineering Approach to Imaging*, SPIE Optical Eng. Press, Bellingham, 1998.
  53. A.D. Turner, J.J. Bock, J.W. Beeman, J. Glenn, P.C. Hargrave, V.V. Hristov, H.T. Nguyen, F. Rahman, S. Sethuraman, and A.L. Woodcraft, "Silicon nitride micro-mesh bolometer array for submillimeter astrophysics", *Appl. Optics* **40**, 4921–4932 (2001).
  54. "Detectors needs for long wavelength astrophysics", *A Report by the Infrared, Submillimeter, and Millimeter Detector Working Group*, June 2002; [http://safir.gsfc.nasa.gov/docs/ISMDWG\\_final.pdf](http://safir.gsfc.nasa.gov/docs/ISMDWG_final.pdf)
  55. J. Glenn, P.A.R. Ade, M. Amarie, J.J. Bock, S.F. Edgington, A. Goldin, S. Golwala, D. Haig, A.E. Lange, G. Laurent, P.D. Maudkopf, M. Yun, and H. Nguyen, "Current status of Bolocam: a large-format millimeter-wave bolometer camera", *Proc. SPIE* **4855**, 30–40 (2003).
  56. G.M. Voellmer, C.A. Allen, M.J. Amato, S.R. Babu, A.E. Bartels, D.J. Benford, R.J. Derro, C.D. Dowell, D.A. Harper, M.D. Jhabvala, S.H. Moseley, T. Rennick, P.J. Shirron, W.W. Smith, and J.G. Staguhn, "Design and fabrication of two-dimensional semiconducting bolometer arrays for HAWC and SHARC-II", *Proc. SPIE* **4855**, 63–72 (2003).
  57. J.G. Staguhn, D.J. Benford, F. Pajot, T.J. Ames, J.A. Chervenak, E.N. Grossman, K.D. Irwin, B. Maffei, S.H. Moseley, T.G. Phillips, C.D. Reintsema, C. Rioux, R.A. Shafer, and G.M. Vollmer, "Astronomical demonstration of superconducting bolometer arrays", *Proc. SPIE* **4855**, 100–107 (2003).
  58. T.W. Crowe, R.J. Mattauch, H.-P. Roser, W.L. Bishop, W.C.B. Peatman, and X. Liu, "GaAs Schottky diodes for THz mixing applications", *Proc. IEEE* **80**, 1827–1841 (1992).
  59. G.L. Carr, M.C. Martin, W.R. McKinney, G.R. Neil, K. Jordan, and G.P. Williams, "High power terahertz radiation from relativistic electrons", *Nature* **420**, 153 (2002).
  60. M. Rodwell, E. Lobisser, M. Wistey, V. Jain, A. Baraskar, E. Lind, J. Koo, B. Thibeault, A.C. Gossard, Z. Griffith, J. Hacker, M. Urteaga, D. Mensa, R. Pierson, and B. Brar, "Development of THz transistors and (300–3000 GHz) sub-mm-wave integrated circuits", *The 11<sup>th</sup> Inter. Symp. on Wireless Personal Multimedia Communications* (WPMC 2008); [http://www.ece.ucsb.edu/Faculty/Rodwell/publications/2008\\_9\\_sept\\_wpmc\\_rodwell\\_digest.pdf](http://www.ece.ucsb.edu/Faculty/Rodwell/publications/2008_9_sept_wpmc_rodwell_digest.pdf)
  61. B.S. Williams, "Terahertz quantum-cascade lasers", *Nat. Photonics* **1**, 517–525 (2007).
  62. J.R. Tucker and M.J. Feldman, "Quantum detection at millimeter wavelength", *Rev. Mod. Phys.* **57**, 1055–1113 (1985).
  63. C.M. Bradford, B.J. Naylor, J. Zmuidzinas, J.J. Bock, J. Gromke, H. Nguyen, M. Dragovan, M. Yun, L. Earle, J. Glenn, H. Matsuhara, P.A.R. Ade, and L. Duband, "WaFIRS: A waveguide far-IR spectrometer: Enabling spectroscopy of high-z galaxies in the far-IR and submillimeter", *Proc. SPIE* **4850**, 1137–1148 (2003).
  64. M. Kenyon, P.K. Day, C.M. Bradford, J.J. Bock, and H.G. Leduc, "Progress on background-limited membrane-isolated TES bolometers for far-IR/submillimeter spectroscopy", *Proc. SPIE* **6275**, 627508 (2006).
  65. B.S. Karasik and R. Cantor, "Optical NEP in hot-electron nanobolometers", *21<sup>st</sup> International Symposium on Space Terahertz Technology*, Oxford, 23–25 March, 2010.
  66. J.C. Mather, E.S. Cheng, D.A. Cottingham, R.E. Eplee, D.J. Fixsen, T. Hewagama, R.B. Isaacman, K.A. Jensen, S.S. Meyer, P.D. Noerdlinger, S.M. Read, L.P. Rosen, R.A. Shafer, E.L. Wright, C.L. Bennett, N.W. Boggess, M.G. Hauser, T. Kelsall, S.H. Moseley, R.F. Silverberg, G.F. Smoot, R. Weiss, and D.T. Wilkinson, "Measurement of the cosmic microwave background spectrum by the COBE FIRAS instrument", *Astrophys. J.* **420**, 439–444 (1994).
  67. J. Dunkley, A. Amblard, C. Baccigalupi, M. Betoule, D. Chuss, A. Cooray, J. Delabrouille, C. Dickinson, G. Dobler, J. Dotson, H.K. Eriksen, D. Finkbeiner, D. Fixsen, P. Fosalba, A. Fraisse, C. Hirata, A. Kogut, J. Kristiansen, C. Lawrence, A.M. Magalhaes, M.A. Miville-Deschenes, S. Meyer, A. Miller, S.K. Naess, L. Page, H.V. Peiris, N. Phillips, E. Pierpaoli, G. Rocha, J.E. Vaillancourt, and L. Verde, "A program of technology development and of sub-orbital observations of the cosmic microwave background polarization leading to and including a satellite mission", *A Report for the Astro-2010 Decadal Committee on Astrophysics*, April, 2009.
  68. D.H. Auston, "Picosecond optoelectronic switching and gating in silicon", *Appl. Phys. Lett.* **26**, 101–103 (1975).
  69. P. LeFur and D.H. Auston, "A kilovolt picosecond optoelectronic switch and Pockels cell", *Appl. Phys. Lett.* **28**, 21–33 (1976).
  70. J.A. Valdmani, G. Mourou, and C.W. Gabel, "Picosecond electrooptic sampling system", *Appl. Phys. Lett.* **41**, 211–212 (1982).
  71. D. Grischkowsky, S. Keiding, M. van Exter, and C. Fattinger, "Far-infrared time-domain spectroscopy with teraHz beams of dielectrics and semiconductors", *J. Opt. Soc.* **B7**, 2006–2015 (1990).
  72. M. Tani, Y. Hirota, C. Que, S. Tanaka, R. Hattori, M. Yamaguchi, S. Nishizawa, and M. Hangyo, "Novel terahertz photoconductive antennas", *Int. J. Infrared Milli.* **27**, 531–546 (2006).
  73. D.M. Mittleman, M. Gupta, R. Neelamani, R.G. Baraniuk, J.V. Rudd, and M. Koch, "Recent advances in terahertz imaging", *Appl. Phys. B*, DOI 10.1007/s003409900011 (1999).
  74. W.L. Chan, J. Deibel, and D.M. Mittleman, "Imaging with terahertz radiation", *Rep. Prog. Phys.* **70**, 1325–1379 (2007).
  75. L. Xu, X.-C. Zhang, and D.H. Auston, "Terahertz beam generation by femtosecond optical pulses in electro-optic materials", *Appl. Phys. Lett.* **61**, 1784–1786 (1992).
  76. E.R. Brown, K.A. McIntosh, F.W. Smith, K.B. Nichols, M.J. Manfra, C.L. Dennis, and J.P. Mattia, "Milliwatt output levels and superquadratic bias dependence in a low-tempera-



- ture-grown GaAs photomixer", *Appl. Phys. Lett.* **64**, 3311–3313 (1994).
77. M. Tani, K.-S. Lee, and X.-C. Zhang, "Detection of terahertz radiation with low-temperature-grown GaAs based photoconductive antenna using 1.55  $\mu\text{m}$  probe", *Appl. Phys. Lett.* **77**, 1396–1398 (2000).
78. M. Suzukia and M. Tonouchi, "Fe-implanted InGaAs photoconductive terahertz detectors triggered by 1.56  $\mu\text{m}$  femtosecond optical pulses", *Appl. Phys. Lett.* **86**, 163504 (2005).
79. H. Page, S. Malik, M. Evans, I. Gregory, I. Farrer, and D. Ritchie, "Waveguide coupled terahertz photoconductive antennas: Toward integrated photonic terahertz devices", *Appl. Phys. Lett.* **92**, 163502 (2008).
80. D.P. Neikirk, D.B. Rutledge, and M.S. Mucha, "Far-infrared imaging antenna arrays", *Appl. Phys. Lett.* **40**, 203–205 (1982).
81. D.B. Rutledge, D.P. Neikirk, and D.P. Kasilingam, "Integrated-circuit antennas", in: *Infrared and Millimeter Waves*, Vol. 10, pp. 1–90, ed. K.J. Button, Academic Press, New York, 1983.
82. J. Zhang, Y. Hong, S.L. Braunstein, and K.A. Shore, "Terahertz pulse generation and detection with LT-GaAs photoconductive antenna", *IEEE P-Optoelectron.* **151**, 98–101 (2004).
83. E.R. Brown, A.W.M. Lee, B.S. Navi, and J.E. Bjarnason, "Characterization of a planar self-complementary square-spiral antenna in the THz region", *Microw. Opt. Techn. Lett.* **48**, 524–529 (2006).
84. J. Grade, P. Haydon, and D. van der Weide, "Electronic terahertz antennas and probes for spectroscopic detection and diagnostics", *Proc. IEEE* **95**, 1583–1591 (2007).
85. R.C. Jones, "Phenomenological description of the response and detecting ability of radiation detectors", *P. IRE* **47**, 1495–1502 (1959).
86. A. Rogalski, *Infrared Detectors*, 2<sup>nd</sup> edition, CRC Press, Boca Raton, 2011.
87. T. Ueda, Z. An, and S. Komiyama, "Temperature dependence of novel single-photon detectors in the long-wavelength infrared range", *J. Infrared Millim. Te.*; DOI 10.1007/s10762-010-9659-3 (2010).
88. A.G.U. Perera, G. Ariyawansaa, P.V.V. Jayaweeraa, S.G. Matsika, M. Buchanan, and H.C. Liu, "Semiconductor terahertz detectors and absorption enhancement using plasmons", *Microelectron. J.* **39**, 601–606 (2008).
89. H.C. Liu, H. Luo, C.-Y. Song, Z.R. Wasilewski, A.J. SpringThorpe, and J.C. Cao, "Terahertz quantum well photo-detectors", *IEEE J. Sel. Top. Quant.* **14**, 374–377 (2008).
90. D.G. Esaev, M.B.M. Rinzan, S.G. Matsik, and A.G.U. Perera, "Design and optimization of GaAs/AlGaAs heterojunction infrared detectors", *J. Appl. Phys.* **96**, 4588–4597 (2004); A.G.U. Perera and W.Z. Shen, "GaAs homojunction interfacial workfunction internal photoemission (HIWIP) far-infrared devices", *Opto-Electron Rev.* **7**, 153–180 (1999).
91. H.C. Liu, "Quantum dot infrared photodetector", *Opto-Electron. Rev.* **11**, 1–5 (2003).
92. J.A. Ratches, "Current and future trends in military night vision applications", *Ferroelectrics* **342**, 183–192 (2006).
93. M. Kohin and N. Butler, "Performance limits of uncooled  $\text{VO}_x$  microbolometer focal-plane arrays", *Proc. SPIE* **5406**, 447–453 (2004).
94. W. Kruse, L.D. McGlauchlin and R.B. McQuistan, *Elements of Infrared Technology*, Wiley, New York, 1962.
95. E.H. Putley, "Thermal detectors", in *Optical and Infrared Detectors*, pp. 71–100, edited by R.J. Keyes, Springer, Berlin, 1977.
96. P.W. Kruse, *Uncooled Thermal Imaging*, SPIE Press, Bellingham, 2001.
97. G.H. Rieke, *Detection of Light: From the Ultraviolet to the Submillimeter*, Cambridge University Press, Cambridge, 2003.
98. W. Whatmore, "Pyroelectric devices and materials", *Rep. Prog. Phys.* **49**, 1335–1386 (1986).
99. P. Muralt, "Micromachined infrared detectors based on pyroelectric thin films", *Rep. Prog. Phys.* **64**, 1339–1338 (2001).
100. V.G. Bozhkov, "Semiconductor detectors, mixers, and frequency multipliers for the terahertz band", *Radiophys. Quantum. El.* **46**, 631–656 (2003).
101. A. Van Der Ziel, "Infrared detection and mixing in heavily doped Schottky barrier diodes", *J. Appl. Phys.* **47**, 2059–2068 (1976).
102. H.A. Watson, *Microwave Semiconductor Devices and their Circuit Applications*, McGraw-Hill, New York, 1969.
103. E.J. Becklake, C.D. Payne, and B.E. Pruer, "Submillimetre performance of diode detectors using Ge, Si and GaAs", *J. Phys. D: Appl. Phys.* **3**, 473–481 (1970).
104. D.T. Young and J.C. Irvin, "Millimeter frequency conversion using Au-n-type GaAs Schottky barrier epitaxial diodes with a novel contacting technique", *Proc. IEEE* **53**, 2130–2132 (1965).
105. T.W. Crowe, D.P. Porterfield, J.L. Hesler, W.L. Bishop, D.S. Kurtz, and K. Hui, "Terahertz sources and detectors", *Proc SPIE* **5790**, 271–280 (2005).
106. H.P. Röser, H.-W. Hübers, E. Bründermann, and M.F. Kimmitt, "Observation of mesoscopic effects in Schottky diodes at 300 K when used as mixers at THz frequencies", *Semicond. Sci. Tech.* **11**, 1328–1332 (1996).
107. T.W. Crowe and W.C.B. Peatman, "GaAs Schottky diodes for mixing applications beyond 1 THz", *2nd Int. Symp. on Space Terahertz Technology* 323–339, Pasadena, February 26–28, 1991, <http://www.nrao.edu/meetings/isstt/papers/1991/1991323339.pdf>
108. T.W. Crowe, "GaAs Schottky barrier mixer diodes for the frequency range 1–10 THz", *Int. J. Infrared Milli.* **11**, 765–777 (1990).
109. H. Kräutle, E. Sauter, and G.V. Schultz, "Antenna characteristics of whisker diodes used at submillimeter receivers", *Infrared Phys.* **17**, 477–483 (1977).
110. R. Titz, B. Auel, W. Esch, H.P. Röser, and G.W. Schwaab, "Antenna measurements of open-structure Schottky mixers and determination of optical elements for a heterodyne system at 184, 214 and 287  $\mu\text{m}$ ", *Infrared Phys.* **30**, 435–441 (1990).
111. I. Mehdi, G. Chattopadhyay, E. Schlecht, J. Ward, J. Gill, F. Maiwald, and A. Maestrini, "THz multiplier circuits", *IEEE MTT-S Intern. Microwave Symp. Digest*, 341–344, San Francisco, 2006.
112. S.M. Marazita, W.L. Bishop, J.L. Hesler, K. Hui, W.E. Bowen, and T.W. Crowe, "Integrated GaAs Schottky mixers by spin-on-dielectric wafer bonding", *IEEE T. Electron. Dev.* **47**, 1152–1156 (2000).
113. P. Siegel, R.P. Smith, M.C. Gaidis, and S. Martin, "2.5-THz GaAs monolithic membrane-diode mixer", *IEEE T. Microw. Theory* **47**, 596–604 (1999).

114. J.A. Copeland, "Diode edge effects on doping profile measurements", *IEEE T. Electron Dev.* **17**, 404–407 (1970).
115. V.I. Piddiyachiy, V.M. Shulga, A.M. Korolev, and V.V. Myshenko, "High doping density Schottky diodes in the 3 mm wavelength cryogenic heterodyne receiver", *Int. J. Infrared Milli.* **26**, 1307–1315 (2005).
116. J.L. Hesler and T.W. Crowe, "Responsivity and noise measurements of zero-bias Schottky diode detectors", <http://www.virginiadiodes.com/VDI/pdf/VDI%20Detector%20Char%20ISSTT2007.pdf>
117. H. Kazemi, G. Nagy, L. Tran, E. Grossman, E.R. Brown, A.C. Gossard, G.D. Boreman, B. Lail, A.C. Young, and J.D. Zimmerman, "Ultra sensitive ErAs/InAlGaAs direct detectors for millimeter wave and THz imaging applications", *IEEE/MTT Int. Microwave Symposium*, 1367–1370 (2007).
118. E.R. Brown, A.C. Young, J.E. Bjarnason, J.D. Zimmerman, A.C. Gossard, and H. Kazemi, "Millimeter and sub-millimeter wave performance of an ErAs/InAlGaAs Schottky diode coupled to a single-turn square spiral", *Int. J. High Speed Electron.* **17**, 383–394 (2007).
119. [http://www.darpa.mil/mto/programs/tift/pdf/MTT\\_THz\\_Workshop.pdf](http://www.darpa.mil/mto/programs/tift/pdf/MTT_THz_Workshop.pdf)
120. F. Maiwald, F. Lewen, B. Vowinkel, W. Jabs, D.G. Paveljev, M. Winnerwischer, and G. Winnerwischer, "Planar Schottky diode frequency multiplier for molecular spectroscopy up to 1.3 THz", *IEEE Microw. Guided W.* **9**, 198–200 (1999).
121. D.H. Martin, *Spectroscopic Techniques for Far-infrared, Submillimeter and Millimeter Waves*, North-Holland, Amsterdam, 1967.
122. B.V. Rollin and E.L. Simmons, "Long wavelength infrared photoconductivity of silicon at low temperatures", *Proc. Phys. Soc.* **B65**, 995–996 (1952).
123. E. Burstein, J.J. Oberly and J.W. Davisson, "Infrared photoconductivity due to neutral impurities in silicon", *Phys. Rev.* **89**, 331–332 (1953).
124. P.R. Bratt, "Impurity germanium and silicon infrared detectors", in *Semiconductors and Semimetals*, Vol. 12, pp. 39–142, edited by R.K. Willardson and A.C. Beer, Academic Press, New York, 1977.
125. J. Wolf, C. Gabriel, U. Grözinger, I. Heinrichsen, G. Hirth, S. Kirches, D. Lemke, J. Schubert, B. Schulz, C. Tilgner, M. Boison, A. Frey, I. Rasmussen, R. Wagner and K. Proetel, "Calibration facility and preflight characterization of the photometer in the Infrared Space Observatory", *Opt. Eng.* **33**, 26–36 (1994).
126. G.H. Rieke, M.W. Werner, R.I. Thompson, E.E. Becklin, W.F. Hoffmann, J.R. Houck, F.J. Low, W.A. Stein, and F.C. Witteborn, "Infrared astronomy after IRAS", *Science* **231**, 807–814 (1986).
127. J. Leotin, "Far infrared photoconductive detectors", *Proc. SPIE* **666**, 81–100 (1986).
128. Sclar, "Properties of doped silicon and germanium infrared detectors", *Prog. Quant. Electron.* **9**, 149–257 (1984).
129. E.E. Haller, "Advanced far-infrared detectors", *Infrared Phys. Techn.* **35**, 127–146 (1994).
130. N.M. Haegel and E.E. Haller, "Extrinsic germanium photoconductor material: crystal growth and characterization", *Proc. SPIE* **659**, 188–194 (1986).
131. J.-Q. Wang, P.I. Richards, J.W. Beeman, J.W. Haegel, and E.E. Haller, "Optical efficiency of far-infrared photoconductors", *Appl. Opt.* **25**, 4127–4134 (1986).
132. A.G. Kazanskii, P.L. Richards and E.E. Haller, "Far-infrared photoconductivity of uniaxially stressed germanium", *Appl. Phys. Lett.* **31**, 496–497 (1977).
133. E.E. Haller, M.R. Hueschen, and P.L. Richards, "Ge:Ga photoconductors in low infrared backgrounds", *Appl. Phys. Lett.* **34**, 495–497 (1979).
134. J. Wolf, C. Gabriel, U. Grözinger, I. Heinrichsen, G. Hirth, S. Kirches, D. Lemke, J. Schubert, B. Schulz, C. Tilgner, M. Boison, A. Frey, I. Rasmussen, R. Wagner and K. Proetel, "Calibration facility and preflight characterization of the photometer in the Infrared Space Observatory", *Opt. Eng.* **33**, 26–36 (1994).
135. E. Young, J. Stansberry, K. Gordon, and J. Cadien, "Properties of germanium photoconductor detectors", in *Proc. Conf. ESA SP-481*, pp. 231–235, edited by L. Metcalfe, A. Salama, S.B. Peschke, and M.F. Kessler, VilSpa, 2001.
136. N. Hiromoto, M. Fujiwara, H. Shibai and H. Okuda, "Ge:Ga far-infrared photoconductors for space applications", *Jpn. J. Appl. Phys.* **35**, 1676–1680 (1996).
137. Y. Doi, S. Hirooka, A. Sato, M. Kawada, H. Shibai, Y. Okamura, S. Makiuti, T. Nakagawa, N. Hiromoto, and M. Fujiwara, "Large-format and compact stressed Ge:Ga array for the Astro-F (IRIS) mission", *Adv. Space Res.* **30**, 2099–2104 (2002).
138. E.T. Young, J.T. Davis, C.L. Thompson, G.H. Rieke, G. Rivlis, R. Schnurr, J. Cadien, L. Davidson, G.S. Winters, and K.A. Kormos, "Far-infrared imaging array for SIRTf", *Proc. SPIE* **3354**, 57–65 (1998).
139. A. Poglitsch, C. Waelkens, O.H. Bauer, J. Cepa, H. Feuchtgruber, T. Henning, C. van Hoof, F. Kerschbaum, O. Krause, E. Renotte, L. Rodriguez, P. Saraceno, and B. Vandenbusche, "The photodetector array camera and spectrometer (PACS) for the Herschel Space Laboratory", *Proc. SPIE* **7010**, 701005 (2008).
140. <http://fifi-ls.mpg-garching.mpg/dr/detector.html>
141. <http://pacs.mpe.mpg.de/p15n.html>
142. N. Billot, P. Agnese, J.L. Augeres, A. Beguin, and A. Bouere, O. Boulade, C. Cara, C. Cloue, E. Doumayrou, L. Duband, B. Horeau, I. Le Mer, J.L. Pennec, J. Martignac, K. Okumura, V. Reveret, M. Sauvage, F. Simoens, and L. Vigroux, "The Herschel/PACS 2560 bolometers imaging camera", *Proc. SPIE* **6265**, 62650D (2006).
143. M. Shirahata, S. Matsuura, T. Nakagawa, T. Wada, S. Kamiya, M. Kawada, Y. Sawayama, Y. Doi, H. Kawada, Y. Creten, B. Okcan, W. Raab, and A. Poglitsch, "Development of a far-infrared Ge:Ga monolithic array detector for SPICA a possible application to SPICA", *Proc. SPIE* **7741**, 77410B (2010).
144. J. Farhoomand, D.L. Sisson, and J.W. Beeman, "Viability of layered-hybrid architecture for far IR focal-plane arrays", *Infrared Phys. Techn.* **51**, 152–159 (2008).
145. M. Ressler, H. Hogue, M. Muzilla, J. Blacksberg, J. Beeman, E. Haller, J. Huffman, J. Farhoomand, and E. Young "Development of large format far-infrared detectors", *Astro2010: The Astronomy and Astrophysics Decadal Survey, Technology Development Papers*, no. 18.
146. H.H. Houge, M.G. Mlynchzak, M.N. Abedin, S.A. Masterjohn, and J.E. Huffman, "Far-infrared detector development for space-based Earth observation", *Proc. SPIE* **7082**, 70820E-1–8 (2008).

147. J. Bandaru, J.W. Beeman, and E.E. Haller, "Growth and performance of Ge:Sb blocked impurity band (BIB) detectors", *Proc. SPIE* **4486**, 193–199 (2002).
148. L.A. Reichertz, J.W. Beeman, B.L. Cardozo, G. Jakob, R. Katterloher, N.M. Haegel, and E.E. Haller, "Development of a GaAs-based BIB detector for sub-mm wavelengths", *Proc. SPIE* **6275**, 62751S (2006).
149. D.R. Khokhlov, I.I. Ivanchik, S.N. Raines, D.M. Watson, and J.L. Pipher, "Performance and spectral response of  $\text{Pb}_{1-x}\text{Sn}_x\text{Te}(\text{In})$  far-infrared photodetectors", *Appl. Phys. Lett.* **76**, 2835–2837 (2000).
150. K.G. Kristovskii, A.E. Kozhanov, D.E. Dolzhenko, I.I. Ivanchik, D. Watson, and D.R. Khokhlov, "Photoconductivity of lead telluride-based doped alloys in the submillimeter wavelength range", *Phys. Solid State* **46**, 122–124 (2004).
151. A.N. Akimov, V.G. Erkov, V.V. Kubarev, E.L. Molodtsova, A.E. Klimov, and V.N. Shumskiy, "Photosensitivity of  $\text{Pb}_{1-x}\text{Sn}_x\text{Te}:\text{In}$  films in the terahertz region of the spectrum", *Semiconductors* **40**, 164–168 (2006).
152. A. Artamkin, A. Nikorici, L. Ryabova, V. Shklover, and D. Khokhlov, "Continuous focal plane array for detection of terahertz radiation", *Proc. SPIE* **6297**, 62970B (2006).
153. A.N. Akimov, A.E. Klimov, I.G. Neizvestny, V.N. Shumsky, V.V. Kubarev, O.V. Smolin, and E.V. Susov, "Sensitivity of  $\text{Pb}_{1-x}\text{Sn}_x\text{Te}$  films in submillimeter spectral range", *Prikladnaya Fizika* **6**, 12–17 (2007). (in Russian).
154. A. Klimov, V. Shumsky, and V. Kubarev, "Terahertz sensitivity of  $\text{Pb}_{1-x}\text{Sn}_x\text{Te}:\text{In}$ ", *Ferroelectrics* **347**, 111–119 (2007).
155. A.G. Milnes, *Deep Impurities in Semiconductors*, Wiley Interscience, New York, 1973.
156. B.A. Volkov, L.I. Ryabova, and D.R. Khokhlov, "Mixed-valence impurities in lead telluride-based solid solutions", *Phys.-Usp.* **45**, 819–846 (2002).
157. Yu.G. Troyan, F.F. Sizov, and V.M. Lakeenkov, "Relaxation time and current instabilities in highly resistive  $\text{PbTe}:\text{Ga}$  single crystals", *Ukr. J. Phys.* **32**, 467–471 (1987).
158. C. Wilson, L. Frunzio, and D. Prober, "Time-resolved measurements of thermodynamic fluctuations of the particle number in a nondegenerate Fermi gas", *Phys. Rev. Lett.* **87**, 067004 (2001).
159. C.A. Mears, Q. Hu, P.L. Richards, A.H. Worsham, D.E. Prober, and A.V. Raisanen, "Quantum limited heterodyne detection of millimeter waves using superconducting tantalum tunnel junctions", *Appl. Phys. Lett.* **57**, 2487–2489 (1990).
160. E. Burstein, D.N. Langenberg, and B.N. Taylor, "Superconductors as quantum detectors for microwave and sub-millimeter radiation", *Phys. Rev. Lett.* **6**, 92–94 (1961).
161. A.H. Dayem and R.J. Martin, "Quantum interaction of microwave radiation with tunnelling between superconductors", *Phys. Rev. Lett.* **8**, 246–248 (1962).
162. P.K. Tien and J.P. Gordon, "Multiphoton process observed in the interaction of microwave fields with the tunnelling between superconductor films", *Phys. Rev.* **129**, 647–651 (1963).
163. P.L. Richards, T.M. Shen, R.E. Harris, and F.L. Lloyd, "Quasiparticle heterodyne mixing in SIS tunnel junctions", *Appl. Phys. Lett.* **34**, 345–347 (1979).
164. G.J. Dolan, T.G. Phillips, and D.P. Woody, "Low-noise 115; GHz mixing in superconducting oxide-barrier tunnel junctions", *Appl. Phys. Lett.* **34**, 347–349 (1979).
165. J.R. Tucker and M.J. Feldman, "Quantum detection at millimeter wavelength", *Rev. Mod. Phys.* **57**, 1055–1113 (1985).
166. C.A. Mears, Q. Hu, P.L. Richards, A.H. Worsham, D.E. Prober, and A.V. Raisanen, "Quantum limited heterodyne detection of millimeter waves using superconducting tantalum tunnel junctions", *Appl. Phys. Lett.* **57**, 2487–2489 (1990).
167. V.P. Koshelets, S.V. Shitov, L.V. Filippenko, P.N. Dmitriev, A.N. Ermakov, A.S. Sobolev, and M.Yu. Torgashin, "Integrated superconducting sub-mm wave receivers", *Radio-phys. Quant. Electr.* **46**, 618–630 (2003).
168. A. Karpov, D. Miller, F. Rice, J.A. Stern, B. Bumble, H.G. LeDuc, and J. Zmuidzinas, "Low noise SIS mixer for far-infrared radio astronomy", *Proc. SPIE* **5498**, 616–621 (2004).
169. G. Chattopadhyay, "Future of heterodyne receivers at sub-millimeter wavelengths", *Digest IRMMW-THz-2005 Conf.*, 461–462 (2005).
170. G.N. Gol'tsman, "Hot electron bolometric mixers: new terahertz technology", *Infrared Phys. Techn.* **40**, 199–206 (1999).
171. R. Blundell and K.H. Gundlach, "A quasioptical SIN mixer for 230 GHz frequency range", *Int. J. Infrared Milli.* **8**, 1573–1579 (1987).
172. M. Nahum, P.L. Richards, and C.A. Mears, "Design analysis of a novel hot-electron microbolometer", *IEEE T. Appl. Supercon.* **3**, 2124–2127 (1993).
173. M. Nahum and J. Martinis, "Ultrasensitive hot-electron microbolometer", *Appl. Phys. Lett.* **63**, 3075–3077 (1993).
174. D. Chouvaev, D. Sandgren, M. Tarasov, and L. Kuzmin, "Optical qualification of the normal metal hot-electron microbolometer (NHEB)," *12<sup>th</sup> Int. Symp. Space THz Technol.*, San Diego, 446–456 (2001).
175. D. Sandgren, D. Chouvaev, M. Tarasov, and L. Kuzmin, "Fabrication and optical characterization of the normal metal hot-electron microbolometer with Andreev mirrors", *Physica C* **372**, 444–447 (2002).
176. D. Golubev and L. Kuzmin, "Nonequilibrium theory of a hot-electron bolometer with normal metal-insulator-superconductor tunnel junction", *J. Appl. Phys.* **89**, 6464–6472 (2001).
177. D.R. Schmidt, K.W. Lehnert, A.M. Clark, W.D. Duncan, K.D. Irwin, N. Miller, and J.N. Ullom, "A superconductor-insulator-normal metal bolometer with microwave readout suitable for large-format arrays", *Appl. Phys. Lett.* **86**, 053505 (2005).
178. P. Day, H.G. LeDuc, B.A. Mazin, A. Vayonakis, and J. Zmuidzinas, "A broadband superconducting detector suitable for use in large arrays", *Nature* **425**, 817–821 (2003).
179. P.R. Maloney, N.G. Czakon, P.K. Day, R. Duan, J. Gao, J. Glenn, S. Golwala, M. Hollister, H.G. LeDuc, B. Mazin, O. Noroozian, H.T. Nguyen, J. Sayers, J. Schlaerth, J.E. Vaillancourt, A. Vayonakis, P. Wilson, and J. Zmuidzinas, "The MKID camera", *AIP Conf. Proc.* **1185**, 176–179 (2009).
180. SELEX GALILEO; [http://www.selex-sas.com/EN/Common/files/SELEX\\_Galileo/Products/DLATGS\\_dsh.pdf](http://www.selex-sas.com/EN/Common/files/SELEX_Galileo/Products/DLATGS_dsh.pdf).
181. D. Dooley, "Sensitivity of broadband pyroelectric terahertz detectors continues to improve", *Laser Focus World*, May 2010.
182. <http://www.spectrumdetector.com/pdf/datasheets/THZ.pdf>
183. A.L. Woodcraft, R.V. Sudiwal, E. Wakui, and C. Paine, "Hopping conduction in NTD germanium: comparison between measurement and theory", *J. Low Temp. Phys.* **134**, 925–944 (2004).
184. Herschel Space Observatory, <http://herschel.jpl.nasa.gov/spireInstrument.shtml>



185. P. Agnese, C. Buzzi, P. Rey, L. Rodriguez, and J.L. Tissot, "New technological development for far-infrared bolometer arrays", *Proc. SPIE* **3698**, 284–290 (1999).
186. C. Dowell, C.A. Allen, S. Babu, M.M. Freund, M.B. Gardnara, J. Groseth, M. Jhabvala, A. Kovacs, D.C. Lis, S.H. Moseley, T.G. Phillips, R. Silverberg, G. Voellmer, and H. Yoshida, "SHARC II: a Caltech Submillimeter Observatory facility camera with 384 pixels", *Proc. SPIE* **4855**, 73–87 (2003).
187. [http://herschel.esac.esa.int/science\\_instruments.shtml](http://herschel.esac.esa.int/science_instruments.shtml)
188. G.H. Rieke, "Infrared detector arrays for astronomy", *Annu. Rev. Astrophys.* **45**, 77–115 (2007).
189. E.M. Conwell, "High field transport in semiconductors", *Solid State Physics*, Suppl. **9**, Academic Press, New York, 1967.
190. T.G. Phillips and K.B. Jefferts, "A low temperature bolometer heterodyne receiver for millimeter wave astronomy", *Rev. Sci. Instrum.* **44**, 1009–1014 (1973).
191. E.H. Putley, "InSb submillimeter photoconductive detectors", in *Semiconductors and Semimetals*, Vol. 12, pp. 143–167, edited by R.K. Willardson and A.C. Beer, Academic Press, New York, 1977.
192. [http://www.infraredlaboratories.com/InSb\\_Hot\\_e\\_Bolometers.html](http://www.infraredlaboratories.com/InSb_Hot_e_Bolometers.html)
193. P.R. Norton, "Photodetectors", in *Handbook of Optics*, Vol. I, chapter 24, edited by M. Bass, McGraw Hill, New York, 2010.
194. K.S. Yngvesson, J.-X. Yang, F. Agahi, D. Dai, C. Musante, W. Grammer, and K.M. Lau, "AlGaAs/GaAs quasi-bulk effect mixers: Analysis and experiments", *Third Int. Symp. Space THz Techn.* 688–705 (1992).
195. Yu.B. Vasilyev, A.A. Usikova, N.D. Il'inskaya, P.V. Petrov, and Yu.L. Ivanov, "Highly sensitive submillimeter InSb photodetectors", *Semiconductors* **42**, 1234–1236 (2008).
196. H. Moseley and D. McCammon, "High performance silicon hot electron bolometers", *Ninth Int. Workshop on Low Temperature Detectors*, AIP Proc. 605, 103–106 (2002).
197. K. Seeger, *Semiconductor Physics*, Springer, Berlin, 1991.
198. S.M. Smith, M.J. Cronin, R.J. Nicholas, M.A. Brummell, J.J. Harris, and C.T. Foxon, "Millimeter and submillimeter detection using  $\text{Ga}_{1-x}\text{Al}_x\text{As}$ /GaAs heterostructures", *Int. J. Infrared Milli.* **8**, 793–802 (1987).
199. J.-X. Yang, F. Agahi, D. Dai, C.F. Musante, W. Grammer, K.M. Lau, and K.S. Yngvesson, "Wide-bandwidth electron bolometric mixers: a 2DEG prototype and potential for low-noise THz receivers", *IEEE T. Microw. Theory* **41**, 581–589 (1993).
200. G.N. Gol'tsman and K.V. Smirnov, "Electron-phonon interaction in a two-dimensional electron gas of semiconductor heterostructures at low temperatures", *JETP Lett.* **74**, 474–479 (2001).
201. A.A. Verevkin, N.G. Ptitsina, K.V. Smirnov, G.N. Gol'tsman, E.M. Gershenzon, and K.S. Yngvesson, "Direct measurements of energy relaxation times on an AlGaAs/GaAs heterointerface in the range 4.2–50 K", *JETP Lett.* **64**, 404–409 (1996).
202. T. Phillips and D. Woody, "Millimeter-wave and submillimeter-wave receivers", *Annu. Rev. Astron. Astr.* **20**, 285–321 (1982).
203. E.M. Gershenzon, G.N. Gol'tsman, I.G. Gogdize, Y.P. Gusev, A.J. Elant'ev, B.S. Karasik, and A.D. Semenov, "Millimeter and submillimeter range mixer based on electronic heating of superconducting films in the resistive state", *Superconductivity* **3**, 1582–1597 (1990).
204. B. Karasik, G.N. Gol'tsman, B.M. Voronov, S.I. Svechnikov, E.M. Gershenzon, H. Ekström, S. Jacobsson, E. Kolberg, and K.S. Yngvesson, "Hot electron quasioptical NbN superconducting mixer", *IEEE T. Appl. Supercon.* **5**, 2232–2235 (1995).
205. D.E. Prober, "Superconducting terahertz mixer using a transition-edge microbolometer", *Appl. Phys. Lett.* **62**, 2119–2121 (1993).
206. A. Skalare, W.R. McGrath, B. Bumble, H.G. LeDuc, P.J. Burke, A.A. Vereijen, R.J. Schoelkopf, and D.E. Prober, "Large bandwidth and low noise in a diffusion-cooled hot-electron bolometer mixer", *Appl. Phys. Lett.* **68**, 1558–1560 (1996).
207. W.R. McGrath, "Novel hot-electron bolometer mixers for submillimeter applications: An overview of recent developments", *Proc. URSI Int. Symp. on Signals, Systems, and Electronics*, 147–152 (1995).
208. P.J. Burke, R.J. Schoelkopf, D.E. Prober, A. Skalare, W.R. McGrath, B. Bumble, and H.G. LeDuc, "Length scaling of bandwidth and noise in hot-electron superconducting mixers", *Appl. Phys. Lett.* **68**, 3344–3346 (1996).
209. A.D. Semenov, G.N. Gol'tsman, and R. Sobolewski, "Hot-electron effect in semiconductors and its applications for radiation sensors", *Semicond. Sci. Tech.* **15**, R1–R16 (2002).
210. E.M. Gershenson, M.E. Gershenson, G.N. Gol'tsman, B.S. Karasik, A.M. Lyul'kin, and A.D. Semenov, "Ultra-fast superconducting electron bolometer", *J. Tech. Phys. Lett.* **15**, 118–119 (1989).
211. K.S. Il'in, M. Lindgren, M. Currie, A.D. Semenov, G.N. Gol'tsman, R. Sobolewski, S.I. Cherednichenko, and E.M. Gershenzon, "Picosecond hot-electron energy relaxation in NbN superconducting photodetectors", *Appl. Phys. Lett.* **76**, 2752–2754 (2000).
212. Y. Gousev, G. Gol'tsman, A. Semenov, E. Gershenzon, R. Nebosis, M. Heusinger, and K. Renk, "Broad-band ultrafast superconducting NbN detector for electromagnetic-radiation", *J. Appl. Phys.* **75**, 3695–3697 (1994).
213. J. J. A. Baselmans, A. Baryshev, S. F. Reker, M. Hajenius, J. Gao, T. Klapwijk, B. Voronov, and G. Gol'tsman, "Influence of the direct response on the heterodyne sensitivity of hot electron bolometer mixers", *J. Appl. Phys.* **100**, 184103 (2006).
214. W.J. Skocpol, M.R. Beasley, and M. Tinkham, "Self-heating hotspots in superconducting thin-film microbridges", *J. Appl. Phys.* **45**, 4054–4066 (1974).
215. A.D. Semenov and H.-W. Hübers, "Frequency bandwidth of a hot-electron mixer according to the hot-spot model", *IEEE T. Appl. Supercon.* **11**, 196–199 (2001).
216. [http://www.sron.nl/index.php?option=com\\_content&task=view&id=44&Itemid=111](http://www.sron.nl/index.php?option=com_content&task=view&id=44&Itemid=111)
217. S.E. Schwarz and B.T. Ulrich, "Antenna-coupled infrared detectors", *J. Appl. Phys.* **85**, 1870–1873 (1977).
218. A. Balanis, *Antenna Theory: Analysis and Design*, 3<sup>rd</sup> edition, Wiley & Sons, New York 2005.
219. J. Volakis, *Antenna Engineering Handbook*, 4<sup>th</sup> edition, McGraw-Hill, New York, 2007.
220. A.J. Kreisler and A. Gaugue, "Recent progress in HTSC bolometric detectors at terahertz frequencies", *Proc. SPIE* **3481**, 457–468 (1998).



221. G.N. Gol'tsman, Yu.B. Vachtomina, S.V. Antipov, M.I. Finkel, S.N. Maslennikov, K.V. Smirnov, S.L. Poluakov, S.I. Svechnikov, N.S. Kaurova, E.V. Grishina, and B.M. Voronov, "NbN phonon-cooled hot-electron bolometer mixer for terahertz heterodyne receivers", *Proc. SPIE* **5727**, 95–106 (2005).
222. D. Rutledge and M. Muha, "Imaging antenna arrays", *IEEE T. Antennas Propagat.* **AP30**, 535–540 (1982).
223. A.J. Kreisler and A. Gauguier, "Recent progress in high-temperature superconductor bolometric detectors: from the mid-infrared to the far-infrared (THz) range", *Supercond. Sci. Tech.* **13**, 1235–1245 (2000).
224. O. Harnack, B. Karasik, W. McGrath, A. Kleinsasser, and J. Barner, "Submicron-long HTS hot-electron mixers", *Supercond. Sci. Tech.* **12**, 850–852 (1999).
225. B. Karasik, W. McGrath, and M. Gaidis, "Analysis of a high- $T_c$  hot-electron mixer for terahertz applications", *J. Appl. Phys.* **81**, 1581–1589 (1997).
226. F. Ronnung, S. Cherednichenko, G. Gol'tsman, E. Gershenson, and D. Winkler, "A nanoscale YBCO mixer optically coupled with a bow tie antenna", *Supercond. Sci. Tech.* **12**, 853–855 (1999).
227. M. Lindgren, M. Currie, C. Williams, T.Y. Hsiang, P.M. Fauchet, R. Sobolewski, S.H. Moffat, R.A. Hughes, J.S. Preston, and F.A. Hegmann, "Intrinsic picosecond response times of Y-Ba-Cu-O superconducting photoresponse", *Appl. Phys. Lett.* **74**, 853–855 (1999).
228. V.V. Shirov and Yu.Ya. Divin, "Frequency-selective Josephson detector: Power dynamic range at subterahertz frequencies", *Techn. Phys. Lett.* **30**, 522–524 (2004).
229. M.V. Lyatti, D.A. Tkachev, and Yu.Ya. Divin, "Signal and noise characteristics of a terahertz frequency-selective  $\text{YBa}_2\text{Cu}_3\text{O}_{7-x}$  Josephson detector", *Techn. Phys. Lett.* **32**, 860–862 (2006).
230. D.J. Benford and S.H. Moseley, "Superconducting transition edge sensor bolometer arrays for submillimeter astronomy", *Proc. Int. Symp. on Space and THz Technology*, www.eecs.umich.edu/~jeast/benford\_2000\_4\_1.pdf
231. D. Olaya, J. Wei, S. Pereverzev, B.S. Karasik, J.H. Kawamura, W.R. McGrath, A.V. Sergeev, and M.E. Gershenson, "An ultrasensitive hot-electron bolometer for low-background SMM applications", *Proc. SPIE* **6275**, 627506 (2006).
232. K. Irwin, "An application of electrothermal feedback for high-resolution cryogenic particle-detection", *Appl. Phys. Lett.* **66**, 1998–2000 (1995).
233. K. Irwin, G. Hilton, D. Wollman, and J. Martinis, "X-ray detection using a superconducting transition-edge sensor microcalorimeter with electrothermal feedback", *Appl. Phys. Lett.* **69**, 1945–1947 (1996).
234. A.T. Lee, P.L. Richards, S.W. Nam, B. Cabrera, and K.D. Irwin, "A superconducting bolometer with strong electrothermal feedback", *Appl. Phys. Lett.* **69**, 1801–1803 (1996).
235. G.C. Hilton, J.M. Martinis, K.D. Irwin, N.F. Bergren, D.A. Wollman, M.E. Huber, S. Deiker, and S.W. Nam, "Micro-fabricated transition-edge X-ray detectors", *IEEE T. Appl. Supercon.* **11**, 739–742 (2001).
236. B. Cabrera, R. Clarke, P. Colling, A. Miller, S. Nam, and R. Romani, "Detection of single infrared, optical, and ultraviolet photons using superconducting transition edge sensors", *Appl. Phys. Lett.* **73**, 735–737 (1998).
237. W. Duncan, W.S. Holland, M.D. Audley, M. Cliffe, T. Hodson, B.D. Kelly, X. Gao, D.C. Gostick, M. MacIntosh, H. McGregor, T. Peacocke, K.D. Irwin, G.C. Hilton, S.W. Deiker, J. Beier, C.D. Reintsema, A.J. Walton, W. Parkes, T. Stevenson, A.M. Gundlach, C. Dunare, and P.A.R. Ade, "SCUBA-2: Developing the detectors", *Proc. SPIE* **4855**, 19–29 (2003).
238. A.J. Walton, W. Parkes, J.G. Terry, C. Dunare, J.T.M. Stevenson, A.M. Gundlach, G.C. Hilton, K.D. Irwin, J.N. Ullom, W.S. Holland, W. Duncan, M.D. Audley, P.A.R. Ade, R.V. Sudiwala, and E. Schulte, "Design and fabrication of the detector technology for SCUBA-2", *IEE Proc.-A* **151**, 119–120 (2004).
239. A.-D. Brown, D. Chuss, V. Mikula, R. Henry, E. Wollack, Y. Zhao, G.C. Hilton, and J.A. Chervenak, "Auxiliary components for kilopixel transition edge sensor arrays", *Solid State Electron.* **52**, 1619–1624 (2008).
240. S. Lee, J. Gildemeister, W. Holmes, A. Lee, and P. Richards, "Voltage-biased superconducting transition-edge bolometer with strong electrothermal feedback operated at 370 mK", *Appl. Opt.* **37**, 3391–3397 (1998).
241. H.F.C. Hoevers, A.C. Bento, M.P. Bruijn, L. Gottardi, M.A.N. Korevaar, W.A. Mels, and P.A.J. de Korte, "Thermal fluctuation noise in a voltage biased superconducting transition edge thermometer", *Appl. Phys. Lett.* **77**, 4422–4424 (2000).
242. M.D. Audley, D.M. Glowacka, D.J. Goldie, A.N. Lasenby, V.N. Tsaneva, S. Withington, P.K. Grimes, C.E. North, G. Yassin, L. Piccirillo, G. Pisano, P.A.R. Ade, G. Teleberg, K.D. Irwin, W.D. Duncan, C.D. Reintsema, M. Halpern, and E.S. Battistelli, "Tests of finline-coupled TES bolometers for COVER", *Digest IRMMW-THz-2007 Conf.*, 180–181, Cardiff, 2007.
243. J.A. Chervenak, K.D. Irwin, E.N. Grossman, J.M. Martinis, C.D. Reintsema, and M.E. Huber, "Superconducting multiplexer for arrays of transition edge sensors", *Appl. Phys. Lett.* **74**, 4043–4045 (1999).
244. P.J. Yoon, J. Clarke, J.M. Gildemeister, A.T. Lee, M.J. Myers, P.L. Richards, and J.T. Skidmore, "Single superconducting quantum interference device multiplexer for arrays of low-temperature sensors", *Appl. Phys. Lett.* **78**, 371–373 (2001).
245. *The SQUID Handbook*, Vol. II: Applications, edited by J. Clarke and A.I. Braginski, Wiley-VCH, Weinheim, 2006.
246. K.D. Irwin, "SQUID multiplexers for transition-edge sensors", *Physica C* **368**, 203–210 (2002).
247. K.D. Irwin, M.D. Audley, J.A. Beall, J. Beyer, S. Deiker, W. Doriese, W.D. Duncan, G.C. Hilton, W.S. Holland, C.D. Reintsema, J.N. Ullom, L.R. Vale, and Y. Xu, "In-focal-plane SQUID multiplexer", *Nuclear Inst. Methods Phys. Research A* **520**, 544–547 (2004).
248. K.D. Irwin and G.C. Hilton, "Transition-edge sensors", in *Cryogenic Particle Detection*, pp. 63–149, edited by C. Enss, Springer-Verlag, Berlin, 2005.
249. T.M. Lanting, H.M. Cho, J. Clarke, W.L. Holzapfel, A.T. Lee, M. Lueker, P.L. Richards, M.A. Dobbs, H. Spieler, and A. Smith, "Frequency-domain multiplexed readout of transition-edge sensor arrays with a superconducting quantum interference device", *Appl. Phys. Lett.* **86**, 112511 (2005).
250. W.S. Holland, W. Duncan, B.D. Kelly, K.D. Irwin, A.J. Walton, P.A.R. Ade, and E. I. Robson, "SCUBA-2: A new generation submillimeter imager for the James Clerk Maxwell Telescope", *Proc. SPIE* **4855**, 1–18 (2003).

251. A.L. Woodcraft, M.I. Hollister, D. Bintley, M.A. Ellis, X. Gao, W.S. Holland, M.J. MacIntosh, P.A.R. Ade, J.S. House, C.L. Hunt, and R.V. Sudiwala, "Characterization of a prototype SCUBA-2 1280-pixel submillimetre superconducting bolometer array", *Proc. SPIE* **6275**, 62751F (2006).
252. "SCUBA-2," <http://www.roe.ac.uk/ukate/projects/scubatwo/>
253. D.J. Benford, J.G. Steguhn, T.J. Ames, C.A. Allen, J.A. Chervenak, C.R. Kennedy, S. Lefranc, S.F. Maher, S.H. Moseley, F. Pajot, C. Rioux, R.A. Shafer, and G.M. Voellmer, "First astronomical images with a multiplexed superconducting bolometer array", *Proc. SPIE* **6275**, 62751C (2006).
254. J. Gildemeister, A. Lee, and P. Richards, "Monolithic arrays of absorber-coupled voltage-biased superconducting bolometers", *Appl. Phys. Lett.* **77**, 4040–4042 (2000).
255. D.J. Benford, G.M. Voellmer, J.A. Chervenak, K.D. Irwin, S.H. Moseley, R.A. Shafer, G.J. Stacey, and J.G. Staguhn, "Thousand-element multiplexed superconducting bolometer arrays", in *Proc. Far-IR, Sub-MM, and MM Detector Workshop*, Vol. NASA/CP-2003-211 408, pp. 272–275, edited by J. Wolf, J. Farhoomand, and C.R. McCreight, 2003.
256. J. Gildemeister, A. Lee, and P. Richards, "A fully lithographed voltage-biased superconducting spiderweb bolometer", *Appl. Phys. Lett.* **74**, 868–870 (1999).
257. W. Knap, V. Kachorowski, Y. Deng, S. Romyantsev, J.-Q. Lu, R. Gaska, M.S. Shur, G. Simin, X. Hu, and M.A. Khan, C.A. Saylor, and L.C. Brunal, "Nonresonant detection of terahertz radiation in field effect transistors", *J. Appl. Phys.* **91**, 9346–9353 (2002).
258. A. El Fatimy, F. Teppe, N. Dyakonova, W. Knap, D. Seliuta, G. Valusis, A. Shchepetov, Y. Roelens, S. Bollaert, A. Cappy, and S. Romyantsev, "Resonant and voltage-tunable terahertz detection in InGaAs/InP nanometer transistors", *Appl. Phys. Lett.* **89**, 131926 (2006).
259. Y.M. Meziani, J. Lusakowski, N. Dyakonova, W. Knap, D. Seliuta, E. Sirmulis, J. Deverson, G. Valusis, F. Boeuf, and T. Skotnicki, "Non resonant response to terahertz radiation by submicron CMOS transistors", *IEICE T. Electr.* **E89SC**, 993–998 (2006).
260. G.C. Dyer, J.D. Crossno, G.R. Aizin, J. Mikalopas, E.A. Shaner, M.C. Wanke, J.L. Reno, and S.J. Allen, "A narrowband plasmonic terahertz detector with a monolithic hot electron bolometer", *Proc. SPIE* **7215**, 721503 (2009).
261. W. Knap, M. Dyakonov, D. Coquillat, F. Teppe, N. Dyakonova, J. Lusakowski, K. Karpierz, M. Sakowicz, G. Valusis, D. Seliuta, I. Kasalynas, A. El Fatimy, Y.M. Meziani, and T. Otsuji, "Field effect transistors for terahertz detection: physics and first imaging applications", *J. Infrared Millim. Te.* **30**, 1319–1337 (2009).
262. W. Knap, D. Coquillat, N. Dyakonova, F. Teppe, O. Klimenko, H. Videlier, S. Nadar, J. Lusakowski, G. Valusis, F. Schuster, B. Giffard, T. Skotnicki, C. Gaquiere, and A. El Fatimy, "Plasma excitations in field effect transistors for terahertz detection and emission", *C.R. Phys.* **11**, 433–443 (2010).
263. W. Knap, F. Teppe, Y. Meziani, N. Dyakonova, J. Lusakowski, F. Boeuf, T. Skotnicki, D. Maude, S. Romyantsev, and M.S. Shur, "Plasma wave detection of sub-terahertz and terahertz radiation by silicon field-effect transistors", *Appl. Phys. Lett.* **85**, 675–677 (2002).
264. F. Teppe, M. Orlov, A. El Fatimy, A. Tiberj, W. Knap, J. Torres, V. Gavrilenko, A. Shchepetov, Y. Roelens, and S. Bollaert, "Room temperature tunable detection of subterahertz radiation by plasma waves in nanometer InGaAs transistors", *Appl. Phys. Lett.* **89**, 222109 (2006).
265. R. Tauk, F. Teppe, S. Boubanga, D. Coquillat, W. Knap, Y. M. Meziani, C. Gallon, F. Boeuf, T. Skotnicki, and C. Fenoillet-Beranger, "Plasma wave detection of terahertz radiation by silicon field effects transistors: Responsivity and noise equivalent power", *Appl. Phys. Lett.* **89**, 253511 (2006).
266. V.I. Gavrilenko, E.V. Demidov, K.V. Maremyanin, S.V. Morozov, W. Knap, and J. Lusakowski, "Electron transport and detection of terahertz radiation in a GaN/AlGaIn submicrometer field-effect transistor", *Semiconductors* **41**, 232–234 (2007).
267. Y.M. Meziani, M. Hanabe, A. Koizumi, T. Otsuji, and E. Sano, "Self oscillation of the plasma waves in a dual grating gates HEMT device", *Int. Conf. Indium Phosphide and Related Materials*, Conf. Proceedings, 534–537, Matsue, 2007.
268. A.M. Hashim, S. Kasai, and H. Hasegawa, "Observation of first and third harmonic responses in two-dimensional AlGaAs/GaAs HEMT devices due to plasma wave interaction", *Superlattice Microsc.* **44**, 754–760 (2008).
269. V. Ryzhii, A. Satou, I. Khmyrova, M. Ryzhii, T. Otsuji, V. Mitin, and M.S. Shur, "Plasma effects in lateral Schottky junction tunneling transit-time terahertz oscillator", *J. Phys.: Conf. Ser.* **38**, 228–233 (2006).
270. X.G. Peralta, S.J. Allen, M.C. Wanke, N.E. Harff, J.A. Simmons, M.P. Lilly, J.L. Reno, P.J. Burke, and J.P. Eisenstein, "Terahertz photoconductivity and plasmon modes in double-quantum-well field-effect transistors", *Appl. Phys. Lett.* **81**, 1627–1630 (2002).
271. M. Dyakonov, and M.S. Shur, "Shallow water analogy for a ballistic field effect transistor: new mechanism of plasma wave generation by the dc current", *Phys. Rev. Lett.* **71**, 2465–2468 (1993).
272. M. Dyakonov and M. Shur, "Plasma wave electronics: Novel terahertz devices using two dimensional electron fluid", *IEEE T. Electron Dev.* **43**, 1640–1646 (1996).
273. M. Shur and V. Ryzhii, "Plasma wave electronics", *Int. J. High Speed Electr. Syst.* **13**, 575–600 (2003).
274. A. Eguliz, T.K. Lee, J.J. Quinn, and K.W. Chiu, "Interface excitations in metal-insulator-semiconductor structures", *Phys. Rev.* **B11**, 4989–4993 (1975).
275. S. Kang, P.J. Burke, L.N. Pfeiffer, and K.W. West, "Resonant frequency response of plasma wave detector", *Appl. Phys. Lett.* **89**, 213512 (2006).
276. F. Teppe, A. El Fatimy, S. Boubanga, D. Seliuta, G. Valusis, B. Chenaud, and W. Knap, "Terahertz resonant detection by plasma waves in nanometric transistors", *Acta Phys. Pol.* **A113**, 815–820 (2008).
277. D. Veksler, F. Teppe, A.P. Dmitriev, V.Yu. Kachorovskii, W. Knap, and M.S. Shur, "Detection of terahertz radiation in gated two-dimensional structures governed by dc current", *Phys. Rev.* **B73**, 125328 (2006).
278. E. Öjefors, A. Lisauskas, D. Glaab, H.G. Roskos, and U.R. Pfeiffer, "Terahertz imaging detectors in CMOS technology", *J. Infrared Millim. Te.* **30**, 1269–1280 (2009).
279. E. Öjefors, U.R. Pfeiffer, A. Lisauskas, and H.G. Roskos, "A 0.65 THz focal-plane array in a quarter-micron CMOS process technology", *IEEE J. Solid-St. Circ.* **44**, 1968–1976 (2009).
280. P.J. Burke, "Carbon nanotube devices for GHz to THz applications", *Proc. SPIE* **5593**, 52–61 (2004).

281. C.M. Sze. *Physics of Semiconductor Devices*, Wiley, New York, 1981.
282. V. Ryzhii, M. Ryzhii, A. Satou, T. Otsuji, A.A. Dubinon, and V.Ya. Aleshkin, "Feasibility of terahertz lasing in optically pumped epitaxial multiple graphene layer structures", *J. Appl. Phys.* **106**, 084507-1-6 (2009).
283. V. Ryzhii, M. Ryzhii, V. Mitin, and T. Otsuji, "Terahertz and infrared photodetection using p-i-n multiple-graphene-layer structures", *J. Appl. Phys.* **107**, 054512-1-7 (2010).
284. S. Reich, C. Thomsen, and J. Maultzsch, *Carbon Nanotubes: Basic Concepts and Physical Properties*, Wiley, Berlin, 2004.
285. Y. Kawano, T. Fuse, S. Toyokawa, T. Uchida, and K. Ishibashi, "Terahertz photon-assisted tunneling in carbon nanotube quantum dots", *J. Appl. Phys.* **103**, 034307 (2008).
286. Y. Kawano, T. Uchida, and K. Ishibashi, "Terahertz sensing with a carbon nanotube/two-dimensional electron gas hybrid transistor", *Appl. Phys. Lett.* **95**, 083123-1-3 (2009).
287. K.S. Yngvesson, K. Fu, B. Fu, R. Zannoni, J. Nicholson, S.H. Adams, A. Ouarraoui, J. Donovan and E. Polizzi, "Experimental detection of terahertz radiation in bundles of single wall carbon nanotubes", *Proc. 19th Int. Symp. Space THz Techn.*, Groningen, 304-313 (2008).
288. Y. Wang, K. Kempa, B. Kimball, J.B. Carlson, G. Benham, W.Z. Li, T.Kempa, J. Rybczynski, A. Herczynski, and Z.F. Ren, "Receiving and transmitting light-like radio waves: Antenna effect in arrays of aligned carbon nanotubes", *Appl. Phys. Lett.* **85**, 2607-2609 (2004).
289. Y. Wang, Q. Wu, X. He, X. Sun, and T. Gui, "Radiation properties of carbon nanotubes antenna at terahertz/infrared range", *Int. J. Infrared Milli.* **29**, 35-42 (2008).
290. O. Astavief, S. Komiyama, T. Kutsuwa, V. Antonov, Y. Kawaguchi, and K. Hirakawa, "Single-photon detector in the microwave range", *Appl. Phys. Lett.* **80**, 4250-4252 (2002).
291. H. Hashiba, V. Antonov, L. Kulik, A. Tzalenchuk, P. Kleinschmid, S. Giblin, and S. Komiyama, "Isolated quantum dot in application to terahertz photon counting", *Phys. Rev.* **B73**, 081310:1-4 (2006).
292. X.H. Su, J. Yang, P. Bhattacharya, G. Ariyawansa, and A.G.U. Perera, "Terahertz detection with tunneling quantum dot inter-sublevel photodetector", *Appl. Phys. Lett.* **89**, 031117-1-3 (2006).
293. T. Ueda, Z. An, S. Komiyama, and K. Hirakawa, "Charge-sensitive infrared phototransistors: Characterization by an all-cryogenic spectrometer", *J. Appl. Phys.* **103**, 093109:1-7 (2008).
294. T. Ueda and S. Komiyama, "Novel ultra-sensitive detectors in the 10-50  $\mu\text{m}$  wavelength range", *Sensors* **10**, 8411-8423 (2010).
295. D. Seliuta, I. Kalyanas, V. Tamoninas, S. Balakauskas, Z. Martnas, S. A. montas, G. Valu is, A. Lisauskas, H.G. Roskos, and K. Köhler, "Silicon lens-coupled bow-tie InGaAs-based broadband terahertz sensor operating at room temperature", *Electron. Lett.* **44**, 825-827 (2006).
296. G. Valu is, D. Seliuta, V. Tamoninas, R. Simnikis, S. Balakauskas, and I. Kalyanas, "Selective and broadband terahertz sensors based on GaAs nanostructures", *Workshop THz Wave Technology*, Bucharest, 19-20 May, 2008.
297. J.-H. Dai, J.-H. Lee, Y.-L. Lin, and S.-C. Lee, "In(Ga)As quantum rings for terahertz detectors", *J. Appl. Phys.* **47**, 2924-2926 (2008).
298. S. Bhowmick, G. Huang, W. Guo, C.S. Lee, P. Bhattacharya, G. Ariyawansa, and A.G.U. Perera, "High-performance quantum ring detector for the 1-3 terahertz range", *Appl. Phys. Lett.* **96**, 231103-1-3 (2010).
299. S. Kim, J.D. Zimmerman, P. Focardi, A.C. Gossard, D.H. Wu, and M.S. Sherwin, "Room temperature terahertz detection based on bulk plasmons in antenna-coupled GaAs field effect transistors", *Appl. Phys. Lett.* **92**, 253508-1-3 (2008).
300. E.A. Shaner, A.D. Grine, J.L. Reno, M.C. Wanke, and S.J. Allen, "Next-generation detectors: Plasmon grating-gate devices have potential as tunable terahertz detectors", *Laser Focus World*, January 2008.
301. G.C. Dyer, J.D. Crossno, G.R. Aizin, E.A. Shaner, M.C. Wanke, J.L. Reno, and S.J. Allen, "A plasmonic terahertz detector with a monolithic hot electron bolometer", *J. Phys.: Condens. Mat.* **21**, 1958031-1-6 (2009).
302. T. Otsuji, M. Hanabe, T. Nishimura, and E. Sano, "A grating-bicoupled plasma-wave photomixer with resonant-cavity enhanced structure", *Opt. Express* **14**, 4815-4825 (2006).